UTRECHT UNIVERSITY

MSC THESIS

Metamorphic conditions of the Cap de Creus shear zones (NE Spain) - Insights from an integrated petrological, electron microscopy and numerical approach

---

Author:
J.H. van Melick

Supervisors:
Prof. dr. Martyn Drury
Dr. Richard Wessels

A thesis submitted in fulfillment of the requirements for the degree of Master of Science

in the

Structural Geology
Department of Earth Sciences

October 16, 2021

UTRECHT UNIVERSITY

Abstract

Faculty of Geosciences
Department of Earth Sciences

Master of Science

Metamorphic conditions of the Cap de Creus shear zones (NE Spain) - Insights from an integrated petrological, electron microscopy and numerical approach

by J.H. van Melick

Recent advances in the field of scanning electron microscopy (SEM) allow the simultaneous, grid-wise, collection of energy dispersive X-ray spectra (EDS) and the capture of back-scattered electrons (BSE). Phase maps of sample surfaces are created by comparing pre- (or post) defined phase classifications to relative elemental abundances obtained by automated deconvolution of the EDS signal. The construction of phase maps using this method is named 'SEM-EDS automated mineralogy', or SEM-AM. In this work an SEM-AM-based workflow is evaluated in a case study on pegmatites and high-grade metasediments that have been strongly deformed into shear zones under greenschist facies conditions. While the structural features of these Cap de Creus area (NE Spain) greenschist facies shear zones have been studied in detail, only few PT constraints are available.

Bulk rock chemistry (BRC) of the samples is calculated by applying a Python-based script to SEM-AM derived data integrated with phase classifications constrained by EDS-SEM and wavelength dispersive X-ray spectroscopy (WDS) microprobe spot measurements. This calculated BRC is compared to BRC obtained using X-ray fluorescence (XRF) on the corresponding samples, and subsequently used as input for numerical modeling with Perple_X. The resulting equilibrium mineral assemblages are compared to the mineral assemblages observed in the samples in order to constrain deformation conditions. To obtain additional constraints on deformation temperatures, quartz microstructures are analyzed and the Ti-in-Quartz geothermometer is applied to selected quartz grains. Trace element chemistry is studied to quantify the effect of fluid influx.

This thesis demonstrates how the aforementioned SEM-AM workflow can deliver high-quality whole-rock chemistry results that are consistent with traditional methods, providing that mineral chemistry can be adequately constrained. The SEM-AM false color phase maps are a great asset because they visualize the relation between mineral associations, structural features and mineral reactions. Integration of the SEM-AM results with a numerical approach provides new PT estimates for the greenschist shear zones, ranging from 400-430 °C at 2.5 kbar to 410-450 °C at 3.5 kbar. Uncertainties in Ti-activity result in a large T uncertainty of results obtained using the Ti-in-Quartz geothermometer, but results suggest pressure may be as low as 2 kbar, associated with temperatures between 390-420 °C. For an undeformed sample PT conditions are estimated at 650$\pm$30 °C at pressures of >3.9 kbar, which is in accordance with earlier estimates. From trace element chemistry a mass increase of $\pm$54% is computed as a result of element transport by Si- and presumably Ca-rich fluids, and thermodynamic modeling highlights the effects Fe speciation has on mineral stabilities. The here presented PT results, quartz microstructures, and observed Al_2SiO_5 polymorph behavior, indicate deformation under progressively decreasing metamorphic conditions consistent with the retrograde stages of the Variscan orogeny.

Acknowledgements

I would like to thank my supervisors, Martyn Drury and Richard Wessels for allowing me to work on this interesting project and their guidance and support throughout this work, and Richard Wessels again for the SEM work. Furthermore I would like to thank Maartje Hamers for acquiring the EBSD data and support with the CL imaging, Helen de Waard for the LA-ICP-MS measurements and Cees-Jan de Hoog for performing the SIMS analyses in Edinburgh. Financial support for the geochemical analyses was provided by the Olaf Schuiling Fund.

Contents

List of Figures

List of Tables

1 Introduction

1.1 General Introduction

Constraining the physical and chemical environments of rocks during metamorphism is a key element in the understanding of large-scale geologic processes: unless we have insights on the conditions, mechanisms and rates of metamorphic processes it is impossible to unravel the geodynamic history of Earth's crust. In that context, the ability to reconstruct *P-T-t* paths of metamorphic rocks has been instrumental in geology, for example in determining the tectonic evolution of continental collision and lithospheric extension settings.

Mineral assemblages, textures and in some cases index minerals (e.g. kyanite in rocks with a pelitic composition) can provide qualitative information about the conditions at which a rock equilibrated. Qualitative methods rely on the principle that for a given mineral its composition changes systematically with pressure or temperature (e.g. the exchange between Fe and Mg in garnet and biotite). However, most qualitative methods do not provide information on both pressure and temperature and have a limited range in which they can be applied.

The progress that has been made in the development of internally consistent thermodynamic databases and activity models in the last decades has provided means of constraining metamorphic conditions using a mathematical framework that connects extensive properties such as chemical composition to intensive properties (pressure, temperature and chemical potentials). Relying on the principle that stable phases are the ones with the minimum Gibbs free energies allows for the calculation of diagrams that show how phases or phase assemblages change as a function of (a combination) of temperature, pressure or phase composition (e.g. Holland and Powell, 1998; White et al., 2000; Connolly and Petrini, 2002; Connolly, 2005; Connolly, 2009).

Normal phase diagrams display the equilibrium relationships between minerals or mineral assemblages, and depending on its chemical composition a system may experience only some of them (or none at all). Pseudosections are diagrams that show only the reactions that are relevant for a specific chemical composition. Another difference is that pseudosections include continuous reactions: reactions that occur over a range of conditions where both the reaction products and reactants are stable but have a composition that changes systematically as conditions change. In natural rocks continuous reactions are more common than discontinuous reactions as many minerals allow for compositional variation. Pseudosections can thus show changes in mineralogy that would not be visible on standard phase diagrams.

The results obtained by thermodynamic modeling stand or fall with the bulk rock composition (BRC) that is used as input. X-Ray Fluorescence (XRF) is one of the most widely used techniques for major and minor element analysis due to its low cost and ease of use, but a potential drawback of XRF analysis is that it requires samples to be prepared in powder form and homogenized and that well-characterized standards of similar composition are available.

Recent advances in the field of Scanning Electron Microscopy (SEM) allow for simultaneous processing of both the electrons generated the sample surface or back-scattered

from within the sample and the X-rays that are emitted as the interacted surface atom returns to its ground state after it becomes ionized. After the EDS (Energy-Dispersive Spectroscopy) detector separates the emitted characteristic X-rays from the different elements into an energy spectrum, software is used to determine the relative abundance of elements and classify different phases. This makes it possible to create phase maps of sample surfaces. While encountered in somewhat varying meanings, the term Automated Mineralogy (AM) is generally used for the automated construction of phase maps using the classification of EDS spectra (Schulz et al., 2020). After phases are classified and mapped the underlying data can be used to calculate the chemical composition of the scanned area.

In this study a SEM-EDS automated mineralogy workflow will be evaluated in the form of a case study on (presumably) greenschist metamorphic rocks from the Cap de Creus area, northeastern Spain. Automated mineralogy results will be complemented with and compared to data obtained using various other analytical techniques and will form the basis of thermodynamic modeling.

1.2 Geological Setting

The Pyrenees are an alpine-aged approximately east-west trending intracontinental mountain belt located in southwestern Europe, forming the border between France and Spain (figure 1.1). The Pyrenees formed as a result of (partial) subduction of the Iberian microplate underneath the European continent during the late Cretaceous to late Oligocene (Vergés et al., 2002).

The crystalline core of the Pyrenees is called the axial zone and is a remnant of an older tectonic period: the Variscan orogeny, a late-Paleozoic continental collision between Euramerica and Gondwana, forming the supercontinent Pangea. The axial zone consists of pre-Mesozoic magmatic and metasedimentary rocks.

Following Zwart and De Sitter (1979) the axial zone of the Pyrenees can be divided into three major structural domains:

(i) The suprastructure, having undergone mostly low-grade metamorphism and its main Variscan structures consisting of upright folds and related axial planar foliation.

(ii) The infrastructure, having undergone medium- to high-grade metamorphism and its main Variscan structures consisting of recumbent folds and associated flat-lying foliation.

(iii) (Late) Variscan batholiths.

The axial zone is separated from Alpine fold- and thrust belts on both its northern and southern side by the NPF (North Pyrenean Fault) and north dipping thrusts (Nogueras Zone), respectively. Its infrastructure consists of several in W(NW)-E(SE) orientation elongated mantled gneiss domes, having a width and length in the order of tens of kilometers. These dome-shaped structures are comprised of an orthogneiss core and a greenschist to amphibolite facies sedimentary mantle (B. Eeckhout, 1986; Mezger et al., 2012). Thrust faults and strike-slip faults with a significant vertical component of both Variscan and Alpine age are located within the axial zone and generally dip at a steep angle. These faults are oriented parallel to the orogenic trend and always show a relative upthrow of the northern block (Mezger et al., 2012).

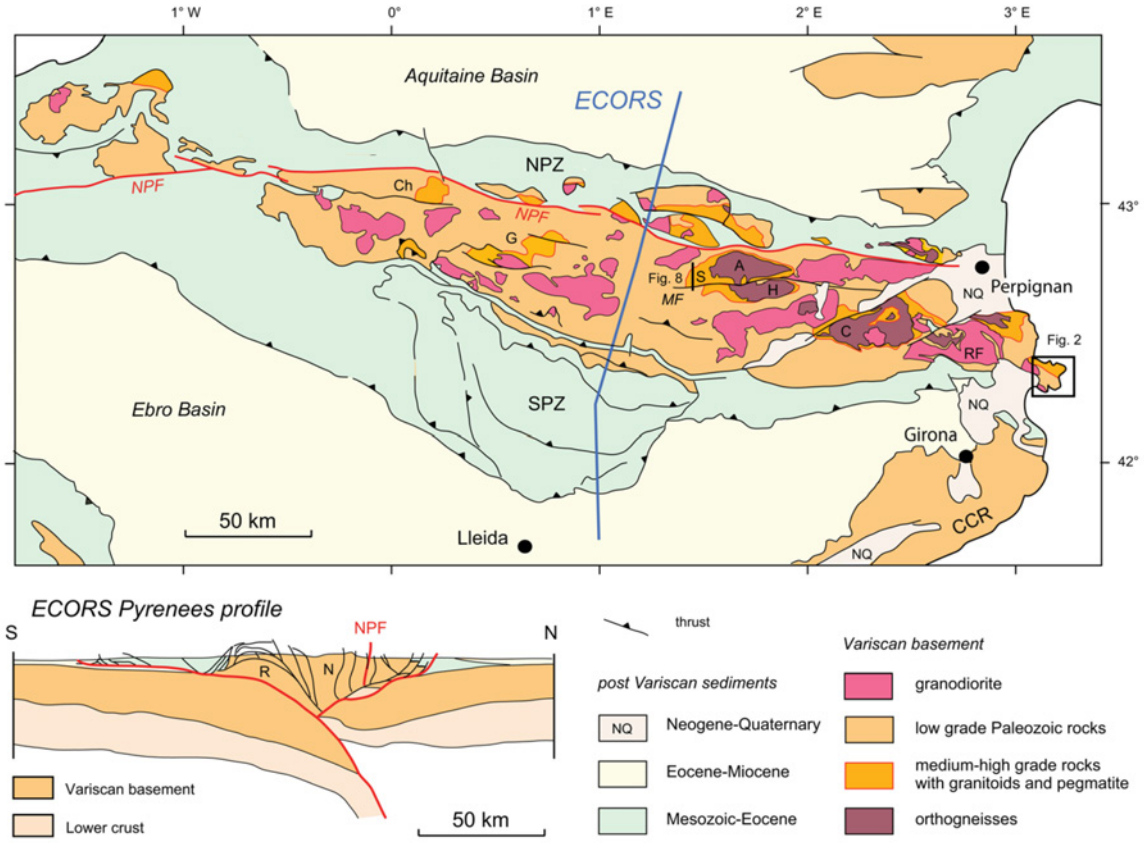

FIGURE 1.1: Geological map of the Pyrenees, obtained from Vissers et al. (2017). The area outlined Fig. 2 is the Cap de Creus area.

1.2.1 Metamorphism of the Cap de Creus peninsula

The Cap de Creus peninsula (easternmost Pyrenees, Spain, figure 1.1) represents a well-studied fragment of Variscan (mid-) crust consisting of greenschist- to amphibolite facies metasediments and granitoids. Characteristic features of the area (figures 1.2 & 1.3) are:

(i) A metamorphic gradient increasing in map view from SW (chlorite zone) to NE (sillimanite zone). A thermal gradient of approximately 80°C/km has been proposed by several authors (e.g. Druguet, 2001) and the WNW-ESE trending isograds crosscut pre-Variscan lithologies at a high angle.

(ii) Isograds are oriented (sub)parallel to the pegmatite dyke swarms and migmatitic complexes located in the high-grade metamorphic zones.

(iii) The overprinting of high-grade structures by zones comprised of narrow and anastomosing bands of low-grade metamorphism (greenschist facies), associated with late folding and mylonitization.

The protolith rock consists of late Precambrian or Cambro-Ordovician psammitic and pelitic layers (Druguet and Hutton, 1998) that have experienced low-pressure and medium- to high-temperature metamorphism during the Variscan orogeny. The cordierite-andalusite zone (labeled as andalusite zone in figure 1.2) is approximately 1.5-2 km wide and is characterized by biotite-cordierite, biotite-cordierite-andalusite, biotite-andalusite and biotite-garnet assemblages. Staurolite can only be found as rare relics within andalusite crystals

(Druguet, 2001). Reche et al. (1996) estimated P-T conditions for the upper part of this zone at 600 °C and 4.3 kbar using a petrogenetic grid.

Transitioning NNE into the sillimanite-muscovite zone grain size increases and sillimanite appears, frequently as fibrolite. In the psammitic layers garnet (almandine) porphyroblasts containing biotite inclusions have been observed by Druguet (2001), as well as relics of staurolite in cordierite. With increasing metamorphic grade towards the NNE the sillimanite-muscovite zone is reached before the association of sillimanite-K-felspar, often as clusters of fibrolite-quartz-K-feldspar, is encountered. In the highest-grade zones partial melting of schists has resulted locally in the formation of migmatites that are spatially associated with the intrusion of granitoid bodies (Druguet, 2001).

1.2.2 Magmatism in the Cap de Creus peninsula

Based on the level of intrusion and their volume, two groups of Variscan igneous rocks can be recognized (Druguet, 2001)

(i) Small intrusions in the sillimanite-muscovite and sillmanite-K-feldspar zones: these consist of hornblende quartz-gabbro, quartz-diorite, tonalite granodiorite and granite. Further, dykes of leucogranite and pegmatite are present. The intrusions are surrounded by migmatites, therefore these associations can be described as migmatite complexes. Three migmatitic complexes are located in the Cap de Creus area, and based on structural arguments migmatization has been interpreted by Druguet et al. (2014) as being coeval with the emplacement of a syntectonic quartz-diorite belonging to the Tudela migmatitic complex. While there are questions regarding syntectonic placement, the zircon U/Pb ages obtained by the same authors of $\pm$299 Ma provide an upper age constraint for the HT-LP metamorphism, and thus confirm a Variscan age.

The pegmatites have formed a $\pm$2.4 km wide cluster of dykes that is oriented more or less parallel to the trend of the metamorphic zones and is located in the cordierite-andalusite zone and the sillimanite zone with its associated migmatite complexes. The pegmatites and leucogranites may have been formed as a result from partial melting of the pelitic metasediments as has been postulated by Damm et al. (1992), which has been observed in other Pyrenean Variscan mid-crustal zones. However, in recent work by Van Lichtervelde et al. (2017) it is argued on the basis of observed fractionation patterns that at least some of the pegmatites have a magmatic origin rather than in situ partial melting. These authors have obtained crystallization ages of 299 Ma and secondary ages of 292 Ma that they attribute to a post-solidus hydrothermal event.

The calc-alkaline intrusions are likely mantle-derived, with varying degrees of crustal contamination (Druguet et al., 1997).

(ii) Large sheet-shaped granodiorite bodies (the Roses and Rodes granodiorites), emplaced in low-grade metasediment south of the studied area. The Roses granodiorite is dated at 290 Ma (Druguet et al., 2014).

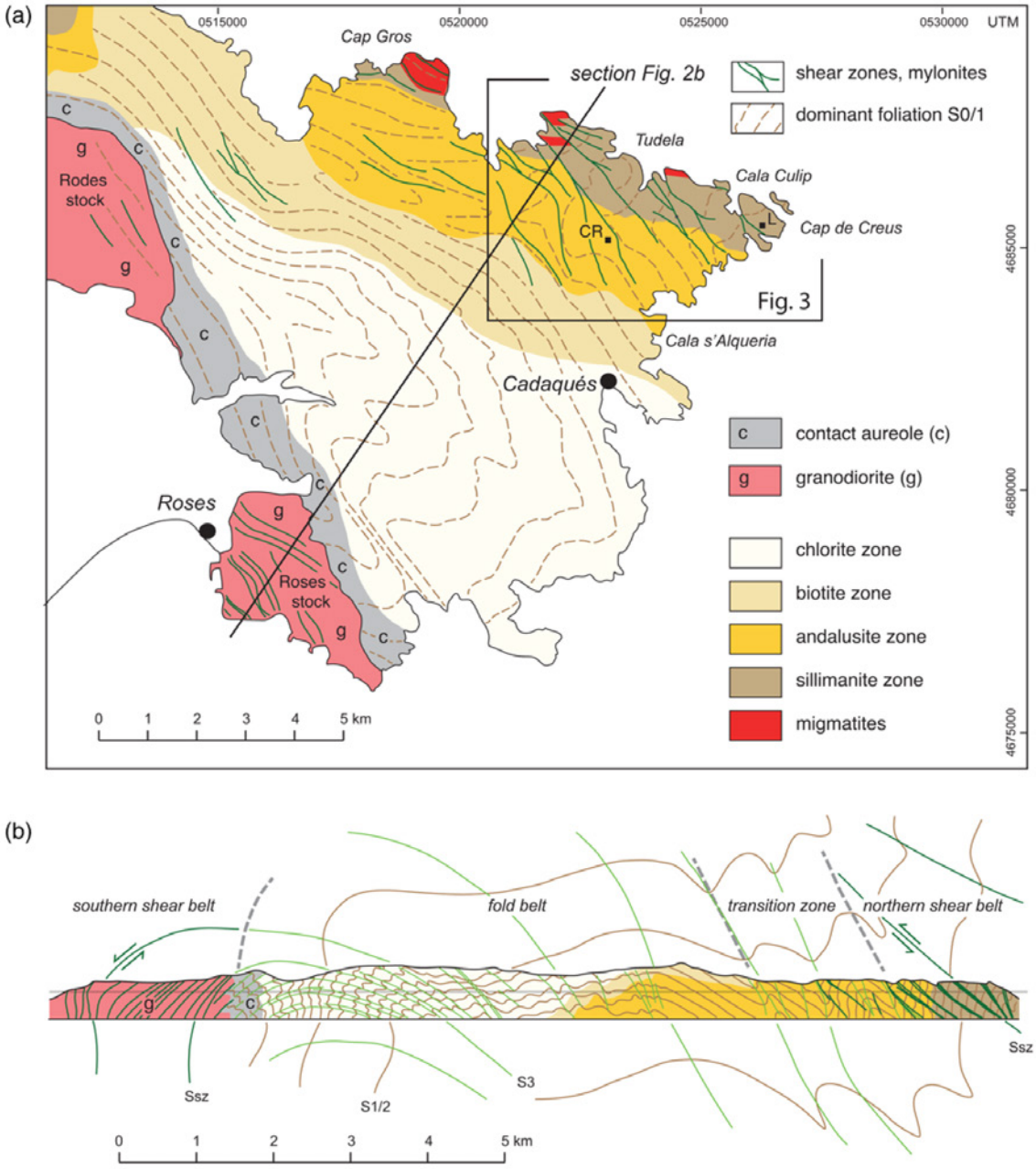

FIGURE 1.2: (**a**) Structural and metamorphic map of the Cap de Creus peninsula, after Druguet et al. (2014) and the geological map of Spain (MapaGeologico de España, sheet 221, Portbou, and sheet 259, Roses). Obtained fromVissers et al. (2017). CR, Can Rabassers de Dalt; L, lighthouse. The outlined northeastern area is shown in more detail in figure 1.3. (**b**) Structural cross-section across the Cap de Creus peninsula, after Carreras (2001), obtained from Vissers et al. (2017).

1.2.3 Tectonic evolution of the Cap de Creus peninsula

The area has experienced a history of poly-phase deformation in which a distinction can be made between three major episodes of deformation. A summary is presented below, for a detailed description of the deformation history the reader can refer to Druguet et al. (1997), Druguet (2001), and Carreras (2001).

D1

The oldest deformation event (D1) recorded in the area resulted in a penetrative schistosity (S1) oriented (sub)parallel to the sedimentary bedding (Ss). This schistosity is characterized by the alignment of phyllosilicates and formed well before peak metamorphic conditions. In domains where no significant overprinting took place S1 trends N-S and dips moderate to steep towards the east. D1 does not appear to have played a regional significant role, but is thought to have produced recumbent folds and/or thrusts and is associated with crustal thickening and a first metamorphic stage. Correcting for subsequent deformation the S1 foliation followed the trajectory of a large scale dome-shaped structure (Druguet et al., 1997).

D2

D2 can be characterized as a prograde folding event leading to folding of the bedding and first schistosity. Crenulations and bandings (S2) in metapelites are defined mainly by biotite and in higher grade metamorphic zones by biotite and sillimanite. The D2 event is associated with non-coaxial compression during which upright folds were produced, and the original trending of these structures is approximately NE-SW and ENE-WSW in zones of more intense D2 deformation (Druguet, 2001). The fold-related strain gradients across the area make a distinction between structurally homogeneous high- and low strain domains possible:

(i) A southern low-strain domain where S1 foliation is dominant, and

(ii) A northern high-strain domain, where S2 dominates.

F2 folds with sub-horizontal fold axes and associated crenulation cleavage. Towards the center of the high strain zone the increased strain is accommodated by increasing tightness of the folds and the clockwise rotation of both Ss/1 and S2 towards a ENE-WSW trend that steeply dips north. Druguet (2001) suggests that the high strain zone could represent a stretched and sheared limb of a large sub-vertical fold.

D3

D3 is characterized by progressive deformation under greenschist conditions during which folds and shear zones developed that deform and overprint D1 and D2 structures. D3 structures are mainly NW-SE oriented, however the attitude of structures is dependent on strain intensity: with increasing strain, a more NNW-SSE direction is observed. E-W trending folds present in low grade and low-strain domains clearly post-dating D2 are likely to represent early stages of D3 deformation, while NW-SE folds and shear zones can be attributed to later stages of deformation during which strain was more localized (Carreras, 2001). In the higher-grade metamorphic zones the late folds disappear and the number of shear zones increases, forming an anastomosing network.

Two of these networks can be recognized, referred to by Carreras (2001) as the northern shear belt and the southern shear belt: the first cutting through medium- to high-grade metasediments while the latter cuts through Variscan granodiorites. Both belts display a similar (approximately) NW-SE trend and are separated by a region of low-grade and complexly folded metasediments. The shear zones show predominant strike-slip movement with a generally dextral sense of shear for the northern belt and sinistral sense of shear for the southern belt. This study focuses on the northern shear belt that resulted in the local greenschist-facies overprinting of the amphibolite facies metasediments.

1.2.4 Northern shear belt

The northern shear belt is comprised of the classical Cap de Creus shear zones that cross-cut all D1 and D2 fabrics. Most shear zones cut the preexisting foliation at an angle and in these situations a deflection of the dominant regional foliation to the orientation of the shear zones is observed. The mylonitic equivalents of the undeformed host rocks are penetratively foliated and as a result of their heterogeneous composition often display distinct banding.

The shear belt consists of NW-SE trending and NE dipping shear zones that have accommodated top to SE shear along moderately steep NW plunging stretching lineations. The former are interlinked with more E-W orientated and N north-dipping shear zones that display steeply NW plunging stretching lineations (Carreras, 2001; Fusseis et al., 2006).

Based on the undeformed host rock, three main types of mylonites can be distinguished:

1. Quartz-rich mylonites, containing varying proportions of feldspar, resulting from the shearing of the psammitic layers.

2. Mica-rich mylonites derived from the rocks having a (more) pelitic composition, however as quartz veins are abundant in the schists these mylonites commonly contain thin quartz bands.

3. Quartz- and feldspar rich mylonites having pegmatites and leucogranites as host rock.

In shear zones that show signs of a complex kinematic history the mylonitic foliation in quartz and quartz-feldspar rich mylonites is often deformed by folds, and in mica-rich mylonites extensional crenulations have developed (Carreras, 2001). Until recently the consensus was that these shear zones could be attributed to late-stage Variscan deformation, and due to the lack of geochronological data this was based mainly on structural arguments. However, recently proposed Alpine Ar/Ar dates by Vissers et al. (2017) have sparked a debate (Druguet et al., 2018; Vissers et al., 2018) regarding the Variscan versus Alpine timing of shear zone development.

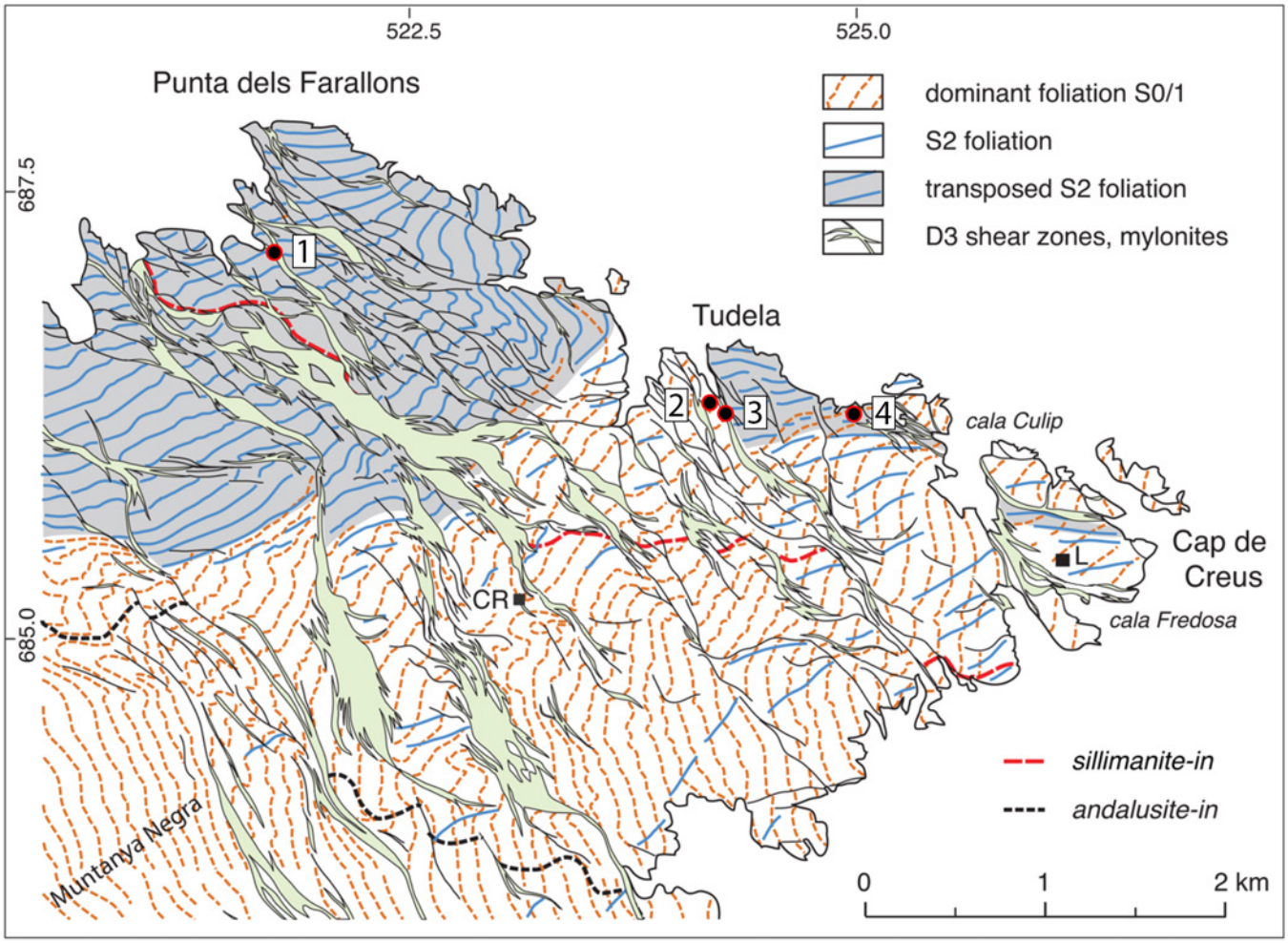

FIGURE 1.3: Structural map of the easternmost area of the Cap de Creus peninsula, modified after Vissers et al. (2017). Black dots denote sample localities, with numbers corresponding to table 3.1.

1.3 Aims and Scope

While the structural and metamorphic geology of the area have been intensively studied, little is published on the metamorphic conditions during development of these greenschist-facies shear zones.

The aim of this study will be to develop and assess an SEM-EDS automated mineralogy workflow, applied to a selection of samples from the northern shear belt in order to obtain constraints on the PT-conditions during shear zone development and activity. Some research (Piazolo, 2001) has suggested the presence of sillimanite in these (presumable) retrograde shear zones. This raises the question whether sillimanite is metastable in dry mylonites, or conversely, if sillimanite formed during prograde development of the shear zones. Therefore, the behavior of Al_2SiO_5 polymorphs in the samples will be studied. In addition, an attempt will be made to qualify the role of fluids during shear zone development.

2 Approach and Methodology

Accurately constraining P-T conditions for greenschist facies metamorphism is challenging due to the limited number of (fully) quantitative geothermobarometric methods that are applicable to low- to medium temperature rocks (Reverdatto et al., 2019). Thermodynamic modeling of phase equilibria has proven to provide valuable insights on metapelites (refer to White et al. (2014b) for a review), of which the input will be the rock chemistry obtained by SEM-EDS automated mineralogy (abbreviated as SEM-AM). The SEM-AM results will be compared with literature data and XRF and Laser Ablation Inductively Coupled Plasma Mass Spectrometry (LA-ICP-MS) data on the same samples. Mineral compositions obtained by SEM-AM will be compared against manual EDS spot measurements and Electron Probe Micro-Analyzer (EPMA) on selected grains. The results of thermodynamic modeling are complemented with data on quartz microstructures and Ti concentrations in quartz to provide additional constraints on metamorphic conditions. Prior to selecting samples for detailed analysis relevant thin sections were characterized using optical microscopy. As this project was conducted during the COVID pandemic laboratory access was limited.

For this study many samples were available that have been acquired during previous field campaigns. For some of these samples suitable thin sections were already prepared, and in case additional thin sections were required these were cut following Tikoff et al. (2019) who proposed a standardized method for the orientation of thin sections with respect to the kinematic and geographic reference frame. A total of 13 thin sections obtained from three shear zones located in the northern shear belt have been studied: one shear zone overprinting amphibolite facies (sillimanite zone) metasedimentary rocks and the other two crosscutting a large pegmatite body. Additionally, an undeformed high-grade schist sample was analyzed to test the methodology and compare mineralogy and whole-rock chemistry against the deformed samples and a quartzite was processed along with the deformed schists for Ti-in-Quartz geothermometry. The sample locations are marked on figure 1.3 and an overview of samples and analyses performed is provided in table 3.1.

2.1 Optical Microscopy

Thin sections were digitized using a Zeiss Axio Scan.Z1 thin section scanner at a 10X magnification and in brightfield transmitted light, resulting in high-resolution (0.44 µm/pixel) files containing channels of both plane polarized light (PPL) as cross-polarized light (XPL). Interpretation and annotation of the scans was done using the ZEN 3.2 (Blue Edition) software.

While working with digitized thin sections has many benefits over traditional microscopy it is difficult to distinguish between positive and negative relief as the focus is fixed, and one cannot observe pleochroism as there is no stage to be rotated. To overcome these limitations and to study specific samples at higher resolutions a traditional petrological microscope was used.

2.2 SEM-EDS Automated Mineralogy

Selected thin sections were polished, carbon coated and analyzed using a Zeiss EVO-15 scanning electron microscope equipped with two Bruker XFlash 6|60 EDS detectors and a back-scattered electrons (BSE) detector. Operating conditions were 15 kV accelerating voltage, in order to ensure x-ray excitation for all elements of interest, and 1 nA probe current. Prior to the automated mineralogy runs, the chemical composition of selected grains was determined by means of EDS spot measurements using Bruker Esprit 2.1 software and saved with the accompanying BSE images. The output of both EDS detectors was registered in separate Microsoft Excel files. This resulted in the measurement of 40-60 individual grains per sample.

The SEM-AM runs were performed with an acceleration voltage of 15 kV, a beam current of 1 nA, an aperature of 30 µm and a dwell time of 0.02 s. Step sizes were 20 µm for the coarse grained samples and 8 µm or 5 µm for the finer-grained samples. For each thin section a selected region of interest was defined and mapped using the Zeiss Mineralogic software suite, resulting in a map of stitched BSE images and a phase map based on the EDS measurements with a user defined pixel size. The EDS measurements are quantitative as a result of the integration of EDS processing within the Zeiss Mineralogic software, allowing for ZAF matrix corrections. The phase map is composed by comparing the EDS data to a table, labeled as 'mineral recipe', in which (ranges of) mineral compositions are specified. This is done by defining a mineral, selecting elements and providing an acceptable range of element concentrations and/or element ratios. Mineral classifications can be further refined by including morphological criteria (e.g. grain size or shape).

The Mineralogic software classifies every pixel as the first phase that matches the measured chemistry of that point by comparing it to the criteria in the mineral recipe. This means that the order in which phases are stored in the mineral recipe is of importance when phases partly overlap in elemental concentrations. All processed EDS data are stored in a database, which allows for retrospective analysis on the measured chemistry in case criteria in the mineral recipe are updated. All thin sections processed with automated mineralogy in this study benefited significantly from fine-tuning of the mineral recipe after the initial analysis.

2.3 Data processing and BRC calculation using SEM-AM data

A Python script (appendix A) was written in order to process the manual EDS spot measurement files and for each element based on the mass normalized concentration calculate the following compositional statistics: minimum value, maximum value, mean value, median value and relative standard deviation. The results for all minerals are aggregated by the script in a single Microsoft Excel file and measurements that are off by more than two standard deviations are highlighted. When the validity of measurements was doubted these measurements were excluded from the calculations. For each mineral the script converts the mean normalized atomic mass to oxide weight percentages, assuming stoichiometry, and summarizes the results in the same Microsoft Excel file.

After each (retrospective) analysis the Zeiss Mineralogic software produces a table that lists for each phase the area percentage, weight percentage (from the specific mass specified in the mineral recipe), average chemical composition in normalized atomic mass and several grain-related properties. This table can be processed using the same Python script to convert mineral compositions to oxide weight percentages, again assuming stoichiometry, and calculate the bulk rock composition. Pixels that did not fulfill the criteria for any

phase, and thus remain unclassified but do have their chemical composition saved, are assumed to be of average specific mass when calculating the bulk rock composition. As the Mineralogic Software does not account for unclassified pixels when determining weight percentages of phases, the original calculated values are corrected in the Python script.

When both automated mineralogy results and manual EDS spot measurements for all or some mineral are available, the Python script can combine these results: the (corrected) weight percentages are obtained from the automated mineralogy results and the mean chemical compositions are calculated from the EDS spot measurements. For the unclassified pixels and phases that do not have any EDS spot measurements, the automated mineralogy chemical composition is taken. Both the results based on the SEM-AM combined with EDS spot measurements as well as the SEM-AM only results are exported to a spreadsheet to allow for comparison, and it is indicated for which minerals EDS spot measurements were available.

In calculating the bulk rock composition only the elements that can be processed in Perple_X using the HP62ver thermodynamic database (Holland and Powell, 2011) are considered: Si, Al, Fe, Mg, Ca, Na, K, Ti, Mn, Zr, F, Cu, S and Cl.

2.4 XRF

XRF analysis was performed on five samples to obtain a second and independent source of bulk rock chemistry. To allow for comparison with SEM-EDS automated mineralogy results material was cut from the same plane as the thin sections. In order to achieve homogeneity, sample material was ground into a powder and dissolved in a heated borate flux before being cooled to produce glass beads. Analysis was performed on a Thermo Scientific ARL Perform'X 4200W WDXRF analyzer.

2.5 LA-ICP-MS

Trace element concentrations can provide insights into the amount of alteration that a rock has undergone as a result of mass transfer by fluids. The method implemented here is outlined in Philpotts and Ague (2009) and relies on the assumption immobile elements to be unaffected by fluid transport. The concentration ratio (i.e. the concentration of an element in the altered rock with respect to the concentration of the same element in the presumably unaltered rock) of an immobile element is then a measure of the the mass gained or lost as a result of mobile elements being transported. The use of concentration ratios are unaffected by the 100% normalization inherent of using weight percentages. Elements commonly regarded as immobile include the high field strength elements (HFSE; Hf, Zr, Ti, Nb, Ta and Th) and rare earth elements (REE) (Jiang et al., 2005; Philpotts and Ague, 2009).

In order to obtain reliable data on element concentrations down to ppm ranges the samples that were analyzed using XRF were subsequently analyzed using LA-ICP-MS. All samples were analyzed three consecutive times, with the analytical configuration as in table 2.1.

Data reduction was done using GLITTER software (http://www.glitter-gemoc.com/) based on the N610 and BCR2-G standards. For each measurement the software automatically proposed an interpolation range, which was manually verified and adjusted in case of doubtful suggested ranges. Care was taken to select the longest possible representative part of the measurement, without including too many anomalously strong (negative) spikes as the software does not allow for exclusion of single points or ranges. The mean values of three measurements were used to calculate concentration ratios.

TABLE 2.1: Overview of LA-ICPMS configuration.

Laser type	Compex 102 excimer
λ	193 nm
Energy	22-30 kV
Energy density on sample	$\pm$12 J cm^{-2}
Beam profile	Homogenized
Repetition rate	10 Hz
Spot size	120 µm
ICPMS type	Thermo Fisher Scientific Element2
Power	1250 W
Plasma gas	Ar - Flow rate: 0.85 l/min
Carrier gas	Ar/He - Flow rate: Ar: 0.7 l/min, He: 0.7 l/min
Cooling gas	Ar - Flow rate: 16 l/min

2.6 EPMA

To assess the accuracy of the EDS spot measurements selected grains on the polished and carbon coated thin sections were analyzed using an JEOL JXA-8530F Hyperprobe electron probe microanalyzer (EPMA) equipped with five wavelength dispersive spectrometers. Operating conditions were 40 degrees takeoff angle, and a beam energy of 15 keV. The beam current was 10 nA, and the beam diameter was 5 µm for all phases except ilmenite (2 µm). Elements were acquired using analyzing crystals LIFH for Fe Kα, Mn Kα, PETL for Ti Kα, PETH for Ca Kα, K Kα, TAPH for Mg Kα, Na Kα, TAP for Si Kα, Al Kα, TAPH for Mg Kα, Na Kα, and TAP for Si Kαand Al Kα. The calibration standards were in-house diopside for Mg Kα, Ca Kα, hematite for Fe Kα, jadeiete for Al Kα, Si Kα, Na Kα, synthetic KTiPO5 for Ti Kα, K Kα, and tephroite for Mn Kα. Both the counting time and peak off counting time was 32 seconds for all elements with a linear correcting method. Unknown and standard intensities were corrected for deadtime.

Oxygen was calculated by cation stoichiometry and included in the matrix correction. For tourmalines, B was calculated 0.097 atoms relative to 1.0 atom of oxygen, based on ideal stoichiometry. H was calculated by difference from 100%, and verified that atomic H:O fulfilled an ideal halogen-free stoichiometric proportions (4:31). Slightly elevated H contents, based on this approach, indicates that some trivalent Fe may be present. The matrix correction method was Phi-Rho-Z and the mass absorption coefficients dataset was CITZMU. The ZAF or Phi-Rho-Z algorithm utilized was Armstrong/Love Scott.

2.7 EBSD

To quantify grainsize distributions and provide a chemistry-independent way of quantifying deformation temperatures an electron backscattered diffraction (EBSD) dataset was acquired for one sample. The thin section was sython polished and carbon coated prior to analysis on a Zeiss Gemini 450 variable pressure SEM equipped with an EBSD detector. Conducting tape was applied to the sample surface surrounding the measurement area to limit unwanted charging effects. EBSD backscatter patterns were obtained at a 70° tilt using an acceleration voltage of 20 kV with a working distance of approximately 25 mm and a step size of 5 µm. The acquired dataset was processed using the AZTEC software (Oxford Instruments) and in MATLAB using the MTEX toolbox (Bachmann et al., 2010).

2.8 Thermodynamic Modeling

The Perple_X software package (Connolly and Petrini, 2002; Connolly, 2005; Connolly, 2009) version 6.9.0 (https://www.perplex.ethz.ch) was used to calculate equilibrium mineral assemblages with the internally consistent dataset (hp62ver.dat) of Holland and Powell (2011). Utilized solution models for biotite, chlorite, chloritoid, cordierite garnet, staurolite and white mica are from White et al. (2014b), and feldspar solid solution models from Holland and Powell (2011). All solution models have been calibrated with the used thermodynamic dataset.

Thermodynamic modeling is often performed using chemical systems with a limited number of components. While this provides clear insights on the reactions that occur between different stability fields it may not represent the reality well as important phases in metapelitic systems are not considered. Including Fe^{3+} and Ti is necessary to include oxide minerals, and without Ca and Na it is impossible to model plagioclase and albite, epidote and some of the white mica's (e.g. paragonite and margarite). Research has also shown that the presence or absence of minor elements can have major effects on mineral stabilities: a study by White et al. (2014a) highlights the effect that manganese concentrations exert on the stability of garnet.

Using the aforementioned thermodynamic database and solution models allows for modeling that considers a wide range of chemical components, and therefore a more realistic modeling of mineral assemblages in natural (metapelitic) rocks.

In this study the following chemical system was considered: MnO-Na_2O-CaO-K_2O-Fe_2O_3-MgO-Al_2O_3-SiO_2-H_2O-TiO_2, assuming the fluid phase to be pure H_2O.

P-T pseudosections were redrawn and annotated using Adobe Illustrator and PyWerami (Lexa, 2011), a Python based application for processing contour- and 3D data, was used for plotting isomodes and compositional isopleths.

An analysis of Forshaw and Pattison (2021) who have studied a large data set on iron partitioning between its Fe^{2+} and Fe^{3+} oxidation states shows that in metapelitic rocks $\pm$75% of the iron is present as Fe^{2+}. This will be used as preliminary value for modeling since the analytical techniques applied in this study only allow to quantify the total amount of iron. Resulting mineral assemblages will be compared to the observed assemblages, and if needed the Fe^{2+}/Fe^{3+} ratio will be adjusted.

2.9 Ti-in-Quartz

The relationship between pressure and temperature and the Ti content of quartz, based on the substitution of Ti for Si, have been experimentally established by Wark and Watson (2006), Thomas et al. (2010), and Huang and Audétat (2012). Subsequent research found a good agreement between results obtained using traditional methods and Ti-in-Quartz thermobarometry (TitaniQ) for metamorphic rocks exceeding upper greenschist facies (e.g. Pennacchioni et al., 2010; Grujic et al., 2011, and references therein). Applicability of the calibration of Thomas et al. (2010) to lower-grade rocks - well below the calibration ranges - has been challenged (by e.g. Grujic et al., 2011; Ashley et al., 2014), and it was suggested temperatures obtained using this calibration are systematically and significantly too low. The alternative calibration, also based on laboratory experiments, proposed by Huang and Audétat (2012) results in temperature estimates of $\pm$ 100 °C higher.

For Ti concentrations to reflect deformation conditions and not those of the original quartz formation, quartz needs to re-equilibrate with a Ti-bearing phase. Studies by e.g. Grujic et al. (2011) and Kidder et al. (2013) have shown that dynamic recrystallization is

able to reset Ti concentrations in quartz. Where Grujic et al. (2011) postulates only grain boundary migration (GBM) to fully reset Ti content, later research by Ashley et al. (2014) and Nachlas et al. (2018) suggest that bulging (BLG) and subgrain rotation (SGR) are also able to reset Ti content.

In the TitaniQ calibration of Thomas et al. (2010) the activity of titanium (a_{TiO_2}) exerts a major control on the calculated conditions. In rutile bearing rocks a_{TiO_2} is generally taken as 1, however a_{TiO_2} can vary drastically a function of rock chemistry and mineral assemblage as is highlighted in a review of Ashley and Law (2015). In light of the ongoing debate regarding the TitaniQ calibration choice, the calibrations of both Thomas et al. (2010) and Huang and Audétat (2012) will be applied in this study and results are compared with independent PT estimates. Based on the bulk rock composition and observed mineral assemblage an appropriate a_{TiO_2} estimate will be obtained from literature.

As the Ti content in quartz correlates well with the cathodoluminescence (CL) peak at 2.72 eV - corresponding to a wavelength of 456 nm - (Leeman et al., 2012), selected samples were CL imaged at high magnification in order to determine Ti variability and select measurement spots. CL imaging was done on a Zeiss Gemini 450 variable pressure SEM equipped with a Delmic SPARC CL detector. The CL detector was fitted with pass-through filters, and using the 400-500 nm filter allowed to image only the relevant part of the CL emission spectrum. Selected regions were imaged using all available filters in order to verify variations in CL intensity did not originate from overlapping CL emission peaks. Simultaneously secondary electron (SE) images were acquired. Having both a CL and SE image of the same region greatly helped with the (automated) stitching of the 500-1100 separate tiles to produce CL intensity maps as the SE images provide a sharp contrast based on surface topography.

Ti concentrations were analyzed by secondary ion mass spectrometry (SIMS) on a Cameca IMS 4f at the NERC Ion Micro-Probe Facility of the University of Edinburgh. As navigation in the SIMS measurement chamber is done using a camera working with reflected light high resolution reflected light scans were made of the thin sections which were marked with the desired measurement locations based on the earlier obtained CL maps. The selected domains were then drilled out as 24 mm discs after the carbon coating from earlier analysis was removed. Prior to analysis the discs were re-coated with a gold film.

The samples were analyzed using a primary ion beam $^{16}O^-$ at an accelerating voltage of 5 kV and initially a beam current of 5 nA, resulting in a spot size of 10 µm. The following isotopes were measured: ^{27}Al, ^{30}Si, ^{40}Ca, ^{48}Ti and ^{49}Ti. The initial analyses contained several cycles with anomalously high Ti concentrations, possibly due to rutile inclusions, after which the beam current was reduced to 2 nA giving a spot size of 5 µm. In order to obtain a good precision on ^{48}Ti it was decided to drop ^{49}Ti, which was initially measured to correct for overlap between ^{48}Ti and ^{48}Ca but the initial analyses showed correction for this overlap to be minimal. Correction was subsequently done based on the measured ^{40}Ca. Four different quartz samples with known Ti concentrations, including a blank, were analyzed prior to each session or after changing measurement conditions and used to reduce the data.

Cycles with unexpectedly high Ti or low Si concentrations were filtered out, the measured ^{27}Al and ^{40}Ca were used to check for inclusions and Ti concentrations were normalized against 100 wt% SiO_2.

3 Results

TABLE 3.1: Overview of samples and analyses performed.

Rock type	Sample loc.[1]	Sample	TS[2]	OM[3]	SEM	SEM-AM	XRF	LA-ICP-MS	EPMA	EBSD	Perple_X	CL	Ti-in-Q
High T schist	2	CC97-9		X	X	X	X	X			X		
Deformed schist	1	MD95CC	.1	X	X	X	X	X	X		X	X	X
			.2	X									
			.3	X						X		X	X
			.4	X			X	X					
		564W	1	X									
			2	X									
			3	X									
Sheared pegmatite	3	BB1B		X	X	X	X				X		
		BB2B	I	X	X	X	X						
			II	X									
			III	X									
			IV	X									
		B1B		X	X								
Quartzite	4	FR3		X						X		X	X

[1] Sample localities correspond to figure 1.3.
[2] TS: Thin Section.
[3] OM: Optical Microscopy.

In this work a total of 15 thin sections have been studied. Table 3.1 provides the reader with an overview of all studied thin sections and the applied analytical and numerical methods.

3.1 Sample Description

3.1.1 Undeformed high-grade schist

Sample CC97-9 was obtained in the transition from the sillimanite-muscovite zone to the sillimanite-K-feldspar zone and is characterized by an assemblage of quartz, biotite, muscovite, plagioclase (oligoclase, as determined by EDS measurements) and sillimanite. Accessory minerals include apatite, monazite, xenotime, zircon, ilmenite and other oxide minerals. Relicts of andalusite crystals are observed in aggregates of muscovite. Quartz and biotite form large aggregates, with plagioclase often present between these and the muscovite aggregates and associated with minor quartz. Sillimanite, in the form of fibrolite, is restricted to the biotite- and quartz rich domains. Precipitation of a dark-red phase, associated with cracks more or less parallel to the foliation, results in the local overprinting of minerals along their grain boundaries.

3.1.2 Deformed schists

Mineralogy and microstructure

Thin section sets W564 (three thin sections) and MD95CC (four thin sections) have been cut from the same sample.

These deformed schist samples contain abundant and strongly folded quartz layers of varying thickness. The thicker (up to 1 cm) layers generally do not contain any other minerals, however occasionally plagioclase, andalusite or tourmaline crystals are imbedded. Quartz microstructures are indicative of dynamic recrystallization by means of subgrain rotation (SGR). In some of the thicker quartz bands a ribbon-structured core is preserved. The nature of the foliation is wavy as a result of shear bands on multiple scales.

Based on the mineralogy three distinct domains can be distinguished:

- Fine-grained muscovite, in places reacting to chlorite, spatially associated with and often imbedded in thick quartz bands. Can contain plagioclase porphyroclasts.
- Fine-grained muscovite and chlorite containing numerous tourmaline crystals often with strain shadows and tails composed of chlorite. Quartz and plagioclase are sparse. Spatially associated with thick quartz bands (figure 3.1).
- Fine-grained biotite, chlorite, epidote and to a lesser extent muscovite containing abundant sigmoidal plagioclase (andesine, determined by EDS measurements) porphyroclasts up to 400 µm, numerous (thin) isolated quartz bands (figures 3.1 and 3.2). Particularly the MD95CC thin sections are rich in tourmaline (figure 3.1).

SEM images (figure 3.3) reveal that biotite and muscovite stably coexist in the domains rich in quartz and plagioclase, and that quartz is being overprinted by biotite. In tourmaline-rich domains muscovite is dominant and the tourmaline crystals leave trails of chlorite ($\pm$ epidote) replacing muscovite. Occasionally biotite precipitates in the strain shadows of tourmaline crystals, and many plagioclase porphyroclasts are overgrown by biotite in strain shadows. Epidote is in parts unstable and overgrown by biotite or muscovite.

In all thin sections some biotite and muscovite crystals up to 200-300 µm in size are present, and in the 564W thin sections up to 750 µm (muscovite) or larger (biotite). Isolated andalusite crystals, up to 1 cm in size, are observed in most thin sections. Both samples contain tourmaline up to 400 µm, which is especially abundant in some muscovite-rich regions of thin sections MD95CC.1 and -.2. Accessory minerals include apatite, monazite, zircon, ilmenite and iron oxide minerals.

Most of the thin sections contain µm-scale fractures that follow shear bands and run more or less parallel to the foliation. Phosphate precipitation in these fractures result in a dark or reddish overprinting of minerals in places (figure 3.2).

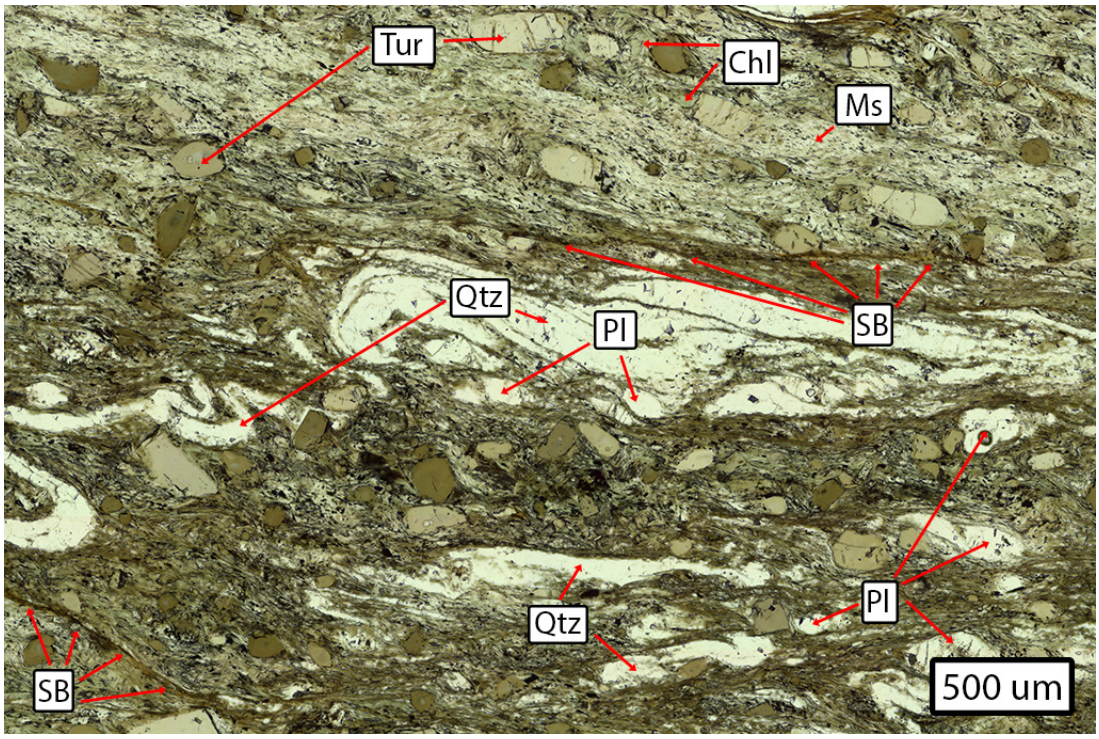

FIGURE 3.1: Photomicrograph of thin section MD95CC.1. Matrix in the top 1/3 of the image consists of fine-grained chlorite (Chl) and muscovite (Ms) containing tourmaline (Tur) with chlorite strain shadows. The bottom 2/3 contains quartz (Qtz), plagioclase (Pl) and tourmaline in a fine-grained matrix of biotite, chlorite, epidote and muscovite. Note the dark-colored shearbands (SB).

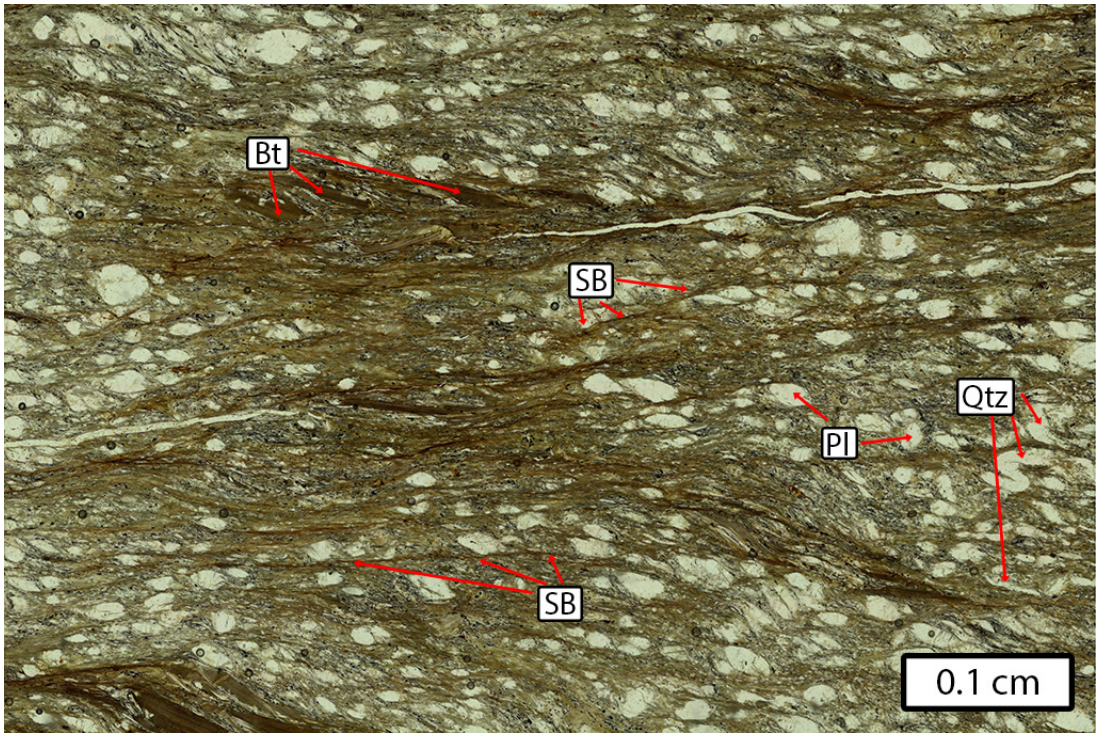

FIGURE 3.2: Photomicrograph of thin section W564.3 showing numerous shearbands (SB), plagioclase (Pl) porphyroclasts, larger biotite (Bt) crystals and isolated quartz (Qtz) bands.

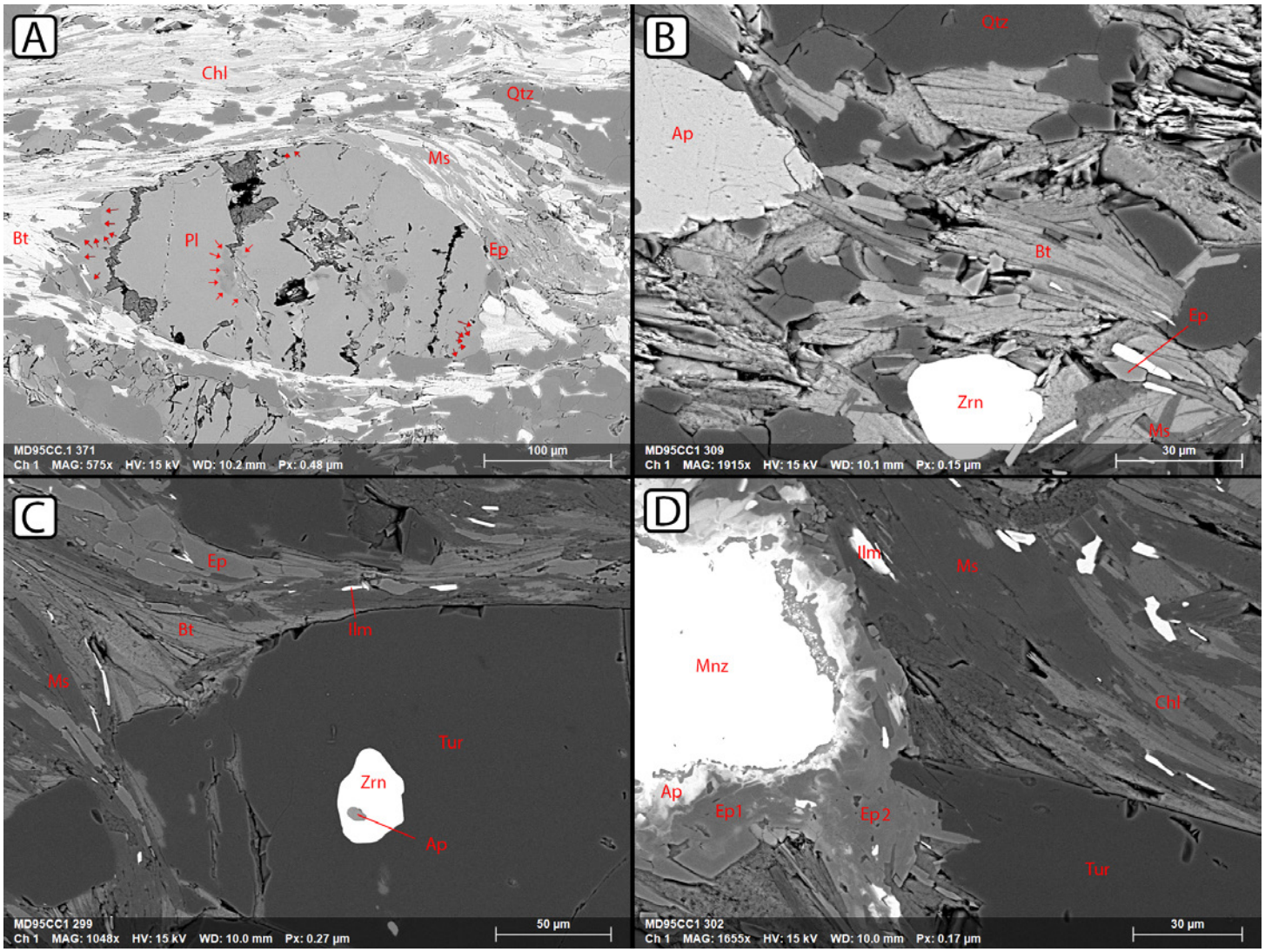

FIGURE 3.3: BSE images of thin section MD95CC.1. (**A**) Plagioclase porphyroclast, in strain shadows being replaced by biotite. Arrows show chemical zoning. (**B**) Biotite coexisting with muscovite and biotite overprinting quartz in the plagioclase- and quartz-rich domains. (**C**) Biotite and epidote replacing muscovite. Biotite in the strain shadow of tourmaline. (**D**) A rim of apatite and epidote (Ep1: high Fe, Ep2: low Fe) around unstable monazite (Mnz), and muscovite reacting to chlorite. The outer epidote rim is partly overgrown by muscovite.

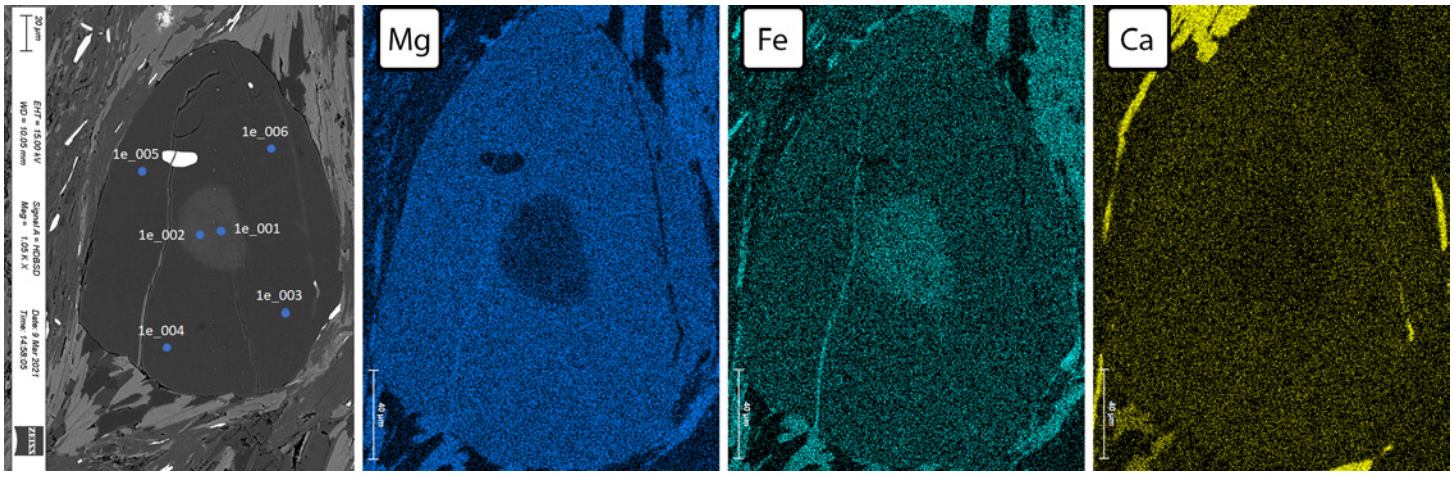

FIGURE 3.4: Chemical zoning in a selected tourmaline grain. **Left:** BSE photomicrograph. **Other images:** EDS element maps where brightness qualitatively shows concentrations of respectively Mg, Fe and Ca. For quantitative measurements refer to table 3.3, where central domains with low Mg & Ca and high Fe are defined as core.

TABLE 3.2: Mineral chemistry in oxide weight percentages for sample MD95CC from EDS spot measurements. The second column lists the relative standard deviation (RSD) in % for major elements.

	Biotite (n=8)		Chlorite (n=16)		Epidote (n=14)		Muscovite (n=18)		Plagioclase (n=32)		Quartz (n=7)		Tourmaline (n=10)	
SiO_2	35.06	3.49	26.89	3.54	37.51	0.73	47.77	1.5	57.89	4.15	99.40	0.9	40.12	2.63
Al_2O_3	18.65	3.37	23.83	1.41	29.63	1.19	37.32	2.87	26.89	6.12	0.35		39.80	1.85
Fe_2O_3	24.08	6.52	30.92	3.95	6.58	7.98	2.07		0.27		0.13		7.93	22.8
MgO	11.58	3.38	17.36	2.8	0.05		0.86		0.22		0.03		8.15	10.4
CaO	0.01		0.04		25.69	0.87	0.01		7.10	35.1	0.01		1.10	
Na_2O	0.09		0.11		0.01		0.87		7.37	12.8	0.03		2.05	
K_2O	8.72	11.6	0.42		0.02		10.30	1.69	0.19		0.00		0.02	
TiO_2	1.64		0.11		0.10		0.75		0.03		0.01		0.79	
MnO	0.16		0.32		0.41		0.04		0.01		0.00		0.04	

TABLE 3.3: Differences in tourmaline core and rim chemistry from EDS spot measurements on selected grains from sample MD95CC. Values are in normalized atomic mass %. Boron could not be measured due to its low atomic mass.

	n	Oxygen	Sodium	Magnesium	Aluminium	Silicon	Phosphorus	Potassium	Calcium	Titanium	Iron
Core	10	49,82	1,49	2,24	19,50	17,21	0,01	0,02	0,31	0,41	8,97
Rim	22	50,83	1,33	4,57	19,68	17,45	0,01	0,01	0,87	0,54	4,71

Mineral chemistry

EDS spot measurements show that in sample MD95CC mineral chemistry is fairly homogeneous: for most minerals the variation in major element concentrations is well below 10% RSD (table 3.2). The iron to magnesium ratio in biotite varies between 0.98 and 1.09, averaging at 1.04 and when spatially associated with ilmenite biotite contains $\pm$ 30% more Ti. In chlorite the Fe/Mg-ratio ranges between 0.83 and 1.00, with an average of 0.91. The Fe/Al-ratio in epidote is 0.14 $\pm$ 0.02 and thus falls as 0.28/0.72 between the epidote and (clino)zoisite end-members. Epidote rims around unstable monazites have a notably higher Fe content and classify towards the epidote end-member.

Plagioclase core compositions are consistently measured as intermediate between the albite and anorthite end-members, classifying as andesine (figure 3.5). Potassium concentrations are negligible with the exception of a rare plagioclase (grain 1-1-5) located in a feldspar-poor muscovite band imbedded in quartz and a single measurement of a plagioclase rim (grain 4a measurement 8, likely caused by a mixed biotite/plagioclase signal).

SEM images show a slight contrast between the cores and rims of most plagioclase porhyroclasts (figure 3.6). Multiple EDS measurements on a selected grain (grain 4a) show a distinct difference between core and rim Na/Ca ratio: where the core is of andesine composition, the rim classifies as oligoclase. Some grains contain fractures along which a similar zoning is observed (figure 3.3A). EDS element maps show a sharp interface with regard to sodium and calcium concentrations.

Many of the tourmaline cores in MD95CC.1 exhibit a slight blue color under the optical microscope. Measurements reveal that cores have a chemically distinct signature compared to their outer rims: cores are low in Mg, Ca and Ti and high in Fe (figure 3.4 and table 3.3).

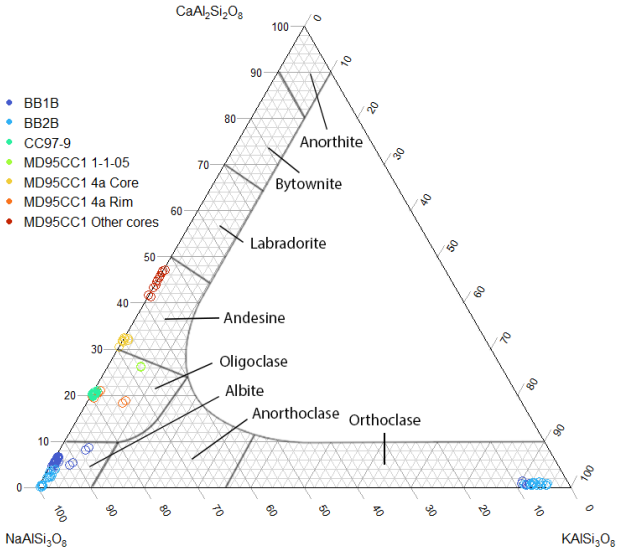

FIGURE 3.5: Measured feldspar compositions for sample CC97-9, the deformed schists (MD95CC) and sheared pegmatites (BB1B & BB2B).

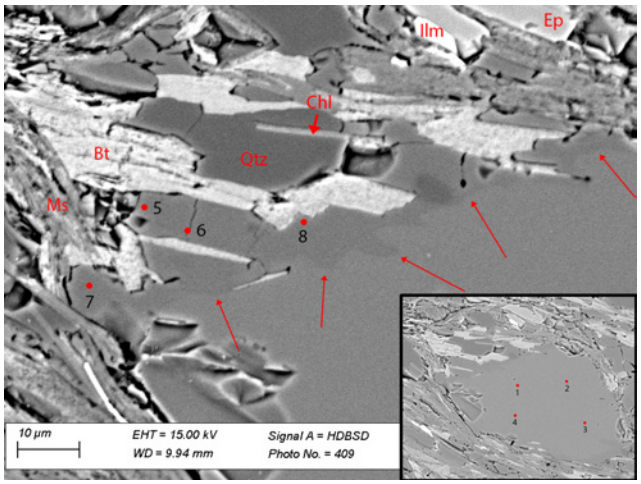

FIGURE 3.6: Chemical zoning (indicated by red arrows) in plagioclase grain 4a. The inset shows the whole grain. Red dots indicate EDS measurement spots.

3.1.3 Sheared pegmatites

Mineralogy and microstructure

Samples BB1B (one thin section), BB2B (five thin sections) and B1B (one thin section) belong to the same shear zone and can both be characterized as mylonites containing up to cm-sized clasts of albite in a fine-grained matrix of the same mineral, with additional quartz and muscovite in varying proportions (figure 3.8). Many of the albite clasts have been fractured into smaller fragments and rotated, forming bookshelf and mosaic structures while some grains have a sigmoidal shape. Albite clasts contain fine-grained inclusions of muscovite and apatite. The samples contain larger (up to 200 µm) fish-shaped muscovite crystals that have an orientation inclined to the foliation, with their (recrystallized) tails sheared into the foliation (figure 3.8 C).

Most feldspar is in the form of albite, however AM-mapping (section 3.2.1) and EDS measurements have revealed that both samples contain a limited number of bands with orthoclase clasts in a matrix of orthoclase, quartz, albite or a combination of these minerals. Additionally, some thin and fine-grained orthoclase rich bands are present. EDS measurements of feldspar compositions are shown in figure 3.5.

In BB2B banding is more pronounced compared to sample BB1B. In the latter albite clasts of varying size are contained within a matrix of smaller feldspar clasts and quartz, with parallel running thin (10-100 µm) and fine-grained muscovite-rich bands that contain fewer clasts and are alternated with monomineralic quartz bands (figure 3.8 A). Remarkable is one thicker band ($\pm$ 1 mm) of very fine-grained (2-10 µm) muscovite, K-feldspar (orthoclase, as determined by EDS measurements), quartz and iron-oxide (figure 3.8 A & F). Quartz bands in BB1B are generally composed of equant grains of $\pm$ 20-30 µm. Quartz grain boundary morphology indicates dynamic recrystallization by means of SGR, however in some bands elongated ribbon cores exhibiting undulatory extinction are preserved. Several micro shearbands and brittle fractures at a high angle to the foliation are present,

the latter sometimes filled with a (presumably) phosphate phase.

BB2B consists of thick (up to 0.5 cm) bands composed almost completely of albite fragments that are either alternated with quartz bands of varying thickness (100 µm to 0.5 cm) or with thin bands of fine-grained muscovite. Unlike the other thick bands, one band (0.2 cm) that is composed of a fine-grained mixture of albite, muscovite and quartz contains only a few (±5) larger albite clasts or fragments. A ± 0.2 cm thick band composed almost completely of fractured orthoclase fragments is located in the central part of the thin section, as well as with two smaller and more fine-grained K-feldspar and muscovite rich bands (figure 3.8 E). Many of the feldspars clasts, especially plagioclase, show signs of sericitization. Tourmalines of varying size (up to 0.2 mm) occur in specific bands, often in fractured fragments.

In contrast to BB1B, quartz bands in BB2B have more often than not retained their elongated ribbon structures and are only partially recrystallized. Three different quartz recrystallization stages can be recognized (figure 3.8 D):

- Aggregates of elongated grains (individual grains are ± 100 µm along their long axis) with polygon-shaped boundaries giving rise to a core-mantle structure.
- Complete recrystallization to a grainsize of ± 10 µm with microstructures consistent with dynamic recrystallization by bulging.
- The overprinting of the ribbon quartz and aforementioned structures with conjugate thin bands (50-100 µm) of fine-grained (± 10 µm)recrystallized quartz orientated at a high angle to the mylonitic foliation. Within the completely recrystallized quartz these bands can be recognized by a change in crystallographic-preferred orientation (CPO). These bands share their orientation with small brittle fractures that are present, often as conjugate sets, throughout the sample.

For both samples the accessory minerals include apatite, xenotime and zircon.

Sample B1B represents a different section of the same shear zone, and is in structural and petrological regard very similar to sample BB1B. This sample has been studied in less detail, but SEM images and EDS measurements have revealed the presence of sillimanite needles in a fine-grained deforming aggregate of albite and orthoclase (figure 3.7). Sillimanite appears to be spatially associated with the fine-grained albite.

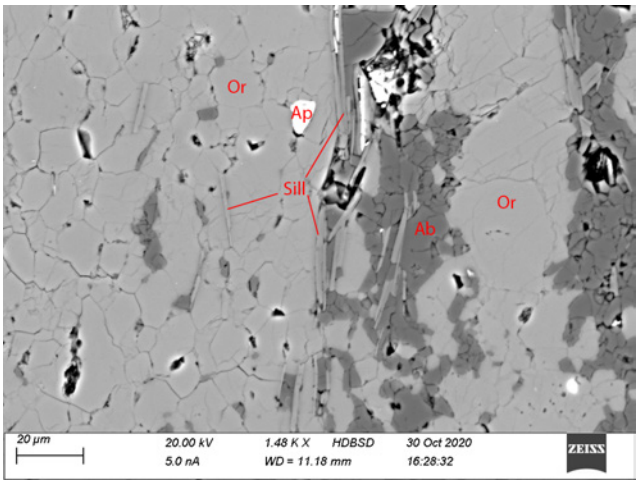

FIGURE 3.7: Photomicrograph of sample B1B where sillimanite (Sill) occurs within an aggregate of predominantly orthoclase (Or) and albite (Ab).

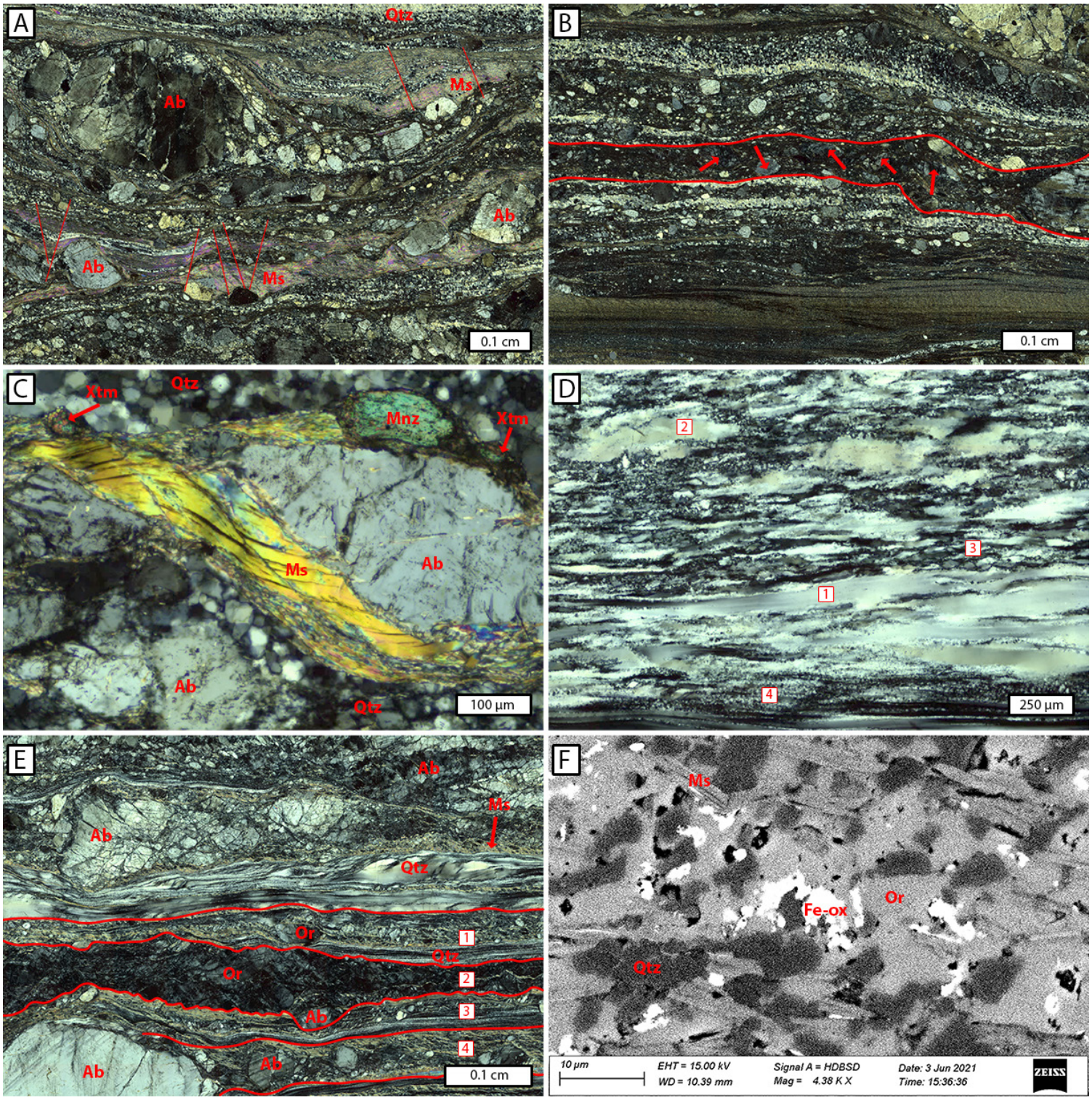

FIGURE 3.8: Photomicrographs with crossed polars of thin sections BB1B (A - C) and BB2B (D & E) and BSE image of BB2B (F). (**A**) Albite (Ab) clasts of varying size in a matrix of either finer-grained albite or muscovite, alternated with bands of fine-grained muscovite and quartz. Red lines trace small shearbands at a high angle to the foliation (**B**) Top: alternation of quartz, albite and muscovite rich bands. The band marked in red consists of orthoclase clasts (indicated with arrows) in a matrix of predominantly albite. Note the very fine-grained bottom band (for detail see (F). (**C**) Deformation structures and recrystallization textures in muscovite, including accessory phases monazite and xenotime (Xtm). (**D**) Different quartz (re)crystallization features including 1) ribbon quartz, 2) remnants of ribbons with subgrain development, 3) smaller elongated grains, 4) very fine-grained quartz. Along the boundaries of 1-3 fine grains have developed. (**E**) Top: quartz bands and fractured albite in a matrix of fine-grained muscovite. Numbered bands: 1) Orthoclase (Or) fragments in a mixture of fine-grained orthoclase, albite, muscovite and quartz, 2) predominantly orthoclase, with minor muscovite seperating the fragments and an occasional albite clast, 3) fine-grained orthoclase and muscovite and 4) albite clasts in a matrix of muscovite and orthoclase. (**F**) High magnification BSE image of the fine-grained band in (B), showing an orthoclase (Or), quartz, and an iron-oxide (Fe-ox) composition.

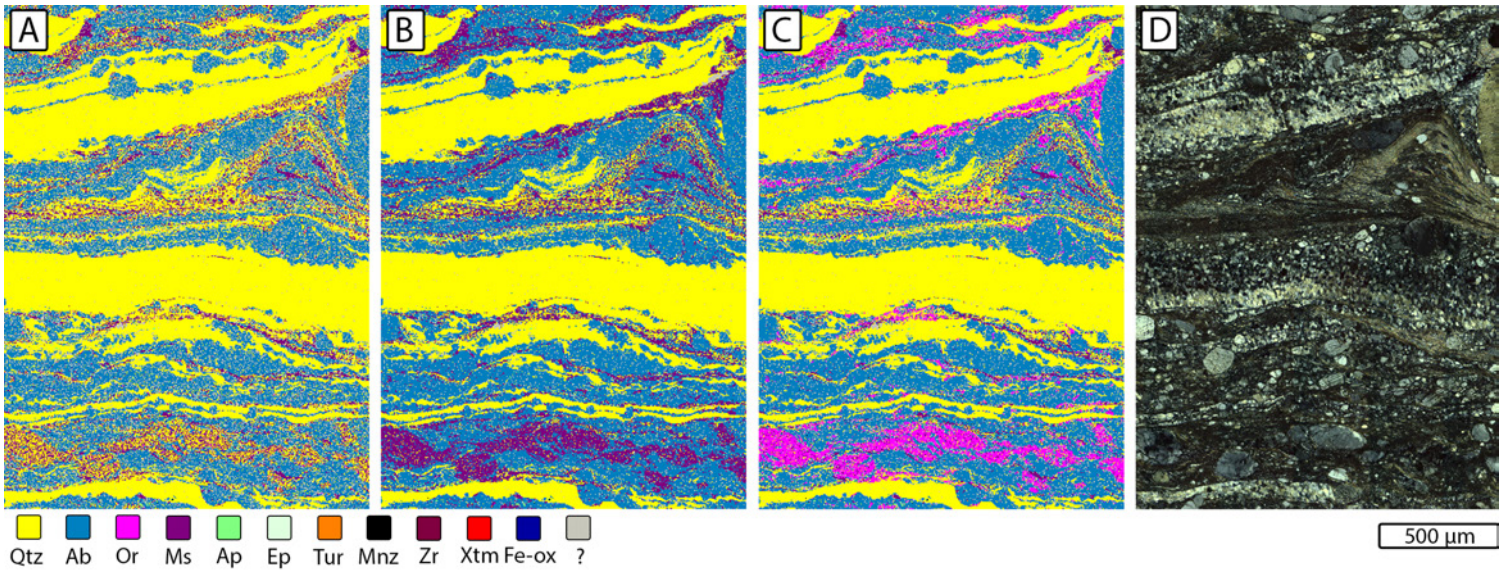

FIGURE 3.9: False color SEM-AM maps of a selected area in thin section BB1B calculated using different versions of the mineral recipe. Mineral abbreviations as in optical and BSE images. (**A**) The preliminary recipe: muscovite and orthoclase are not properly classified, and albite contains many misclassified pixels. (**B**) An intermediate version: albite and muscovite are now correctly classified, however orthoclase is classified as muscovite. (**C**) The result of the final recipe with a good separation of albite, muscovite and orthoclase. (**D**) XPL view of the mapped area for comparison.

3.2 Automated Mineralogy

For the initial analyses a preliminary mineral recipe was used and results were compared to the optical microscopy and BSE images after which the mineral recipe was fine-tuned. The initial measurements were subsequently reclassified by performing a retrospective analysis using the updated mineral recipe. For both the schists and sheared pegmatites this process was repeated 7-8 times in order to classify most of the pixels correctly while keeping the unclassified and mis-classified pixels to a minimum. When minerals share major elements in similar concentrations, as for example is the case with muscovite and orthoclase, and when grain sizes are of similar size (or smaller) as the step size this can be challenging. An example of these incremental improvements in mineral recipe are illustrated in figure 3.9. Thin sections CC97-9, MD95CC1, BB1B and BB2B have been (partially) SEM-AM mapped. The calculated modal mineralogy based on the SEM-AM data for these samples is listed in table 3.4.

TABLE 3.4: Modal mineralogy in wt % as calculated from the SEM-AM data.

	Qtz	Ms	Bt	Pl [1]	Or	Tur	Chl	Ep	Ilm	Ap	Zrn	Mnz	Fe-oxide	Unclassified
MD95CC.1	20,0	17,6	14,7	10,8	<0,1	8,8	8,4	6,3	1,7	0,4	0,1	<0,1	<0,1	9,9
BB1B	35,2	7,4	0,0	44,1	4,6	0,0	0,0	0,0	0,0	0,4	<0,1	0,2	<0.1	8,1
BB2B	33,4	5,6	0,0	48,2	3,5	2,4	0,0	0,1	0,0	0,7	<0,1	0,2	<0,1	5,8
	Qtz	Ms	Bt	Pl	Sill [2]	Tur	Ap	Ilm	Zrn	Mnz	Fe-oxide			Unclassified
CC97-9	27,5	23,4	30,9	12,1	2,40	0,7	0,6	0.1	<0,1	<0,1	0,3			1,9

[1] Plagioclase in MD95CC.1 is of andesine/oligoclase composition, plagioclase in BB1B & BB2B is of albite composition. Abbreviations as in BSE images.
[2] Sillimanite includes relict andalusite.

3.2.1 SEM-AM Observations

SEM-AM mapping has revealed some features that are difficult to observe using traditional microscopy or BSE images when grainsizes are small, optical properties are similar or Z-contrast is limited: the false color maps clearly visualize mineral associations, mineral reactions and structural features without having to resort to high magnification imagery and losing the overview. The following text can be considered as an addition to the sample description (section 3.1).

CC97-9

While the SEM-AM false color map of thin section CC97-9 (figure 3.10) itself does not reveal any new information it does provide a clear overview of the mineralogy and relationships between different phases: quartz is associated with biotite forming large intergrows with occasional sillimanite, muscovite aggregates contain relict andalusite, and some clusters of isolated biotite occur. Plagioclase is generally observed in margins between biotite and muscovite.

MD95CC.1

The SEM-AM map of thin section MD95CC.1 (figure 3.10) shows the association of chlorite with tourmaline, often in the form of trails and originating from strain shadows. Zooming in reveals that biotite forms in the strain shadows of plagioclase porphyroclasts, and somewhat less often in the strain shadows of tourmaline grains. While plagioclase also occurs elsewhere, most of the clasts are located in quartz and biotite rich domains.

Within the SEM-AM mapped region, three different domains can be recognized:

- The top of the map is composed of tourmaline grains (and associated chlorite) in a matrix of mostly muscovite with minor epidote.
- In the central left part and below the top quartz-rich band, tourmalines with chlorite trails are still abundant but now within a more biotite-rich matrix and with occasional plagioclase clasts.
- The quartz and plagioclase rich bottom (right) domain, where quartz bands of varying size are alternated with biotite and to a much lesser extend muscovite with minor epidote. Tourmalines are smaller and less abundant, and sporadically some apatite can be observed.

Figure 3.12 shows that the different domains can be observed based on the spatial distribution of muscovite, biotite and chlorite and illustrates how SEM-AM false color maps can contribute to sample characterization by providing an overview of the distribution of fine-grained minerals on the scale of a thin section.

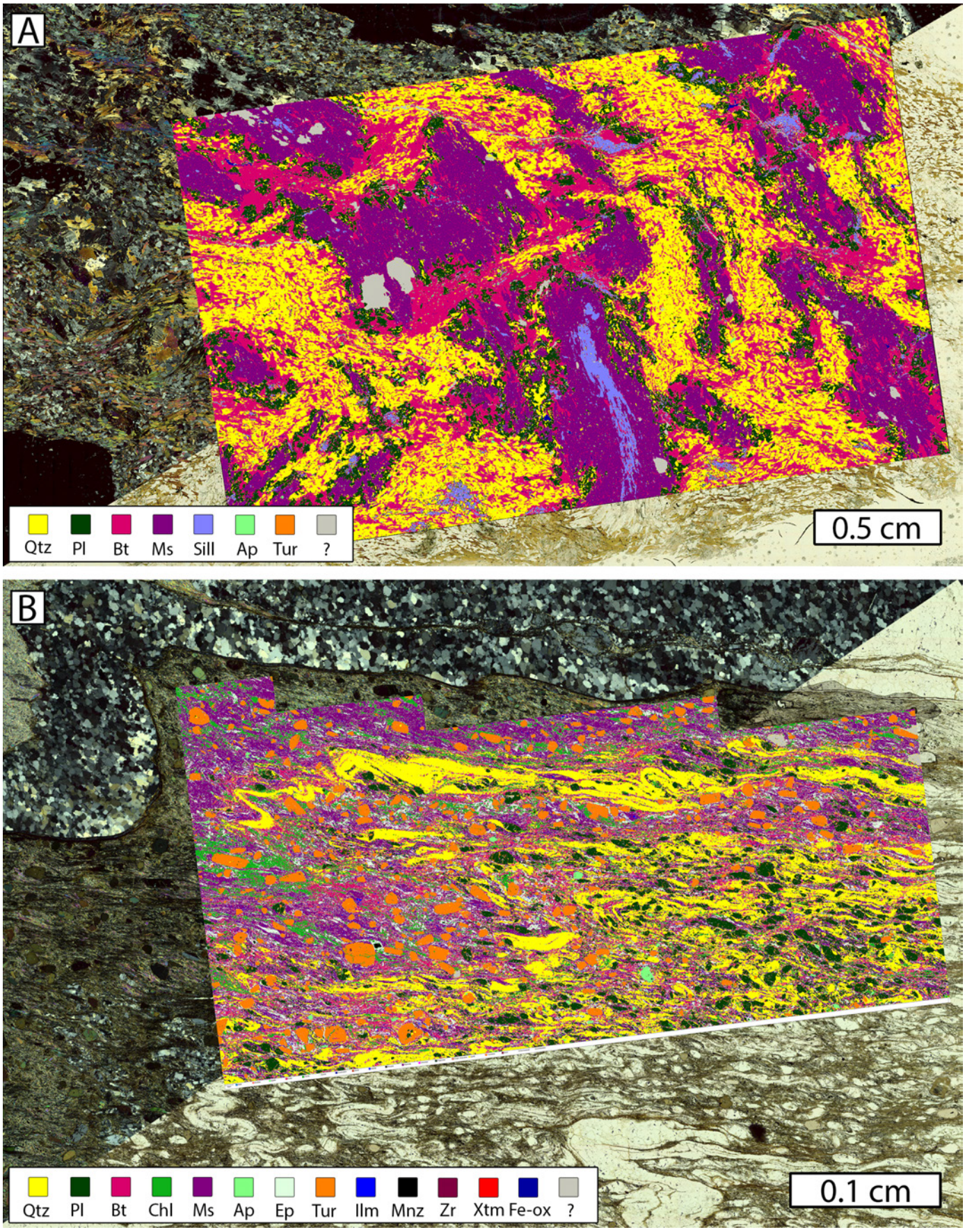

FIGURE 3.10: False color SEM-AM maps as overlay on XPL and PPL view. (**A**) thin section CC97-9. Note that sillimanite includes the andalusite relicts within muscovite aggregates. Large unclassified areas are holes. (**B**) a selected area of thin section MD95CC.1.

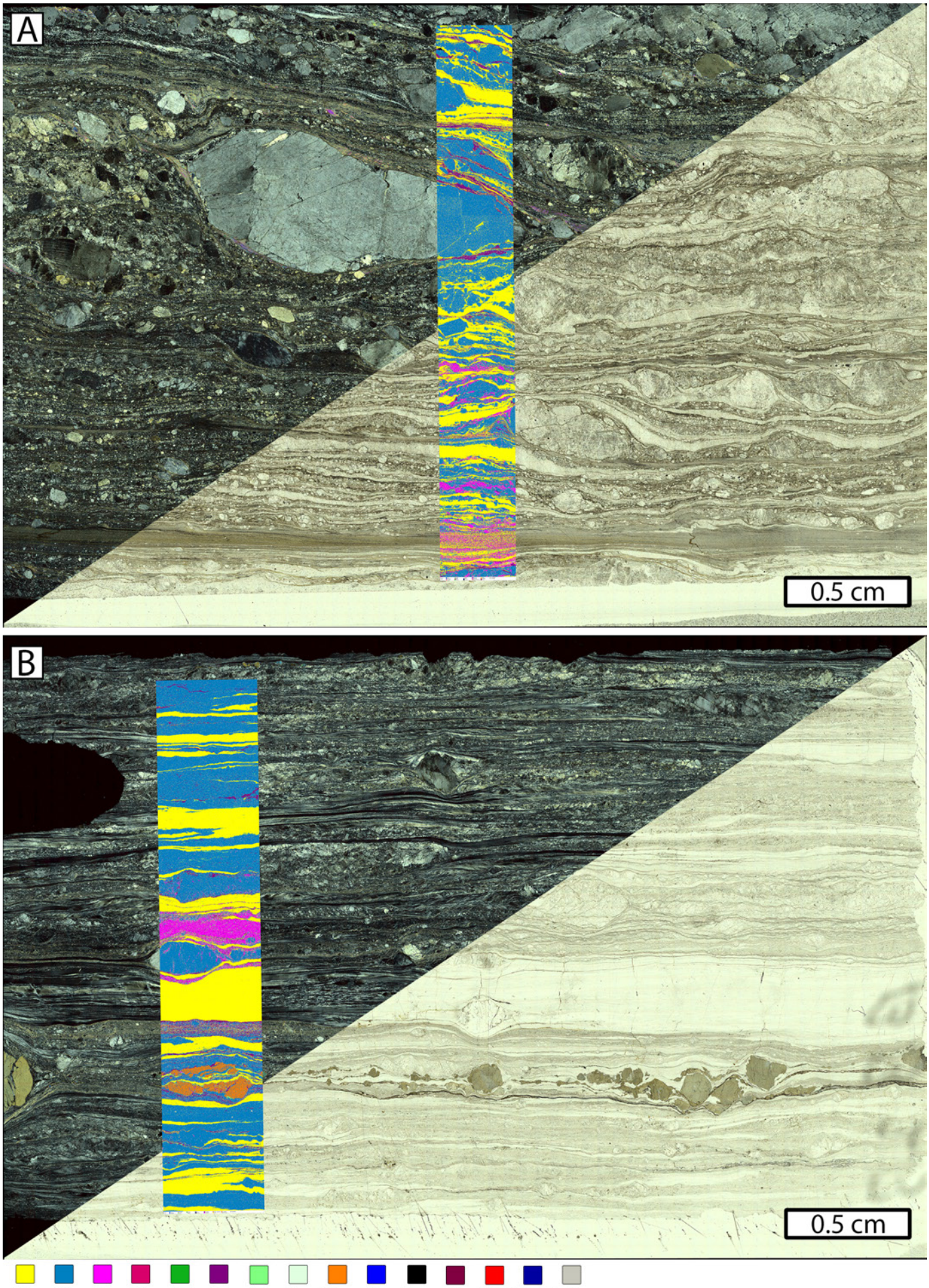

FIGURE 3.11: False color SEM-AM map overlay on XPL and PPL view. (**A**) Thin section BB1B. (**B**) Thin section BB2B.

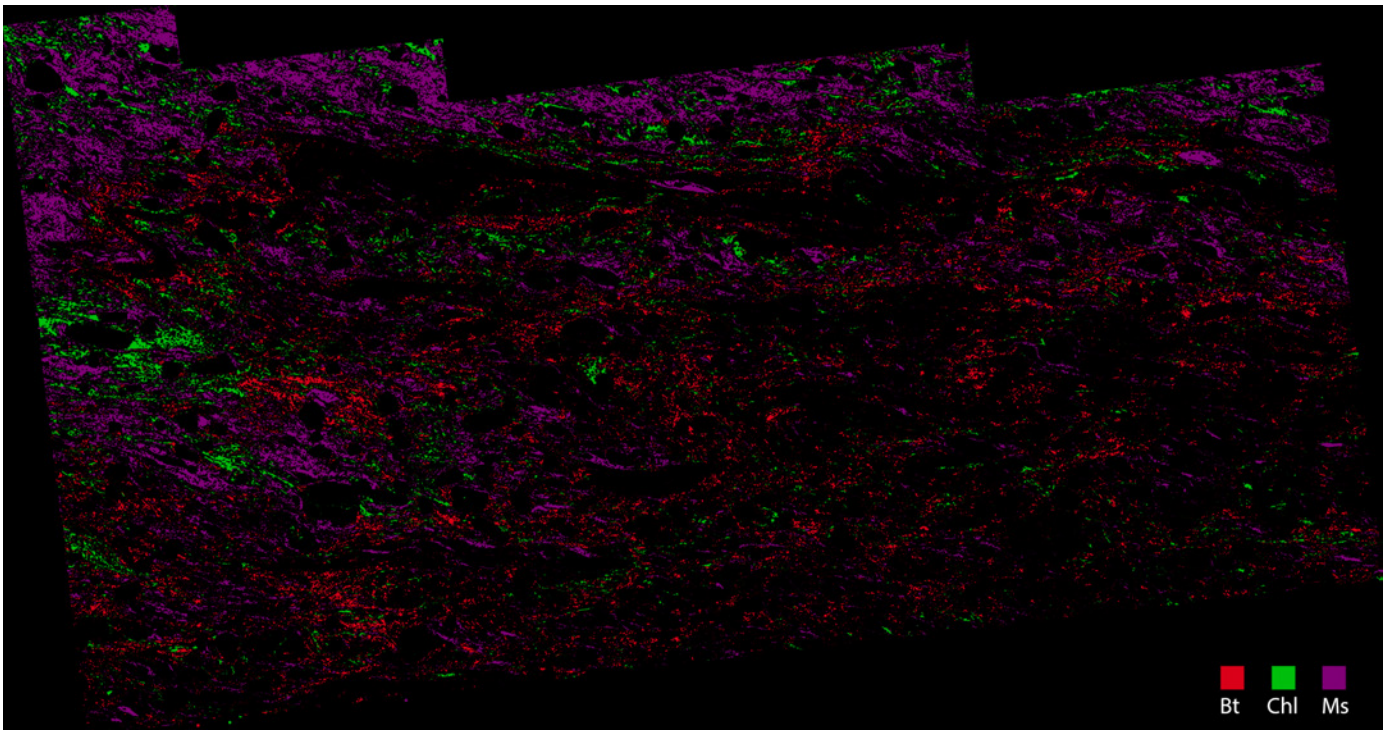

FIGURE 3.12: False color map of thin section MD95CC.1 showing the spatial distribution of biotite, muscovite and chlorite.

BB1B & BB2B

SEM-AM mapping of thin sections BB1B & BB2B (figure 3.11) shows that these samples consist mostly of alternating albite and quartz bands. In the albite-rich bands, (often fractured) albite porphyroclasts occur within a matrix of either fine-grained and fractured albite, quartz or muscovite. Noteworthy is the occurrence of orthoclase that is restricted to specific bands in both thin sections, and is present in the forms of:

- Sigmoidal clasts,
- A single band composed almost entirely of angular orthoclase fragments,
- A fine-grained matrix that can contain either, or both, albite and orthoclase clasts,
- The apparent reaction product of albite clasts precipitated in cracks and strain shadows, sometimes leaving orthoclase trails.

The false color maps also reveal that thin and fine-grained muscovite rich bands that are optically very similar can consist almost entirely of muscovite, or of a combination of muscovite, quartz, albite and orthoclase. Occasionally thin bands of apatite are observed.

3.2.2 Accuracy of EDS spot measurements

Table 3.5 compares EPMA WDS average results of measurements on tourmaline grains with SEM EDS measurements on the same grains. This table also lists averages of EPMA WDS and SEM EDS measurements on ilmenite, however these are not performed on the same grains. For both tourmaline and ilmenite EDS spot measurements are in good agreement with EPMA WDS measurements for major elements with relative differences of <5%. The same is true for Mg in ilmenite; other minor and elements cannot be meaningfully

TABLE 3.5: SEM EDS measurements compared to EPMA WDS measurements for ilmenite and tourmaline grains in normalized atomic mass %.

	Ilmenite				Tourmaline			
	mean EDS	mean WDS	% RSD [1]	% Error [2, 3]	mean EDS	mean WDS	% Error [3]	S [4](%)
Oxygen	32,92	31,66	0,4	4,0	50,65	52,28	3,1	-
Sodium	0,03	0,00	-	-	1,36	1,19	14,7	1,9
Magnesium	0,01	0,03	67,3	63,2	3,93	3,63	8,2	0,7
Aluminium	0,06	0,03	93,5	99,8	19,68	19,08	3,1	0,5
Silicon	0,07	0,05	71,7	33,2	17,37	16,55	5,0	0,5
Potassium	0,10	0,11	30,2	7,4	0,02	0,04	57,6	20,7
Calcium	0,09	0,02	154,0	464,5	0,71	0,73	3,1	1,1
Titanium	31,78	31,47	1,5	1,0	0,48	0,47	1,5	2,6
Manganese	2,77	2,86	9,0	2,9	NA	0,03	-	39,9
Iron	32,15	33,78	4,8	4,8	5,80	6,00	3,3	1,0

[1] As for ilmenite different grains are measured WDS/EDS comparison is only meaningful for elements with a low spread in measured values. This column lists a measure of spread in the values measured based on the WDS analyses.
[2] Values in gray correspond to a high spread in measured WDS values.
[3] For the relative error, EPMA WDS measurements are taken as reference values.
[4] EPMA WDS relative analytical sensitivity (at the 99% confidence level).

compared due to a high spread in concentrations measured in different grains. Relative differences in minor- and trace elements in tourmaline are generally well below 10% except for Na (14.7%) and K (57.6%). From comparison of the individual spots it can be concluded that EDS spot measurements are consistently 0.18-0.28 atomic wt% high in Na with respect to WDS analyses, averaging at 0.22 wt% on values that are in the order of 1.2 wt% Na. A similar picture emerges from comparing SEM EDS with EPMA WDS measurements in cordierite on a sample not discussed in this study. In case of K, EPMA WDS has a relative analytical sensitivity of $\pm$ 21% (due to the spectrometer configuration) and concentrations are in the order of 0.02-0.04 atomic mass %, therefore it is difficult to determine if there is a significant systematical error in the EDS measurements.

3.3 Whole-rock & trace element chemistry

Thin sections MD95CC.1 & -.4 contain large quartz bands. A band constituting $\pm$37% of thin section MD95CC.1 has not been included in the SEM-AM mapping and is corrected for in the XRF measurements, assuming this band is composed of pure SiO_2. The accuracy of the XRF results is questionable as relative errors for the measured standards are averaging $\pm$30% with respect to reported values, however the standard homogeneity and quality of standard characterization are unknown. Still, for samples CC97-9, BB1B and BB2B the XRF and SEM-AM data are in good agreement for major and minor elements. For trace elements in these samples, and most elements in MD95CC.1, there are substantial differences however. It is important to emphasize that thin sections MD95CC.1, BB1B and BB2B have only partially been SEM-AM mapped and that especially MD95CC.1 shows compositional heterogeneity on scales similar to the size of the SEM-AM map.

Samples CC97-9 and MD95CC (after correcting for excess SiO_2) differ mainly in CaO and K_2O content and are similar to an average pelitic composition (Mahar et al., 1997). The mylonitic pegmatites are high in Na_2O and low in K_2O compared to the data of Druguet et al. (2014) on undeformed Cap de Creus pegmatites.

TABLE 3.6: SEM-AM + EDS calculated BRC compared to XRF data and literature compositions.

	MD95CC.1			MD95CC.4	CC97-9		Lit [2]	BB1B		BB2B		Lit [3]
	AM	XRF [1]	XRF	XRF	AM	XRF		AM	XRF	AM	XRF	
SiO_2	53,29	58,34	73,90	72,71	58,39	59,98	59,80	75,08	75,17	74,12	73,74	74,56
Al_2O_3	22,29	17,32	10,85	11,66	20,37	18,58	16,57	14,89	14,19	15,53	15,05	15,03
Fe_2O_3	10,15	7,21	4,52	4,62	8,63	7,11	5,81	0,51	0,02	0,61	0,11	1,22
MgO	4,44	3,65	2,28	2,32	3,33	3,05	2,62	0,43	0,12	0,46	0,14	0,09
CaO	2,95	2,92	1,83	2,24	1,16	0,80	1,09	1,01	0,62	0,87	0,62	0,82
Na_2O	1,28	1,63	1,02	1,53	1,46	1,25	1,73	5,83	5,30	6,42	6,02	3,62
K_2O	3,92	3,03	1,90	1,92	5,49	4,87	3,53	1,77	2,30	1,53	1,77	3,94
TiO_2	1,39	0,82	0,51	0,43	0,93	0,82	0,75	0,10	0,01	0,07	0,01	0,03
MnO	0,20	0,13	0,08	0,08	0,14	0,09	0,10	0,31	0,01	0,33	0,02	0,04
LOI		1,52	1,52	1,42		1,76			0,64		0,64	

[1] To allow comparison with SEM-AM data XRF results for MD95CC.1 have been corrected to adjust for a quartz band (37% area of the rock dummy) not mapped in SEM-AM.
[2] Average pelite composition from Mahar et al. (1997).
[3] Undeformed Cap de Creus pegmatite composition from Druguet et al. (2014).

When normalizing the oxides against SiO_2 an enrichment in Ca, depletion in K and possibly a minor depletion in Fe are observed for the deformed schists compared to sample C97-9. Note that only the K_2O contents of CC97-9 deviates from the trend set in other high-temperature schists that are not discussed (appendix D).

Using LA-ICP-MS and XRF data the (trace) element ratios between the deformed schists (MD95CC.1 & -.4) and the reference schist (CC97-9) were computed (figure 3.13). XRF oxide data was converted to ppm values. For all rare earth elements (REE) except Eu the concentration ratio, $\frac{C^1}{C^0}$ with C^1 as deformed schist and C^0 (sample CC97-9) as reference, lies between 0.55 and 0.75. For thin section MD95CC.4 the concentration ratios of the REE are consistently $\pm$0.05-0.10 lower than for thin section MD95CC.1. Under the assumption that in this case elements with ratios between 0.55 and 0.75 (i.e. similar to REE excluding Eu) are immobile, an average concentration ratio for both thin sections of 0.64 is calculated for immobile elements.

The HFSE elements display a less consistent trend: the Ti concentration ratios for both MD95CC.1 & -.4 are in line with those of the REE. For MD95CC.4 Zr, Nb, Hf and Th are also in the 0.60-0.70 range, while for MD95CC.1 these elements have an elevated ratio (0.80-1.0). This ratio is the inverse of the ratio in the total mass change expression, $T_{\text{mass,i}} = \frac{C^0{}_i}{C^1{}_i} - 1$ where $T_{\text{mass,i}}$ is the total rock mass change as calculated from the concentrations of element *i* in the reference rock C^0 and C^1 in the altered rock. For a derivation of this expression the reader is referred to Philpotts and Ague (2009). A value smaller than one implicates concentrations of this element were diluted due to the addition of other elements. Assuming certain elements to be immobile and using these as a reference then allows to determine which elements have been added or lost: elements plotting above the reference value of - in this case - 0.64 have been added and elements below it have been lost. For the measured elements that exceed trace level concentrations samples MD95CC.1 & -.4 are enriched in Si, Ca and Na, and depleted in K. By inserting the inverse of the average immobile element concentration ratio (0.64) in the mass change expression translates to a mass gain of $\pm$54%.

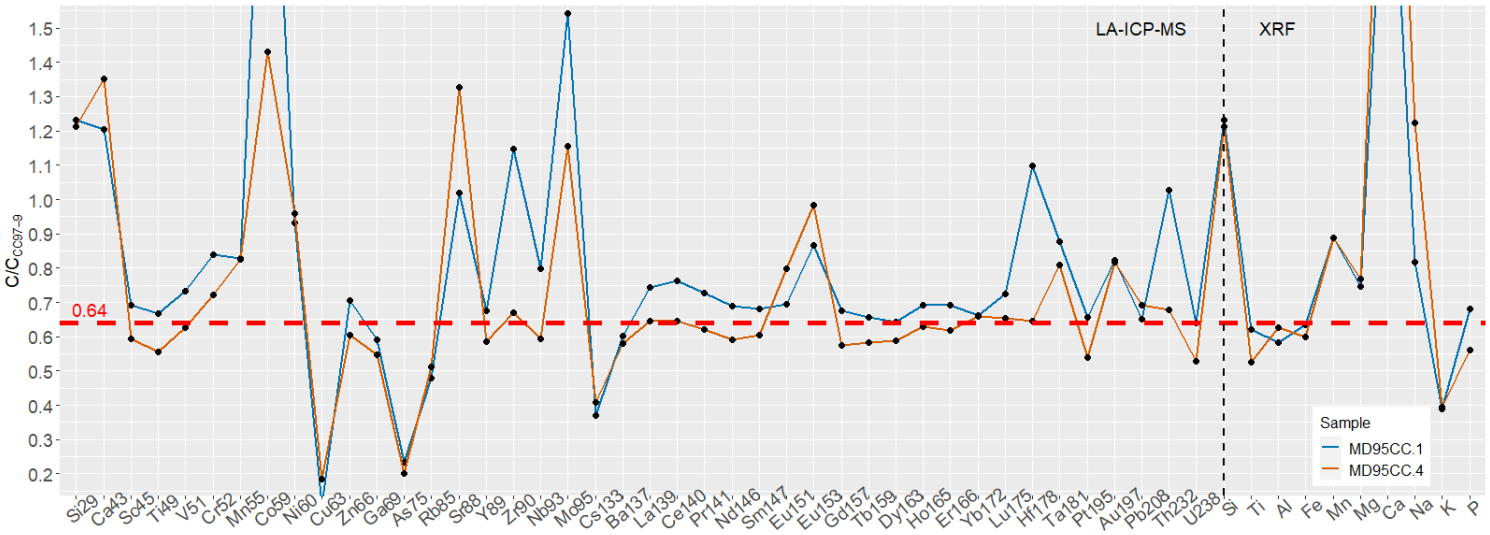

FIGURE 3.13: Concentration ratio diagram of samples MD95CC.1 & -.4 with respect to sample CC97-9. Dashed red line at 0.64 is considered the mean of presumably immobile elements and taken as reference line. Dashed vertical line separates data obtained using LA-ICP-MS (left) from XRF data (right). ^{59}Co at 2.4 and Ca at 2.3 and 2.8 for MD95CC.1. & -.4, respectively.

3.4 Thermodynamic modeling

Mineral assemblages specific for bulk rock compositions calculated with the integrated manual EDS and SEM-AM approach are modeled over a pressure range of 1-5 kbar and a temperature range of 300-600 °C (thin sections MD95CC.1 & BB1B) or 600-900 °C (thin section CC97-9). H_2O content modeling results predict water saturation is achieved at around 2-2.5 wt% for the schists and below 1 wt% for the pegmatites. In under-saturated conditions garnet and kyanite or andalusite are predicted for nearly all of the modeled PT-range in sample MD95CC. In dry pegmatites, sillimanite stability is predicted from 600 °C at 3 kbar, with stability occurring at lower pressures with increasing temperature (outside the here plotted PT-range).

As garnet, kyanite and andalusite are not observed as part of the equilibrium assemblage in sample MD955CC it is assumed that the assemblage formed at (nearly) saturated conditions. This is supported by the XRF loss on ignition values (table 3.6), which tends to slightly underestimate the volatile contents, and are close to the modeled H_2O saturation values for the considered samples. Therefore, all pseudosections are modeled assuming fluid-saturated conditions. The calculated mineral assemblages for thin sections MD95CC.1 with $X_{Fe^{3+}} = 0.25$, where $X_{Fe^{3+}} = Fe^{3+} / (Fe^{2+} + Fe^{3+})$ are shown in figure 3.14A, and for CC97-9 in figure 3.14B. Calculated mineral assemblages for MD95CC.1 with $X_{Fe^{3+}} = 0.05$ and BB1B are presented in figure 3.15A and 3.14B, respectively.

The observed mineral assemblage in sample CC97-9 of Qtz + Bt + Ms + Pl + Sil is predicted as an equilibrium assemblage in a single field at 650±30 °C and >±3.9 kbar (figure 3.14B), being constrained by the sillimanite in- and muscovite out reactions. Measured feldspar compositions for this sample (78Ab/22An) are close to the calculated 65Ab/32An/3Or, whereas right of the muscovite out reaction K-feldspar is predicted.

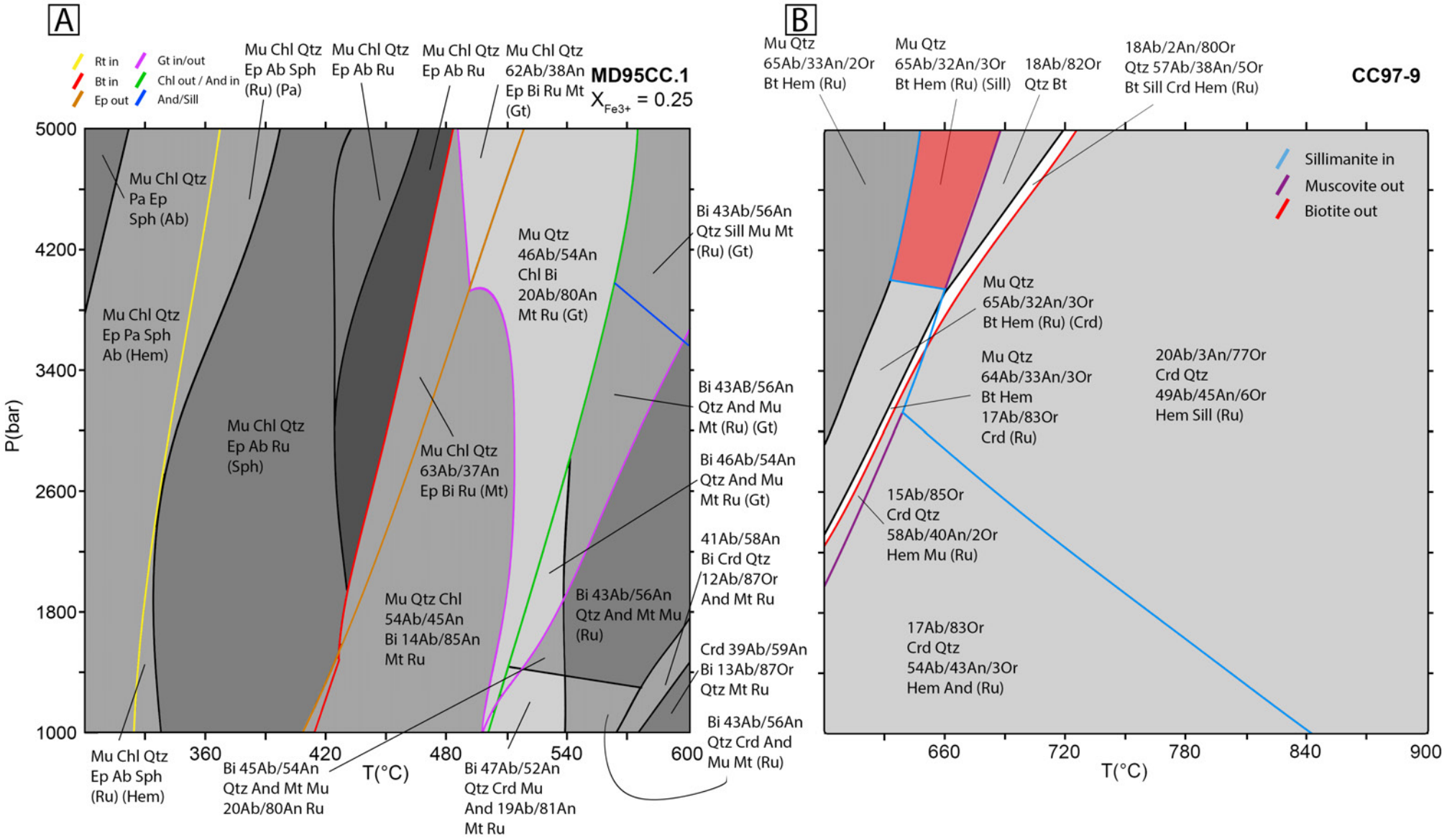

FIGURE 3.14: Pseudosections for (**A**) thin section MD95CC.1 and (**B**) CC97-9 with in red the field containing the observed mineral assemblage, based on their specific BRC, calculated in the MnNCKFMASHT chemical system under H_2O saturated conditions using the thermodynamic database of Holland and Powell (2011). MD95CC.1 is modeled with 25% of Fe as Fe^{3+}. Phases are listed in order of modal proportions, in brackets when <1 wt%. Variance increases from light to dark. Ab = albite, An = anorthite, And = andalusite, Bt = biotite, Chl = chlorite, Crd = cordierite, Cz = clinozoisite, Ep = epidote, Gt = garnet, Hem = hematite, Mt = magnetite, Mu = muscovite, Or = orthoclase, Pa = paragonite, Pre = prehnite, Qtz = quartz, Ru = rutile, Sill = sillimanite, Sph = sphene, Wrk = wairakite, Zo = zoisite.

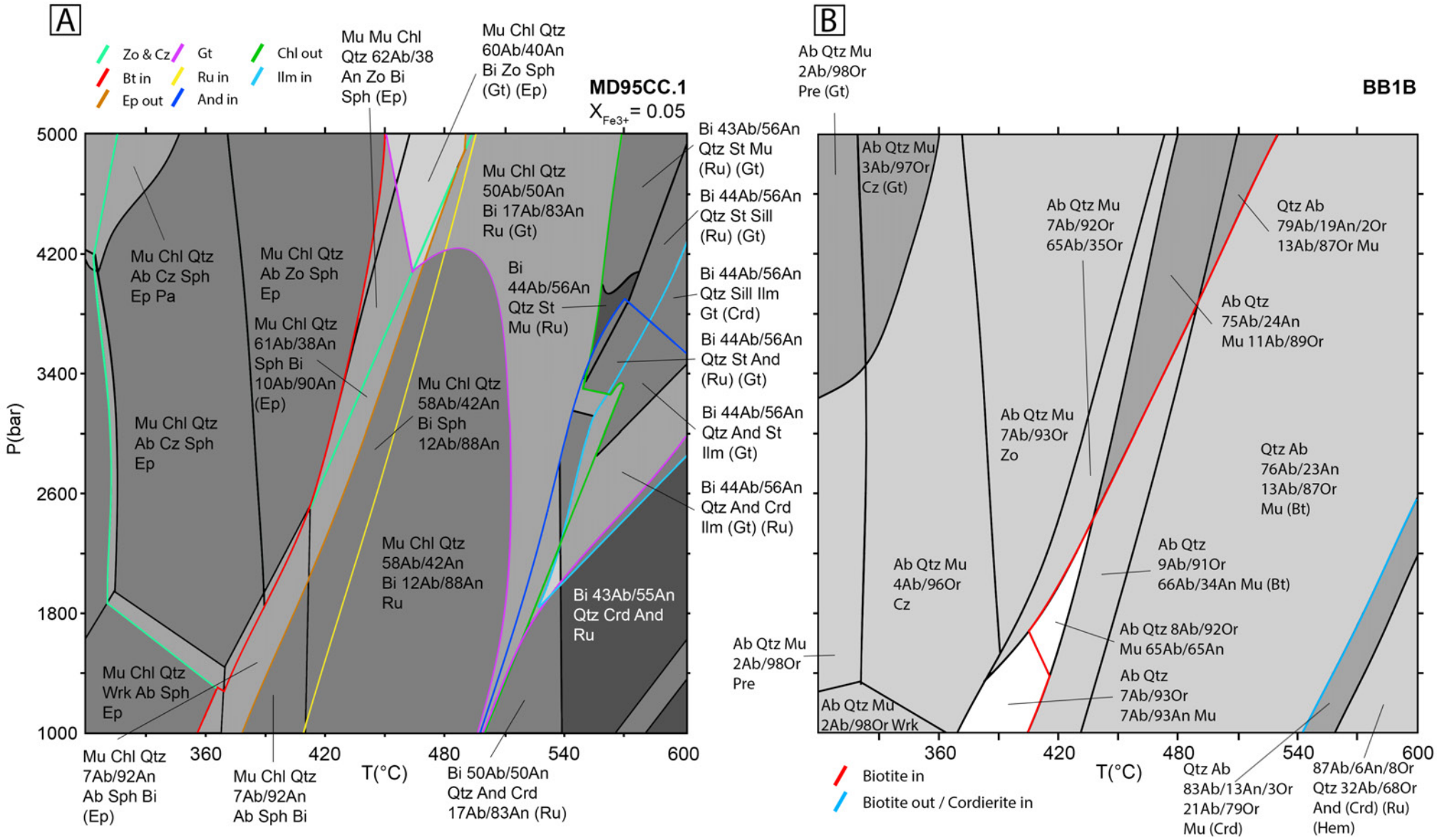

FIGURE 3.15: Pseudosections for thin section (**A**) MD95CC.1 and (**B**) BB1B. Chemical system, thermodynamic database and mineral abbreviations as in figure 3.14. MD95CC.1 is modeled with 5% of Fe as Fe^{3+} Phases with <0.2 wt% are not listed for BB1B.

Considering the calculated phase equilibria for thin section MD95CC.1, the most relevant changes in mineralogy with changing PT conditions are defined by the chlorite, biotite and epidote (and/or (clino)zoisite) reaction lines. As is apparent from the differences between figures 3.14 and 3.15, the partitioning of iron between its 2+ and 3+ oxidation state has a major influence on the predicted stability of biotite, the epidote-group minerals and the oxides. With the introduction of iron speciation as a compositional variable ilmenite stability was only predicted for $X_{Fe^{3+}}$ of $\leq$0.10. Due to the occurrence of ilmenite in thin section MD95CC.1 an intermediate value of $X_{Fe^{3+}}$ = 0.05 was chosen. Compared to the reference value of $X_{Fe^{3+}}$ = 0.25 (Forshaw and Pattison, 2021), at $X_{Fe^{3+}}$ = 0.05:

- the Fe-poor (clino)zoisite epidote group minerals appear in the lower-grade assemblages,
- ilmenite is stable at intermediate pressures above $\pm$ 540 °C and rutile stability shifts to above 400 °C,
- magnetite is not predicted in any field and oxides in general are much less abundant (close to 1 wt% compared to > 5 wt% in some fields),
- the biotite in reaction shifts towards lower temperatures by $\pm$ 60 °C to 360 °C at 1 kbar and 420 °C at 3 kbar,
- modal proportions of biotite increase with 50-100% below the chlorite out reaction
- the epidote out reaction shifts downwards with $\pm$ 50 °C to 380 °C at 1 kbar and 440 °C at 3 kbar.

For both $X_{Fe^{3+}}$ values the chlorite out reaction is modeled at $\pm$ 500 °C at 1 kbar and at 550 °C at 3 kbar, above which at low to intermediate pressures andalusite and/or cordierite and at higher pressures sillimanite are predicted. While garnet stability encompasses several fields its modal volume never exceeds 1%.

The modeled feldspar compositions are not significantly influenced by the Fe-partitioning. In the fields between the epidote and chlorite out reaction lines two distinct feldspars are predicted to occur: 1) a plagioclase feldspar ranging from 40-60 % albite, and 2) a less abundant plagioclase feldspar (80-90% anorthite). Suggested modal proportions of the Ca-rich plagioclase are $\pm$ 5% (volume) at high temperatures, decrease with temperature and approach 1% close to the epidote reaction line. Below this line its predicted stability disappears completely and the remaining plagioclase becomes more sodium rich before pure albite is predicted. Modal proportions of feldspar rapidly decrease with temperature below the epidote out line and have become a minor phase at the lower range of the plotted temperatures.

For thin section BB1B a two (or three) feldspar assemblage is predicted for all fields in the plotted PT range. Albite (or sodium rich plagioclase) is the dominant feldspar (in all fields approximately 50 wt%), with increasing sodium content as temperature decreases. Below the biotite- and cordierite out reaction line the orthoclase component in K-feldspar is consistently calculated between 87-98%. K-feldspar contents decrease from $\pm$ 15% at the 600 °C to $\pm$ 10% at 300 °C. The biotite in reaction is modeled between 390-420 °C at pressures below 2 kbar, increasing to 460 °C at 3kbar, however modal proportions are well below 1 wt%.

When limiting the chemical components to the KFMASH system the BRC compositions

of MD95CC.1 and C97-9 are practically identical as differences between these samples are mainly in Na and K content. AFM diagrams (appendix B) projected from muscovite predict the following assemblages in this system for thin section MD95CC.1 at 2 kbar:

Temperature	**Assemblage**
400 °C	Chlorite + chloritoid
425 °C	Chlorite + chloritoid ± andalusite
450 °C	Chlorite + chloritoid + andalusite
475-500 °C	Chlorite + andalusite ± chloritoid
>525 °C	Andalusite + Biotite

And for thin section CC97-9 at 4 kbar:

Temperature	**Assemblage**
450 °C	Chlorite + chloritoid
475 °C	Chlorite + chloritoid ± kyanite
500 °C	Chlorite + chloritoid + staurolite
525 °C	Chlorite + staurolite
550 °C	Staurolite + biotite ± chlorite
575 °C	Staurolite + Biotite
>600 °C	Sillimanite + Biotite

3.5 EBSD

EBSD data was acquired on a strongly folded quartz layer in thin section MD95CC.3. The inverse pole figure (IPF) maps show distinct oblique banding: alternation between ±0.5 cm bands with c-axes dominantly perpendicular to the kinematic XZ plane (X: parallel to lineation, Y: parallel to foliation and normal to lineation, Z: normal to foliation), and bands of similar size with a more oblique orientation of quartz c-axes (IPF Y map and pole figures in figure 3.16).

Pole figures constructed from the entire quartz orientation dataset show a central and slightly oblique cluster for the c-axes and six evenly spaced maxima for the a-axes. The c-axes pattern is consistent with a combination of prismatic and rhomb slip in the <a> direction (figure 3.17). Patterns for the bands with c-axes predominantly perpendicular to plane of view show a well defined central cluster of c-axes that is only slightly oblique (figure 3.16C), indicative of prism <a> slip. The a-axes form six well defined clusters, with the two most prominent ones parallel to the fabric attractor. Pole figures constructed from bands with more oblique c-axis orientations with respect to the thin section plane show a oblique c-axes pattern that is defined by a combination of (mostly) rhomb <a> slip and (some) prism <a> slip (figure 3.16D). Here a-axes do not form a clear pattern, but best defined maxima are parallel to the fabric attractor plane.

Noteworthy is that while the CPO patterns are consistent with a dextral sense of shear the fold geometry indicates a sinistral shear sense.

Grain sizes form a single uniform distribution with no difference between the different oblique bands. The mean area weighted equivalent circle diameter is 76 µm, with a standard deviation of 25 µm. The distribution is slightly skewed towards larger grain sizes, suggesting grain sizes have been reduced (appendix C). These grain sizes are consistent with dynamic recrystallization by means of SGR as follows from the statistical analysis of Stipp et al. (2010) who have correlated recrystallized grain diameters to quartz microstructures based on a large dataset of natural samples.

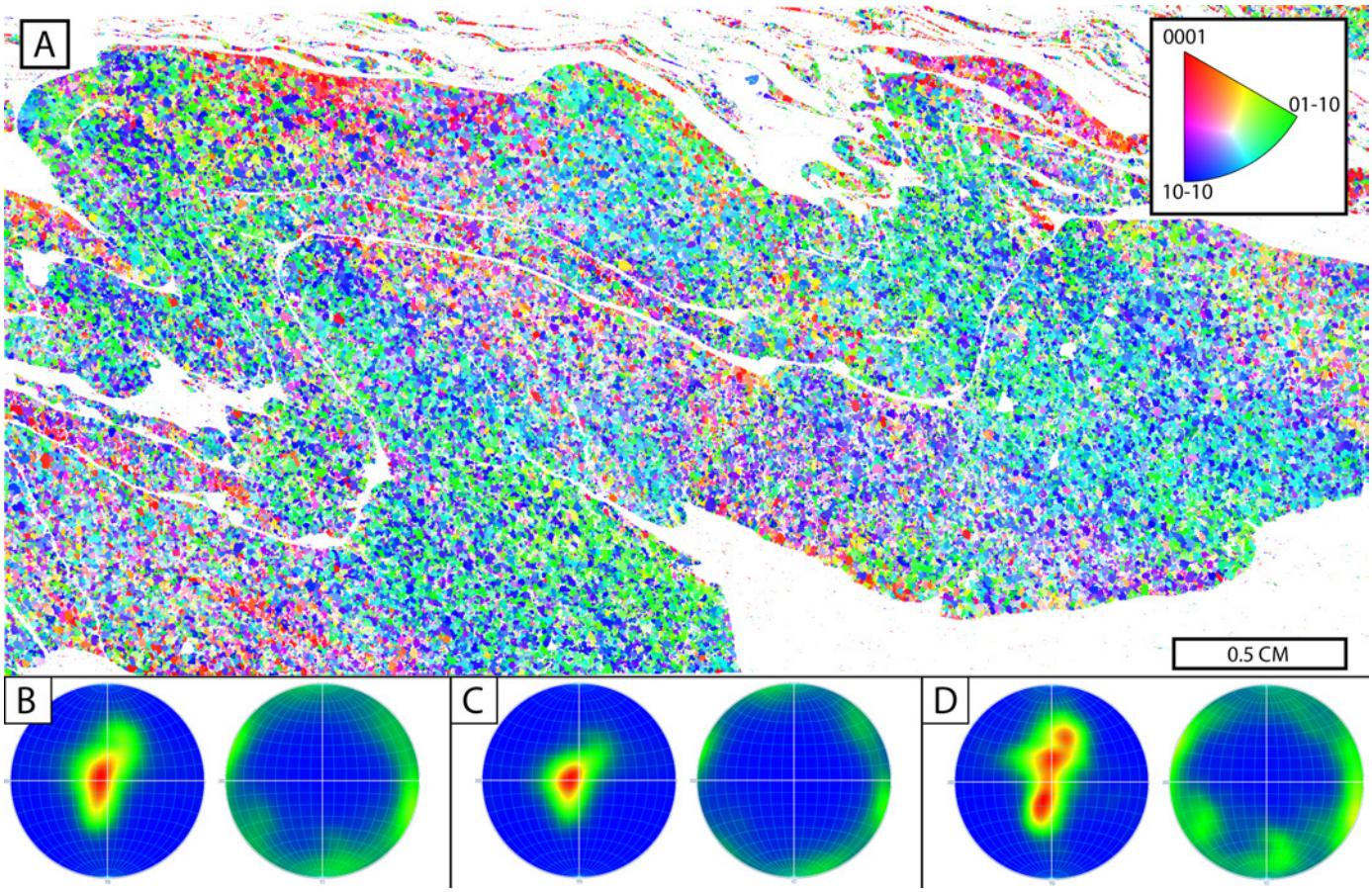

FIGURE 3.16: EBSD data on thin section MD95CC.3. (**A**) IPF map showing the orientation of quartz grains with respect to the Y direction. X: horizontal, Y: vertical: Z into the map. Color coding according to inset. (**B**) Pole density figures showing the CPO of quartz c-axes (left) and a-axes (right) of the entire dataset. (**C**) Same as (B) for the dominant blue and green colored bands (C axes perpendicular to Y). (**D**) Same as (B) for the band with c-axes more oblique to Y.

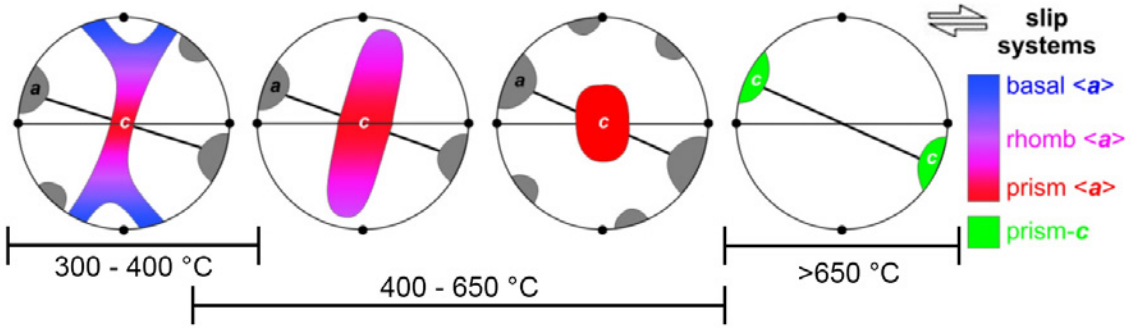

FIGURE 3.17: Schematic pole figures showing CPO development of quartz a-axes (gray maxima) and c-axes (colored maxima) under non-coaxial dextral shearing. Color coding corresponds to different slip systems and the oblique line resembles the flow plane. Figure modified from Parsons et al. (2016), after Passchier and Trouw (2005). Indicated temperature ranges (after Mainprice et al., 1986; Schmid and Casey, 1986; Stipp et al., 2002) are approximate.

3.6 Ti-in-Quartz

For thin sections MD95CC.1 and -.3 CL maps were made which show variation in CL intensity 1) within individual quartz grains as banding, 2) between grains and 3) between domains in the individual thin section. The banding within individual grains has a wavy nature, varies in thickness, is often similarly orientated in neighboring grains and sometimes crosses grain boundaries. These features appear to have a structural nature, possibly deformation related (deformation lamellae) as structures of a similar nature are observed in optical microscopy. In the 500-600 nm and to a lesser extent in the 600-700 nm range this banding is also observed suggesting it is not (exclusively) related to Ti content of quartz.

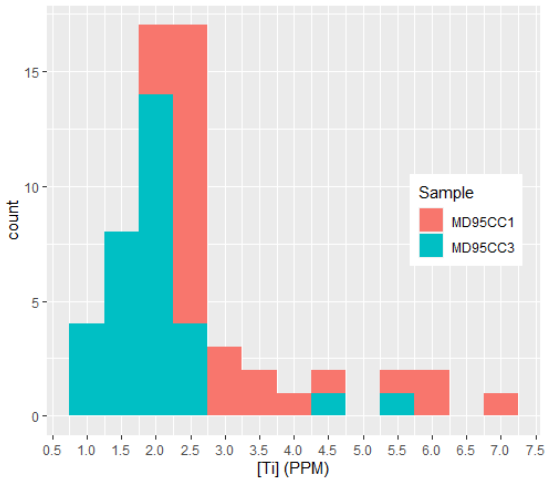

FIGURE 3.18: Frequency distribution of measured Ti concentrations. Eight [Ti] > 7.5 ppm spots are not displayed.

In thin section MD95CC.1 a total of 35 spots distributed over four transects were measured, and in thin section MD95CC.3 three transects composed of in total 35 spots. For an overview the transect locations within the thin sections refer to appendix E. After filtering out measurement cycles with anomalously high Ti (sometimes > 100 ppm), the measured Ti concentrations generally range from 1.2 to 10 ppm with 1-sigma uncertainties in the range of 0.02-0.04 ppm. Occasionally concentrations of 10-40 ppm are measured, likely caused by Ti-rich inclusions. The four transects in MD95CC.1 were set out in three different domains based on CL characteristics:

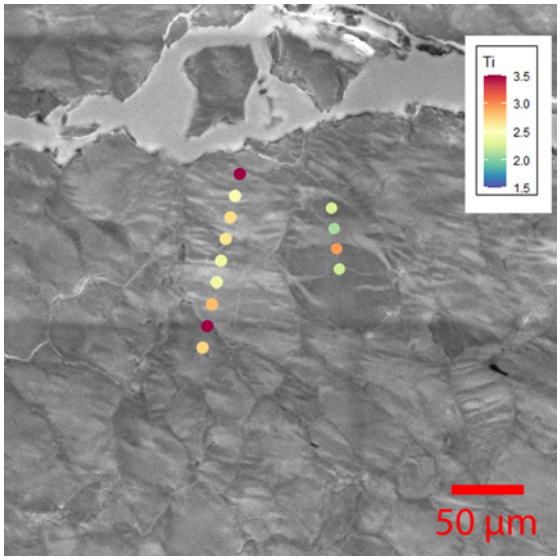

FIGURE 3.19: CL map with measured Ti concentrations in transects 1 & 2 in sample MD95CC.1. Dark red for [Ti] $\geq$ 3.5 ppm.

1. One transect of 11 spots (5 µm) was plotted crossing two grains grains showing banding with 5 µm spacing between the spots to capture within-grain variation of Ti content. The second transect with similar spacing was set out in the neighboring grain with a slightly weaker CL signal for comparison (figure 3.19).
2. A transect of 9 spots covering 500 µm and capturing 9 grains in a relatively bright region. This transect was measured with a spot size of 10 µm resulting in five measurements with more than 10 ppm Ti.
3. A transect of 11 spots (5 µm) spanning 300 µm containing 6 grains in a slightly darker domain.

The same approach was applied to thin section MD95CC.3, now with all spots 5 µm in diameter:

1. One transect of 12 spots was set out perpendicular to a $\pm$ 250 µm in diameter sheared quartz limb crossing 6 grains.
2. Six spots parallel to a thin (30 µm diameter) quartz band in a mica rich domain.
3. A transect of 16 spots covering 900 µm perpendicular to a weak CL intensity band following the fold geometry in the interior of a 0.5 cm thick quartz band.

Frequency distributions of Ti concentrations for the measured spots in samples MD95CC.1 & -.3 show concentrations are distributed normally around values of 2.25 and 2.0 ppm respectively, with the tail of the distributions close to 4 ppm (figure 3.18). To avoid high Ti spots offsetting mean values measurements with [Ti] > 4 ppm are excluded in the calculations, resulting in mean concentrations in MD95CC.1 and -.3 of approximately 2.60 and 1.90 ppm, respectively (table 3.7). For all profiles with measured Ti values refer to appendix E.

TABLE 3.7: Mean Ti concentrations.

	Domain	[Ti][1]	SD[1, 2]	N
MD95CC.1	1	2.52	0.26	11
	2	2.58	0.12	3
	3	2.66	0.60	7
	All	2.58	0.41	21
MD95CC.3	1	1.89	0.42	9
	2	1.92	0.32	6
	3	1.88	0.49	15
	All	1.89	0.45	30

[1] In ppm.
[2] SD - Standard deviation.

Ti concentrations vary within a single grain by $\pm$0.4 ppm. Based on these data a correlation between CL intensity and within-grain CL banding cannot be confirmed or ruled out. There is also no clear correlation between the minor variations in CL intensity and Ti concentrations for individual grains with different CL domains. An exception is the darker band in transect 3 in MD95CC.3 where Ti concentrations gradually decrease from $\pm$2.5 ppm outside this band to $\pm$1.2 ppm in the center of the band before gradually increasing to > 2 ppm again.

As a reference two transects were measured in sample FR3, a high-grade quartzite. While this sample is low in Ti-bearing phases the transect set out in the interior of a grain yielded a mean [Ti] of 7.22$\pm$1.06 ppm, and close to a crack values of 2.82$\pm$0.68 ppm were obtained (appendix E, figure E.9).

4 Discussion

4.1 SEM-AM results and workflow

Classification of phases in samples with large grains and consistent mineral chemistry (e.g. CC97-9) is rather straightforward, however in fine-grained samples that contain multiple phases or many impurities (e.g. MD95CC.1) there is a balance between 'classifying most pixels' and 'correctly classifying pixels'. The proportion of pixels that do not match any of the criteria listed in the final mineral recipes ranges from 1.9% for thin section CC97-9 to 9.9% for thin section MD95CC.1 (table 3.4). These numbers will be a slight overestimate of the actual unclassified phases due to the presence of cracks and voids in the thin section; especially MD95CC.1 contains several large voids.

The unclassified pixels are not evenly distributed across all phases: minerals with easy to constrain and well defined compositions that do not overlap with other phases (such as: quartz, tourmaline, apatite, monazite, zircon) contain very few unclassified pixels. In thin section MD95CC.1 most of these unclassified pixels ($\pm$ 80%) are located in fine-grained muscovite- and/or biotite rich domains, roughly evenly distributed between these phases. Within these fine-grained domains it is difficult to estimate how much biotite and muscovite is actually under-reported, and how much of the unclassified pixels can be attributed to the numerous sub step size inclusions. Larger biotite and muscovite grains contain few unclassified pixels. There are numerous reasons as for why an individual pixel can remain unclassified: anomalously high concentrations of certain minor elements (e.g. spike in Fe in a pixel surrounded by muscovite), anomalously low concentrations of major elements (e.g. no Al measured in a pixel surrounded by biotite) or values in between realistic compositions of biotite and muscovite. In the sheared pegmatites, the vast majority of the unclassified pixels are in albite that contains many impurities, cracks and alterations, or in fine-grained polyphase bands where one pixel often covers more than one mineral. Using the Python script to calculate BRC the effect of unlassified pixels on the final BRC will be minimized by considering unclassified pixels as a phase with sample-average specific gravity.

When comparing the final SEM-AM false color maps to the optical thin section scans obvious misclassified pixels are rare, and at grain sizes that allow details to be resolved with optical microscopy ($\pm$ 15-20 µm) in practice all pixels that are actually classified are done so correctly. At smaller scales it is difficult to compare SEM-AM maps at pixel level to BSE images due to the effects introduced by slight optical distortion, however it appears that if phases are classified they are classified correctly, even at grain boundaries, until grain sizes approach the SEM-AM step size. This is the case in thin section BB1B, which was mapped using a step size of 8 µm, where in a very fine-grained band not all phases are resolved correctly (lowermost band in figure 3.10A). Within this band SEM-AM results report the following area percentages: 43% Qtz, 22% Or, 15% Ms, 8% Ab, <1% Ap, 12% Unclassified. BSE images of this band (e.g. figure 3.8E) do not show the presence of any albite. Area percentages based on BSE images using gray value separation are: 50% Or, 31% Qtz, 10% Ms, 5% Fe-oxide, 4% porosity.

The reported albite is likely a result of the mineral recipe implementation specific for the sheared pegmatites: for every pixel relative elemental abundances are first compared

against the criteria for orthoclase, and when these do not match they are compared to those for albite. Examining individual pixels classified as albite reveals this is mainly due to too low potassium concentrations in order to be classified as orthoclase. Reported sodium is negligible for these pixels, however in practice it was necessary to set the lower bound for sodium in albite to 0 to avoid many unclassified pixels in albite. While reported abundances of other phases in this band deviate from the BSE images the discrepancies are limited, especially considering grain sizes for different minerals range from close to, to well below the used step size. This issue of pixels incorrectly classified as albite does not manifest itself outside of this single band in sample BB1B.

The SEM-AM Zeiss Mineralogic software only uses the elements that are specified in the recipe to calculate the mineral chemistry and disregards the other elements being measured. So in case SEM-AM results are to be used for BRC calculation without EDS spot measurements it is worthwhile to include (minor) elements that are not necessarily needed for mineral classification purposes as long as this does not negatively impact the classification. Even when not all elements in a phase are included in the recipe it can still be useful to compare mineral chemistry to EDS spot measurements as the discrepancies between calculated AM-SEM and measured EDS mineral chemistry are a good measure for quality of the classification for that phase.

Misclassification of pixels will affect the quality of the BRC calculation based on SEM-AM data in two ways:

1. It will influence the modal mineralogy, and
2. It offsets the mineral chemistry.

In that light it is better to pursue correct classification of all pixels at the cost of unclassified pixels rather than trying to achieve the classification of all pixels at the cost of misclassified pixels: while it is still possible to incorporate unclassified pixels in BRC calculation using the Python script, the amount of misclassified pixels can only be estimated and the effect on mineral chemistry cannot be corrected for.

A comparison between SEM-AM calculated and manual EDS spot measured mineral chemistry shows that discrepancies are generally relatively small, except for Si which is consistently being (significantly) over-represented in the SEM-AM data (table 4.1). These results indicate final mineral classifications are for the most part correct, and SEM-AM reported modal mineralogy will be close to the 'true' value. Not considering the Si discrepancies and minor elements, the largest deviations between manual EDS and SEM-AM mineral chemistry are in biotite, muscovite and tourmaline in the deformed schists and in orthoclase and muscovite in the sheared pegmatites. Regarding the deformed schists: compared to EDS measurements the calculated SEM-AM mineral chemistry in muscovite is low in Al and Fe and high in K, and for biotite low in Al and K. This makes it unlikely that missclassification between biotite and muscovite is the cause of the observed differences, also as muscovite is the most K-rich phase in these schists. A similar phenomenon is observed in muscovite and orthoclase in the pegmatite mylonites: for both minerals K is over-reported and Al is under-reported. In tourmaline Mg is significantly under-reported and while tourmaline is predominantly surrounded by a Mg-poor phase (muscovite), separation between the two minerals is easy to verify with SEM-AM false color maps overlays on optical images and is excellent. So while the missclassification of pixels may contribute in some part to the discussed differences, the EDS signal processing (e.g. deconvolution of energy spectra) in the Zeiss Mineralogic software likely plays a major role.

The best approach is to constrain mineral chemistry using EDS or WDS spot measurements (for the most abundant minerals, and ideally for all), and use these in conjunction

TABLE 4.1: SEM-AM calculated mineral chemistry (AM) compared to measured EDS mineral chemistry (EDS) for selected minerals in samples MD95CC.1 and BB1B. Listed differences (Diff) are absolute values.

MD95CC.1	Plagioclase			Biotite			Chlorite			Muscovite			Tourmaline		
	AM	EDS	Diff	AM	EDS	Diff	AM	EDS	Diff	AM	EDS	Diff	AM	EDS	Diff
SiO_2	59,74	57,89	1,84	38,15	35,06	3,09	30,28	26,89	3,39	52,20	47,77	4,43	48,32	40,12	8,20
Al_2O_3	25,78	26,89	1,11	19,86	18,65	1,22	23,52	23,83	0,30	34,27	37,32	3,06	39,99	39,80	0,19
Fe_2O_3	0,06	0,27	0,21	22,82	24,08	1,26	30,88	30,92	0,05	0,70	2,07	1,37	6,29	7,93	1,64
MgO	0,00	0,22	0,22	10,36	11,58	1,22	14,96	17,36	2,40	0,03	0,86	0,82	4,36	8,15	3,79
CaO	7,55	7,10	0,44	0,00	0,01	0,01	0,07	0,04	0,04	0,00	0,01	0,01	0,22	1,10	0,89
Na_2O	6,82	7,37	0,54	0,10	0,09	0,00	0,10	0,11	0,00	0,34	0,87	0,53	0,76	2,05	1,29
K_2O	0,05	0,19	0,14	8,66	8,72	0,06	0,12	0,42	0,31	12,41	10,30	2,11	0,00	0,02	0,02
TiO_2	0,00	0,03	0,03	0,02	1,64	1,62	0,02	0,11	0,09	0,00	0,75	0,75	0,06	0,79	0,73
MnO	0,01	0,01	0,00	0,04	0,16	0,12	0,05	0,32	0,26	0,05	0,04	0,02	0,00	0,04	0,04

BB1B	Albite			Orthoclase			Muscovite			Quartz		
	AM	EDS	Diff	AM	EDS	Diff	AM	EDS	Diff	AM	EDS	Diff
SiO_2	69,29	64,23	5,06	65,83	63,93	1,90	54,55	48,26	6,30	98,43	97,46	0,97
Al_2O_3	21,73	22,08	0,35	17,56	19,62	2,06	32,11	36,70	4,59	1,15	1,27	0,12
Fe_2O_3	0,11	0,40	0,29	0,13	0,31	0,18	0,36	1,88	1,51	0,12	0,29	0,16
MgO	0,02	0,37	0,35	0,00	0,50	0,50	0,02	1,57	1,56	0,02	0,36	0,35
CaO	0,09	1,28	1,18	0,00	0,15	0,15	0,00	0,14	0,14	0,00	0,06	0,06
Na_2O	8,75	11,25	2,50	0,21	0,84	0,63	0,15	0,51	0,36	0,07	0,23	0,16
K_2O	0,01	0,17	0,16	16,27	14,26	2,01	12,64	10,44	2,20	0,00	0,06	0,06
TiO_2	0,00	0,06	0,06	0,00	0,21	0,21	0,02	0,32	0,31	0,02	0,10	0,08
MnO	0,00	0,14	0,14	0,00	0,15	0,15	0,14	0,15	0,00	0,11	0,13	0,02

with SEM-AM modal mineralogy for BRC calculation. When EDS or WDS data is available this can also be used to help constrain the compositional criteria in the mineral recipe, either beforehand or afterwards when running retrospective analyses. When mineral compositions are consistent the quality of the SEM-AM classification can then be verified by comparing SEM-AM calculated mineral chemistry with EDS or WDS measured mineral chemistry.

As discussed earlier, the final SEM-AM mineral chemistry results presented here are in agreement with EDS spot measurements for most elements in most minerals indicating classification is mostly correct. The accuracy of EDS measurements compared to WDS measurements is generally good for major and minor elements, but for trace element analysis WDS data is superior (section 3.2.2). The overall quality of the SEM-AM results are confirmed by the XRF results that match the calculated BRC fairly well considering only selected parts of the thin sections have been SEM-AM mapped.

4.2 Constraining metamorphic conditions of the Cap de Creus samples

The reference sample (CC97-9) was obtained in the transition from the sillimanite-muscovite zone to the sillimanite K-feldspare zone and is characterized by a mineral assemblage consisting of Qtz + Bt + Ms + Pl + Sill (section 3.1.1). This assemblage, including the measured feldspar composition, is modeled in a single field at 650± 30 °C at pressures > 3.9 kbar and thus provides a well-constrained temperature estimate. This estimate is in line with research by Reche et al. (1996) that has suggested peak metamorphic conditions for the sillimanite-zone at 670 °C and 4.7 kbar based on garnet geothermobarometry, thereby demonstrating the potential of thermodynamic modeling based on SEM-AM obtained bulk rock composition. Limiting the chemical components to the KFMASH system

a similar assemblage is predicted at >600 °C and 4 kbar, but lacking plagioclase as this system contains no Ca and Na.

The consequence of using the KFMASH system is that Na- and Ca-bearing phases cannot be modeled, and therefor the effects of Al-rich phases containing Na and/or Ca (specific to these samples: plagioclase and epidote) on aluminum silicates stability are not accounted for. Also the effects of the minor elements Ti and Mn on mineral stability are ignored. So while adequately showing Mg and Fe partitioning relationships, the use of the KFMASH chemical system is limited when modeling natural metapelites as is evident from the discrepancies between the AFM diagagrams and both the observed mineralogy and calculated mineral equilibria for the lower-grade samples using the more complex MnNCKFMASHT system.

The complexity of sample MD95CC makes it less straightforward to constrain PT conditions using calculated mineral stabilities for a single bulk rock composition. Due to the combination of compositional heterogeneity, lower temperatures, and deformation and fluid induced- or enhanced reactions overprinting earlier mineral assemblages it is unlikely a bulk rock equilibrium has been achieved. This is evident from the many phases that are observed to be involved in reactions. An additional complication is the unknown partitioning of Fe between the 2+ and 3+ oxidation states. Nonetheless, based on the results of thermodynamic modeling the behavior of mainly (clino)zoisite, biotite and chlorite can provide insights with regard to deformation conditions. These three minerals are present in varying degrees in the fine-grained matrix as is apparent from the BSE images, with (clino)zoisite often having an unstable appearance. The upper temperature bound is defined by the chlorite out reaction (500 °C at 1 kbar, 560 °C at 4 kbar). Abundant precipitation of biotite in shear bands and in strain shadows overprinting plagioclase combined with the occurrence of (clino)zoisite indicates conditions are close to the epidote (or zoisite) and biotite reaction lines. The lower bound is then set by the biotite reaction line, just below and more or less parallel to the epidote reaction line, both of which are strongly dependent on $X_{Fe^{3+}}$.

While the modeled system with a reference $X_{Fe^{3+}}$ of 0.25 for metapelites (Forshaw and Pattison, 2021) suggests biotite stability above 420 °C is in line with traditional estimates, the observed mineral assemblage is more consistent with modeling results obtained using the significantly lower value of $X_{Fe^{3+}}$ = 0.05 as in this case:

- no magnetite is predicted, ilmenite is the main oxide at temperatures > 500 °C and intermediate pressures. and oxide phases in general are much less abundant,
- (clino)zoisite stability is calculated at lower end of the modeled PT range.

TABLE 4.2: PT estimates from thermodynamic modeling for thin section MD95CC.1.

$X_{Fe^{3+}}$	P	Bt in	Ep out
0.05	2.5 kbar[1]	410 °C	420 °C
	3.5 kbar[2]	430 °C	450 °C
0.25	2.5 kbar[1]	430 °C	450 °C
	3.5 kbar[2]	460 °C	480 °C

[1] Lower bound after garnet stability.
[2] Upper bound after andalusite stability.

The observed mineral assemblage is interpreted to represent retrograde metamorphism as is apparent from the relict andalusite crystals, and based on the andalusite stability field an upper pressure of ± 3.5 kbar can be estimated. Garnets have not been observed in the studied samples, but Fußeis (2007) reported µm-scale synkinematic garnets in an ultramylonite of similar mineralogy belonging to the same shear zone suggesting a lower pressure constraint of ± 2.5 kbar is reasonable based on predicted garnet stability. Corresponding temperature estimates constrained by the biotite in and epidote out reaction lines range from 410-450 °C and 430-480 °C for $X_{Fe^{3+}}$ =

0.05 and $X_{Fe^{3+}}$ = 0.25, respectively (table 4.2).

Retrograde metamorphism is consistent with both predicted and observed plagioclase compositions. The two main Ca bearing phases are plagioclase and epidote, with apatite as minor Ca host that does not appear to be significantly involved in reactions. While plagioclase core compositions (andesine) in sample MD95CC match with those predicted well above the epidote and biotite reaction lines, the observed plagioclase rims tend towards the more Na-rich oligoclase composition (figures 3.5 & 3.6) that is consistent with compositions found close to the the epidote and (clino)zoisite stability fields. Many studies have shown feldspars to re-equilibrate when in contact with hydrothermal fluids, both in natural rocks (Plümper and Putnis, 2009) and in laboratory experiments (Niedermeier et al., 2009; Putnis and Putnis, 2007). The observed sharp interface in both BSE contrast and EDS element maps is characteristic of the interface-coupled dissolution–reprecipitation mechanism proposed by the aforementioned authors. As plagioclase re-equilibrates to a more Na rich composition Ca is released to the fluid allowing (clino)zoisite to grow.

Reaction lines on which previous discussion is based may shift as a function of the available elements that define a 'local' bulk composition, either due to elements effectively being locked up in larger grains or as a result of compositional differences, and can thus vary throughout the sample. It is difficult to estimate the scale of local compositions, but growth of (clino)zoisite in domains poor in plagioclase evidences that element transport occurs on scales larger than individual grains.

Research by Stipp et al. (2002) and Passchier and Trouw (2005) has shown that the quartz dynamic recrystallization mechanism can be used as means of estimating deformation temperatures. Observed quartz microstructures and grainsizes in the MD95CC thin sections are consistent with the subgrain rotation (SGR) regime, corresponding to a temperature range of 420-490 °C (Stipp et al., 2002).

Associated with dynamic recrystallization mechanisms of quartz are the different slip systems that are active under different temperature regimes. As the (combinations of) activity on different slip systems result in characteristic CPO patterns these can be used to provide information on deformation conditions: at 300-400 °C slip on the basal plane in the <a> directions is dominant, from 400-650 °C first rhomb <a> and then prism <a> slip become more active and at > 650 °C prism <c> slip is dominant (Mainprice et al., 1986; Schmid and Casey, 1986; Stipp et al., 2002). These ranges are broad estimates as the activity of slip systems is also a function of strain rate, strain geometry and water content. CPO patterns based on EBSD orientation data from sample MD95CC.3 are indicative of mixed rhomb and prism <a> slip, corresponding to a temperature range of $\pm$ 400-500 °C. When considering bands with distinct CPO's seperately the bands with c-axes consistently aligned perpendicular to the thin section show patterns with dominant <a> slip characterized by a single c-axis Y-maximum corresponding to the higher end of the 400-500 °C range (Stipp et al., 2002).

The pseudosections calculated for the sheared pegmatites do not provide many insights in deformation conditions as 1) few major changes in mineralogy are predicted and 2) due to the large number of porphyroclasts the bulk mineralogy does not come close to representing an equilibrium assemblage. Some qualitative comments can still be made:

The extensive precipitation of fine-grained muscovite and the commonly observed partial sericitization of clasts is consistent with the predicted increasing muscovite content at lower temperatures (figure 3.15B). For all fields orthoclase is predicted, however modal

proportions decrease with temperature. The observation that albite is predominantly reacting to either muscovite or orthoclase suggest that in orthoclase-rich bands deformation temperatures were not far below 400 °C, as at this temperature muscovite is predicted to be much more abundant than orthoclase. In other bands however, albite is reacting to muscovite in the absence of orthoclase. For muscovite and orthoclase grow, K and H need to be transported on a larger scale than individual clasts so it is unlikely the differences between orthoclase and muscovite growth can be explained (solely) by differences in fluid transport. From this and the suite of different quartz microstructures it follows that in different bands different stages of deformation are preserved. The observed partial recrystallization of quartz in the BLG regime, with the transition from SGR to BLG postulated by Stipp et al. (2002) at 390-420 °C. Besides evidence for BLG dynamic recrystallization, extensive SGR recrystallization is observed and remnants of ribbon quartz are present. The latter are commonly associated with deformation at mid-greenschist to amphibolite facies conditions in the presence of fluids (Dunlap et al., 1997; Gleason and DeSisto, 2008). The observed fine grained sillimanite in a shear band in sample B1B is likely a relict of deformation under a higher metamorphic grade because 1) sillimanite stability is only predicted at temperatures > 600 °C and 2) in the other samples that show signs of deformation under greenschist conditions no sillimanite is observed.

In the pseudosection calculated for sample BB1B some fields (mainly above 420 °C) contain a three-feldspar assemblage (figure 3.15B), while the measured feldspar compositions for this sample show only two distinct compositions (figure 3.5). This can be explained as follows: with Perple_X you have 1) the used feldspar solid solution model based on which two distinct feldspar compositions are calculated, of which one tends towards the albite endmember, but 2) the used thermodynamic database also contains albite as a compound with a fixed composition. So as the composition of the "solid solution feldspar" approaches the "thermodynamic databasae albite" there is some overlap. Once the "solid solution feldspar" is predicted to be (almost) pure albite this phase disappears in the assemblages and only pure albite is predicted. So while the pseudosection shows three feldspars in practice it will be two, of which one is close to a pure albite composition.

4.3 Integration with Ti-in-Quartz

In order for Ti concentrations to reflect deformation conditions, re-equilibration with a Ti-bearing phase needs to have occurred. Work by Negrini et al. (2014) suggests that because Ti atoms act as defects within the quartz structure Ti concentrations are more easily reset during deformation under retrograde conditions when Ti is expelled from the lattice, than during deformation under prograde conditions when Ti is taken up into the lattice. When Ti is expelled from the lattice this can cause precipitation of Ti-bearing phases along grain boundaries, which can explain the SIMS cycles or spots with high Ti content (section 3.6). From the CL maps and measured SIMS profiles it is evident that Ti concentrations are fairly homogeneous. The exception is distinct low-Ti banding in thin section MD95CC.3, demonstrating re-equilibration in thick quartz bands was insufficient to homogenize Ti concentrations. This is likely a result of a limited fluid assisted exchange between quartz grains in the interior of bands with Ti bearing phases in the mica-rich domains. As the banding follows the overall fold geometry these low-Ti zones reflect compositional differences with regard to Ti concentration prior to folding. Unlike in other domains only one spot contained SIMS measurement cycles that had to be filtered out, suggesting these domains never reached Ti saturation. In an undeformed quartzite (sample FR3), that is poor in Ti-bearing phases, distinct differences were found between a grain close to a fracture

(± 2 ppm Ti) and grains further away from the fracture (± 8 ppm Ti), implying that re-equilibration has occurred in that sample. The consistent [Ti] in thinner (stretched) bands in thin section MD95CC.3 and thin section MD95CC.1 as a whole, can then be considered as signs of [Ti] resetting resulting in the precipitation of Ti-bearing phases along grain boundaries causing occasional Ti spikes in measurements.

Two experimentally derived expressions for relating temperature (or pressure, if temperature can be otherwise constrained) to Ti concentrations are available. The first by Thomas et al. (2010):

$$T(^{\circ}C) = \frac{a + cP}{b - R \cdot \ln X_{TiO_2}^{Qtz} + R \cdot \ln a_{TiO_2}} - 273.15 \tag{4.1}$$

where a (60952±3122), b (1.520±0.04) and c (1741±63) are empirically derived parameters related to changes in respectively enthalpy, entropy and volume, R is the gas constant, $X_{TiO_2}^{Qtz}$ is the mole fraction of TiO_2 in quartz, a_{TiO_2} is the Ti-activity in the considered system and P is pressure in kbar. Challenging the work from previous authers, Huang and Audétat (2012) derived the following relationship after their experiments:

$$\log \text{Ti(ppm)} = \frac{-0.27943 \cdot 10^4}{T} - 660.53 \cdot \frac{P^{0.35}}{T} + 5.6459 \tag{4.2}$$

with T in K and P in kbar. Unlike the calibration of Thomas et al. (2010), the expression of Huang and Audétat (2012) does not take into account variation in a_{TiO_2} and obtained temperatures will be a lower estimate. However, analogous to Hayden and Watson (2007) a_{TiO_2} can be incorporated in this expression by dividing the measured Ti concentration by a_{TiO_2}. At low and intermediate pressures both calibrations are not very sensitive to changes in pressure, so even when pressure can only be broadly constrained the influence on calculated temperatures will be limited.

In studies by Morgan et al. (2014) on contact metamorphism and Ashley et al. (2014) on Ti resetting during dynamic recrystallization it is argued that the calibration of Thomas et al. (2010) underestimates recrystallization temperatures. On the other hand both calibrations were applied by Ashley et al. (2013) on amphibolite facies metapelitic rocks and by Kidder et al. (2013) on greenschist facies quartz veins and quartzites and found the Thomas et al. (2010) calibration to match better with independent temperature constraints. In later experiments Thomas et al. (2015) showed that quartz with a different Ti content can re-equilibrate to concentrations predicted by their original calibration. Nonetheless there is no clear answer to why many studies found discrepancies between conditions calculated using the Thomas et al. (2010) calibration and independent constraints, but differences in the activity of titanium likely plays a major role.

Besides uncertainties regarding the degree of Ti re-equilibration another factor hampering the application of the Ti-in-Quartz geothermometer are uncertainties in Ti-activity (a_{TiO_2}). In rutile bearing systems a_{TiO_2} is generally taken as unity, otherwise a range from 0.6-0.8 is proposed for metapelites (Ghent and Stout, 1984). In rocks containing ilmenite similar activity values (0.8) are suggested by Menegon et al. (2011) and Spear et al. (2012), however several authors have argued that a_{TiO_2} may be much lower (0.2 or even lower) in dynamic systems (Cawood and Platt, 2020; Bestmann and Pennacchioni, 2015; Ashley et al., 2014; Grujic et al., 2011, e.g.). In addition modeling by Ashley and Law (2015) implicates that Ti activity can vary significantly based on bulk rock chemistry, mineral assemblage and P-T conditions.

Following the results of recent Ti activity modeling on greenschist metapelites, best estimates of a_{TiO_2} for the here discussed schists are in the range 0.3-0.6:

- Ashley and Law (2015) modeled the average pelitic bulk composition from Mahar et al. (1997) (for a comparison with the discussed samples refer to table 3.6) and their results suggest a rapidly declining a_{TiO_2} at temperatures <450 °C. At 3 kbar and 400 °C an a_{TiO_2} of 0.45 is calculated.
- In a recent study Cawood and Platt (2020) modeled activity values for a large number of metetapelitic samples of varying compositions deformed under greenschist conditions. Most activities were calculated to lie between 0.3 and 0.5.

When assuming Ti activity between 0.3-0.6 and pressure between 2.5-3.5 kbar the following temperature ranges are obtained for thin section MD95CC.1 based on a mean [Ti] of 2.58±0.41 ppm:

Calibration	**T-min**	**T-max**
Thomas et al. (2010)	365±9 °C	421±10 °C
Huang and Audétat (2012)	465±10 °C	537±12 °C

And for thin section MD95CC.3 with a mean [Ti] of 1.89±0.45 ppm:

Calibration	**T-min**	**T-max**
Thomas et al. (2010)	349±13 °C	403±15 °C
Huang and Audétat (2012)	446±16 °C	514±20 °C

In the above results a_{TiO_2} is incorporated in the calibration of Huang and Audétat (2012) as was outlined earlier. Obtained temperature ranges are for both samples in the order of 50 °C and 70 °C for the calibrations of Thomas et al. (2010) and Huang and Audétat (2012), respectively. In both calibrations uncertainties in a_{TiO_2} contribute most to this range: at a given a_{TiO_2} the pressure uncertainty results in a difference of ±17 °C and ±23 °C for the calibrations of respectively Thomas et al. (2010) and Huang and Audétat (2012), while the a_{TiO_2} range of 0.3-0.6 results in calculated temperature differences of 38-40 °C and 48-53 °C (depending on pressure) for the two calibrations. Figure 4.1 visualizes the effects of uncertainties in pressure and a_{TiO_2} for fixed Ti concentrations in the discussed samples. It is apparent from these results that the Huang and Audétat (2012) calibration yields temperatures 100-120 °C higher compared to the Thomas et al. (2010) calibration, analogous to the findings of the earlier cited studies.

The [Ti] differences between thin sections MD95CC.1 (2.58 ppm) and MD95CC.3 (1.89 ppm) translate to roughly a 20 °C lower temperature for the latter. This may reflect actual deformation temperatures, however both thin sections were cut from the same sample and are very similar in mineralogy. The low number of spots in thin section MD95CC.3 (2 versus 13, with the same number of spots per thin section) where cycles had to be filtered out due to high Ti concentrations and the distinct low-Ti domains suggest that as a result of original variation in Ti content quartz never achieved Ti saturation in this thin section.

Integrating the Ti-in-Quartz obtained temperatures with the thermodynamic modeling does not give unambiguously results: when $X_{Fe^{3+}} = 0.25$ is assumed, the area in the pseudosection under the results calculated using the calibration of Huang and Audétat (2012) matches best with the observed mineralogy (dark blue shaded area in figure 4.2A), whereas at $X_{Fe^{3+}} = 0.05$ the expression of Thomas et al. (2010) is more in line with the observed mineralogy (dark red shaded area in figure 4.2B).

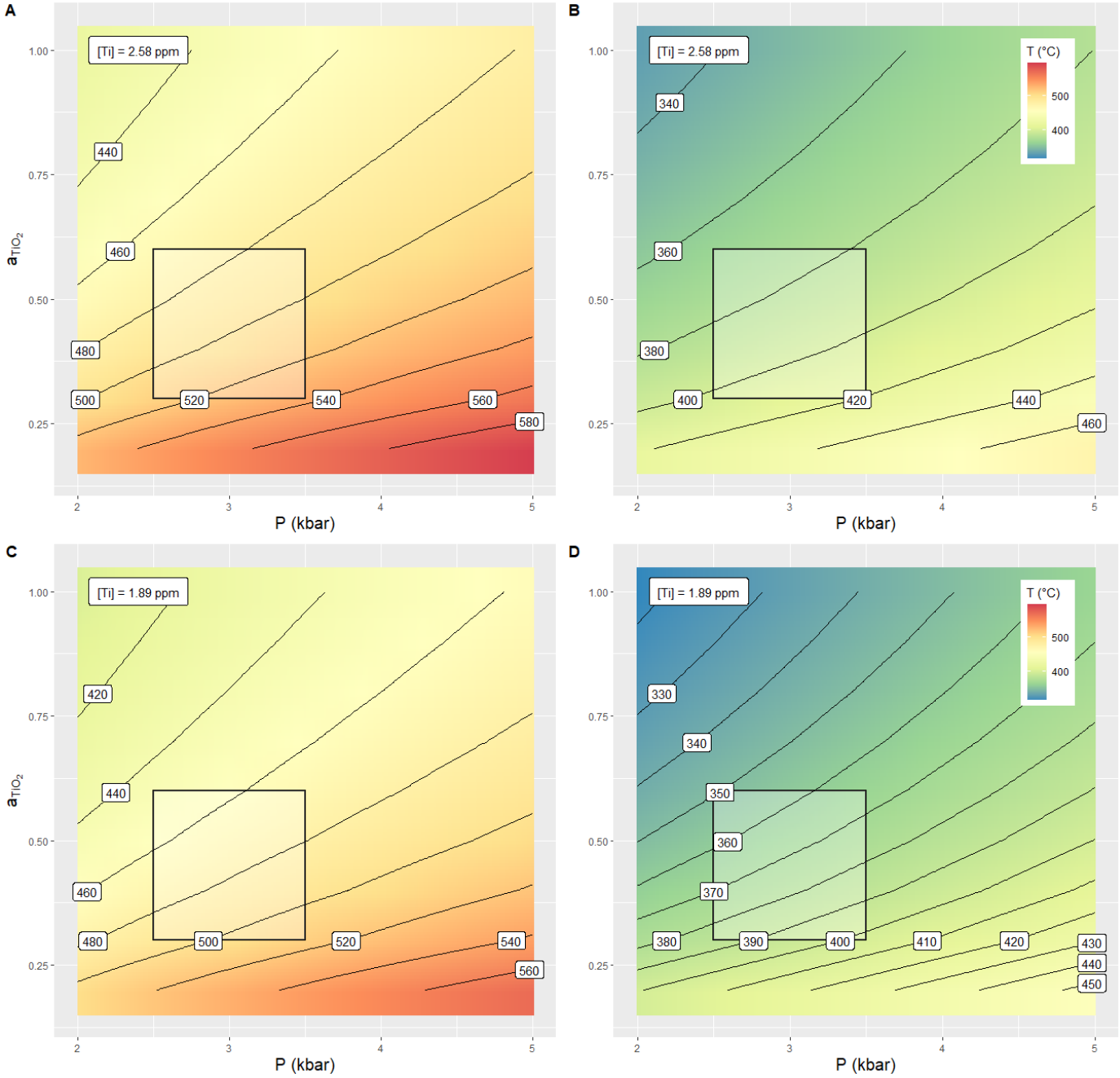

FIGURE 4.1: Calculated temperatures as function of pressure and a_{TiO_2} at fixed Ti concentrations. Figures (**A**) and (**C**) are computed using the calibration of Huang and Audétat (2012), figures (**B**) and (**D**) using the calibration of Thomas et al. (2010). Figures (**A**) and (**B**) are calculated with [Ti] = 2.58 as is measured in sample MD95CC.1, figures (**C**) and (**D**) with [Ti] = 1.89, corresponding to sample MD95CC.3. Insets mark the best estimates for a_{TiO_2} (0.3-0.6) and P (2.5-3.5 kbar). Color scale is the same for all figures.

As discussed earlier the predicted mineral assemblages at $X_{Fe^{3+}} = 0.05$ match best with the observations. In that case the calibration of Huang and Audétat (2012) yields minimum temperatures of ±60 °C above the epidote out reaction, whereas using the Thomas et al. (2010) calibration the upper range of predicted temperatures lies ±10 °C below the biotite in reaction at pressures between 2.5-3.5 kbar. With declining pressure the biotite reaction line and the Thomas et al. (2010) Ti-in-Quartz temperatures converge, overlapping

below 2.1 kbar. In the light of these results, subsequent experiments confirming the reproducibility of the Thomas et al., 2010 experiments and the questions regarding the validity of the experiments by Huang and Audétat (2012) that produced quartz with variable Ti content the Thomas et al. (2010) calibration is considered the most accurate. The discrepancy between the Ti-in-Quartz temperatures between 2.5-3.5 kbar suggest that Ti activity may be lower than 0.3, that the 2.5 kbar lower pressure estimate is too high, a combination of both, or that a final prograde evolution is preserved during which Ti concentrations did not re-equilibrate. While (clino)zoisite does appear to be involved in reactions there are no further arguments to support the possibility of a prograde deformation stage, and for the observed biotite growth the thermodynamic modeling offers an explanation that does not require a prograde deformation stage.

Summarizing the above: by comparing thermodynamic modeling to observed mineral assemblages, conditions close to the biotite and epidote (or (clino)zoisite) reaction lines were inferred. The Ti-in-Quartz results, taking into account the uncertainties inherent to the Ti-in-Quartz method (mainly a result of an unknown a_{TiO_2}), do not fundamentally challenge this estimate as the upper bound is within $\pm$10 °C of the biotite reaction line for pressures within the 2.5-3.5 kbar best estimate range. However, depending on the actual a_{TiO_2} the lower estimate of 2.5 kbar may be too high. The consequence of pressures below 2.5 kbar is that temperatures for which both biotite and epidote stability is predicted rapidly decline. Unfortunately no definite pressure constraints are available on the Cap de Creus greenschist overprinted rocks; neither from this work nor from literature. Although in several works of Druguet and Carreras (e.g. Druguet, 2001) a study of Bossiere et al. (1996) is mentioned who have supposedly estimated 3 kbar and 430 °C for the here studied shear zone from Fe and Mg partitioning between biotite and garnet. In either case, by combining the Ti-in-Quartz data with the results from thermodynamic modeling (assuming $X_{Fe^{3+}} = 0.05$) the following best estimates are obtained for the deformed schist (sample MD95CC):

P (kbar)	**T**
2.0	390-420 °C
2.5	400-430 °C
3.0	405-445 °C
3.5	410-450 °C

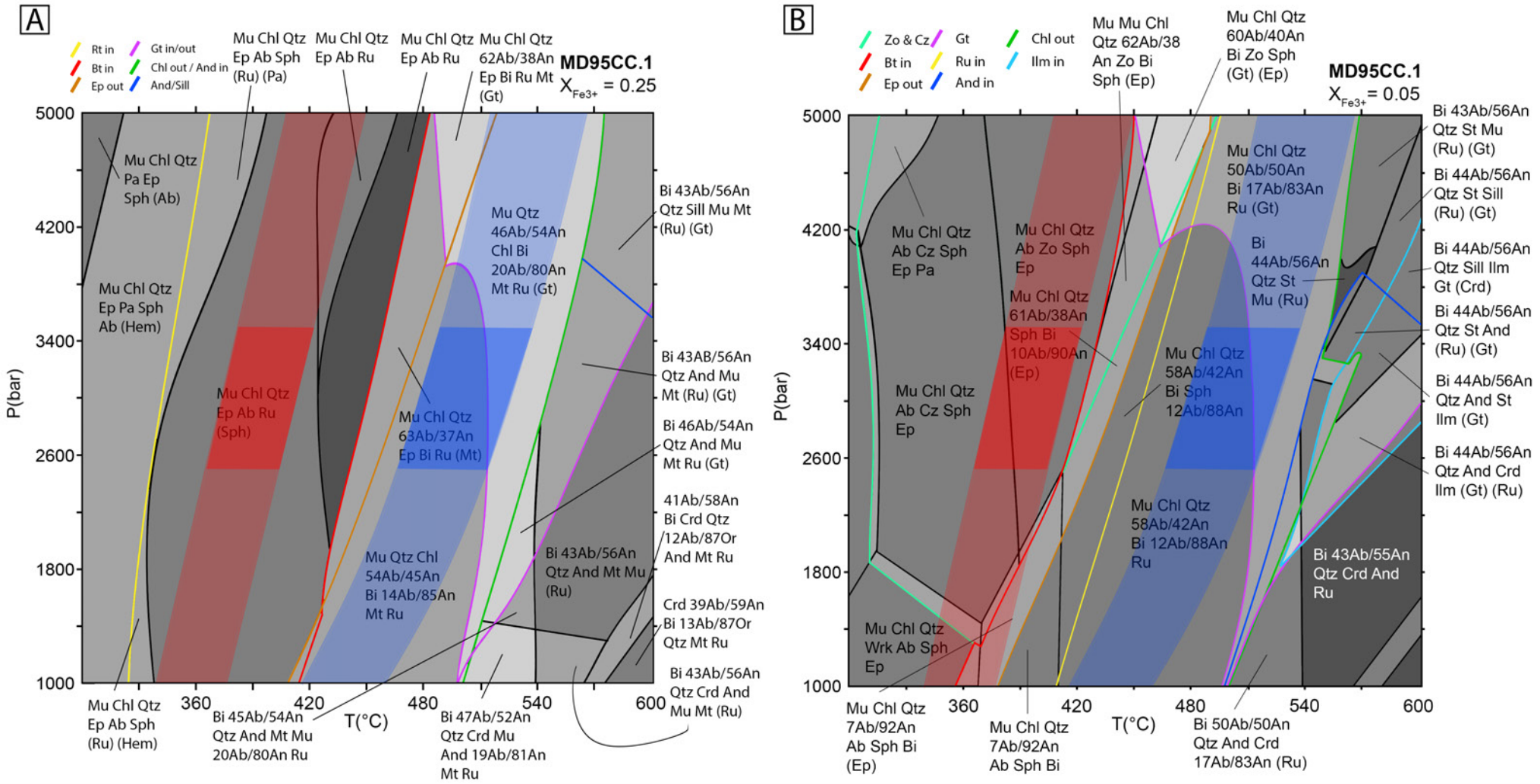

FIGURE 4.2: Integration of the Ti-in-Quartz results with the pseudosections for sample MD95CC.1 with $X_{Fe^{3+}}$ = 0.25 (left) and $X_{Fe^{3+}}$ = 0.05 (right). Outlined in red the temperature ranges calculated for a_{TiO_2} = 0.3-0.6 at given pressures from 1 to 5 kbar with [Ti] = 2.58 ppm using the Thomas et al. (2010) calibration, in blue using the Huang and Audétat (2012) calibration. Darker shading between 2.5-3.5 kbar Abbreviations as in figure 3.14.

4.4 Fluid transport

Comparison between oxides normalized against SiO_2 in the reference schist and the deformed schists indicates the bulk chemical composition may have changed as a result of element transport by hydrothermal fluids as the deformed schists show an enrichment in Ca and Na, a depletion in K and possibly an enrichment in Mg (section 3.3). From the precipitation of (clino)zoisite and feldspar alteration it is that clear fluid assisted element transport occurred, however quantifying the amount of fluid flux based on changes in mineralogy is troublesome. Using changes in bulk rock composition is not very helpful either as weight percentages by definition sum to 100 wt%. The amount of chlorite can be used as a rough indicator, but since chlorite is mainly observed in the muscovite-rich matrix as trails leaving tourmaline crystals, it is likely the reaction is controlled by the rate and extent of iron and/or magnesium that are released by tourmaline rather than the amount of fluid.

The use of concentration ratios cancels out the problem of normalizing to 100 wt% and assuming REE concentrations to be similar in both reference and deformed schist results in a calculated mass gain of $\pm$ 54%. According to Philpotts and Ague (2009) mass changes resulting from fluid transport in metamorphic rocks exceeding 35% are rare, but can in this case be explained by volume change associated with deformation as is in line with the observed extensional crenulations. Research shows that significant mass changes are not uncommon in shear zones: Streit and Cox (1998) have estimated (mostly silica) mass gains of 30-60% in a mylonitized granite and Tartèse et al. (2012) calculated mass changes ranging from -31% to +37% for several mylonitized granites. In a recent work by Stenvall et al. (2020) mass changes of -39% to +11% are proposed for retrograde shear zones overprinting migmatised gneisses.

The fluids that have deposited a lot of SiO_2 in sample MD95CC were likely Ca-bearing, as is interpreted from the Ca concentration ratios that are significantly elevated compared against presumably immobile elements (REE and most of the HFSE). An additional argument supporting Ca enrichment is the following: there is $\pm$6% of combined (clino)zoisite and epidote in thin section MD95CC.1, and $\pm$11% plagioclase (table 3.4). As clino(zoisite) contains approximately three times more Ca than the plagioclase in this sample, the release of Ca by the limited degree of feldspar alteration is insufficient to provide enough Ca for the abundant (clino)zoisite precipitation and epidote and (clino)zoisite growth around decaying monazite crystals. Other high temperature schists obtained from the sillimanite zone which are not discussed in this work show similar compositions as sample CC97-9 with regards to all major elements except K (appendix D), showing compositional differences do exist from place to place. To determine to what extent the changes in major elements Ca, Na, Mg and K are the result of element transport or reflect original compositional differences requires more geochemical data on undeformed samples. From a review by Tursi et al. (2018), discussing numerous works related to element mobility during shearing, it follows that Si, Ca, Mg and K are among the most mobile elements regardless of metamorphic conditions.

Since peak metamorphic temperatures corresponding to the upper amphibolite facies are estimated for the undeformed schists it is likely these rocks were dehydrated to a large extent prior to deformation, further implying a primarily external fluid source. In earlier research numerous models have been proposed to explain how surface derived fluids can penetrate the mid-crust to below the brittle-ductile transition, including: inverted stress gradients that allow dehydration derived fluids to flow up-temperature in a compressional setting (Clark et al., 2006), seismic pumping (McCaig, 1988) and topographically driven flow (Barker et al., 2000).

Rosenberg et al. (2020) related phosphate-filled fractures and phosphate seams along grain boundaries, similar to features observed in sample MD95CC and to a lesser extent in sample CC97-9, to the intrusion of tourmaline-bearing pegmatites and associated fluids. This implies both the deformed schist (MD95CC) and the reference schist (CC97-9) were influenced by pegmatite fluids and there is a possible relation between these fluids and the locally abundant tourmaline crystals in sample MD95CC.

4.5 Timing of deformation

It is generally assumed the localized greenschist overprinting of higher-grade metamorphic rocks occurred in the retrograde stages of the Variscan orogeny, in this region recognized as D3 deformation features (Carreras, 2001; Druguet, 2001; Druguet et al., 2014). The preservation of fine grained sillimanite in shear bands and the suite of quartz microstructures, both in the sheared pegmatites, indicate the activity of these structures over a wide range of temperatures consistent with retrograde deformation after peak metamorphic conditions. Based on the here presented results no contribution can be made to the ongoing debate regarding a possible Alpine reactivation (Vissers et al., 2017; Druguet et al., 2018; Vissers et al., 2018): the preserved mineralogy is consistent with both late-stage Variscan activity and with Alpine reactivation. The appearance of unstable (clino)zoisite and abundant biotite growth in shear bands may be a hint of (post-Variscan) prograde deformation, but without further supporting arguments this remains rather speculative.

4.6 Suggestions for future work

This work demonstrates how SEM-AM mapping can reveal features that are difficult to observe using traditional microscopy or BSE images when grainsizes are small, optical properties are similar, or Z-contrast is limited: the high contrast false color maps clearly visualize mineral associations, mineral reactions and structural features without having to resort to high magnification microscopy. In addition it is shown how SEM-AM data can be used to calculate bulk rock compositions that are in good agreement with traditional methods of obtaining bulk chemical data, provided mineral compositions are well-constrained and the SEM-AM step size is such that mineral phases can be adequately separated. Using the SEM-AM derived BRC as input for thermodynamic modeling results in predicted mineral assemblages that closely match the observed ones, especially for undeformed high-grade samples. The results for the samples deformed under greenschist conditions are associated with more uncertainties resulting from 1) these rocks achieving only partial equilibrium, and 2) uncertainties about the partitioning of iron between its 2+ and 3+ oxidation state. In order to fully assess the quality of this workflow it should be applied on a set of homogeneous and well-characterized samples for which reliable independent PT estimates are available.

While this approach has not been pursued in this work, it would be beneficial to be able to select parts of SEM-AM maps used to calculate *local* bulk chemical compositions that can be used as input for equilibrium modeling. This would allow to account for the effects of compositional heterogeneity on the scale of a thin section, and allow to compute local equilibria in fine-grained regions in overprinted rocks (provided high resolution maps are made). The Zeiss Mineralogic software suite does not offer this functionality, but integration with the here used Python processing script would be relatively straightforward. A simple but effective alternative would be using standard image analysis software to count the number of pixels by color in a selected region and use the area fractions as input for the processing script.

As the calculated pseudosections at $X_{Fe^{3+}}$ = 0.05 and at $X_{Fe^{3+}}$ = 0.25 demonstrate, the speciation of Fe exerts a major control on mineral stabilities and thus on predicted assemblages for given pressures and temperatures. Since the advent of modern analytical methods the partitioning of Fe between a 2+ and 3+ oxidation state is rarely measured since the most used techniques (XRF, EDS, WDS, LA-ICP-MS) only report total Fe. In the analysis of metamorphic rocks it is generally assumed all iron is ferrous (Fe^{2+}), however several studies have confirmed a minor concentration of ferric iron (Fe^{3+}) to significantly influence mineral equilibria (e.g. White et al., 2000; Diener and Powell, 2010; Boger et al., 2012): the fraction of ferric iron reduces the amount of ferrous iron that is available for silicate minerals, resulting in a) rocks appearing more magnesian-rich than would be concluded on the basis of the Fe/Mg ratio, and b) affecting Fe/Mg thermobarometry that relies on the exchange of Fe^{2+} and Mg due to a similar size and charge. In addition, Dyar et al. (2002) have shown how incorporation of Fe^{3+} instead of other 3+ cations changes the thermodynamic properties of these phases. All modern thermodynamic activity models now incorporate Fe^{3+}, unlike the earlier generations, making it worthwhile to experiment with different Fe^{2+}/Fe^{3+} ratios when not analytically determined (i.e. using X-ray absorption near edge structure (XANES)). Assuming a best guess ratio is tricky since iron speciation is generally controlled by redox conditions, and not by chemical composition or metamorphic conditions.

Many studies have outlined the potential of the Ti-in-Quartz geothermo(baro)meter, and besides calibration choice and questions regarding the degree of Ti requilibration the uncertainty in Ti activity (and to a much lesser extent pressure) for the studied samples is a major limitation in constraining deformation temperatures. While not applied in this study, Ashley and Law (2015) provides a method of Ti activity modeling that can be integrated with the equilibrium assemblage modeling when high quality geochemical data is available. Better a_{TiO_2} estimates are also desirable in light of the debate regarding which of the two available calibrations is superior, as this is likely the source of the many apparently contradictory findings in literature.

Whereas for the studied samples temperatures are constrained within a 30-40 °C range given a certain pressure between 2.0 and 3.5 kbar, pressure estimates can only be poorly constrained based on the data presented in this work. Besides a_{TiO_2} and $X_{Fe^{3+}}$ further research should focus on obtaining better pressure estimates in order to place the localized retrograde greenschist overprinting in a context of the area's tectonic and metamorphic evolution. In that context more geochronical data is desired to determine to what degree, if any, Alpine reactivation has occurred. And while data gathered in this study demonstrates fluids have played a major role, the origin of these fluids is unclear: a Ca rich source, or pathway through Ca-rich rocks, is expected based on the elevated Ca-content in the deformed schists, but to make definite statements more trace element (and isotopic) data are needed.

Many of the observed tourmaline crystals, in both the sheared pegmatites and deformed schists, display distinct chemical zoning. Studies by Hinsberg et al. (2006), Hinsberg and Schumacher (2007), Hinsberg and Schumacher (2009), and Berryman et al. (2017) outline the potential use of tourmaline chemistry as a geothermometer: element partitioning (mainly Ca and Ti) between different sectors within a single crystal, due to the polar nature of tourmaline, is temperature-dependent and could thus provide additional information on the metamorphic evolution of these rocks.

5 Conclusions

1. This work has demonstrated the potential of an integrated SEM-AM and thermodynamic modeling approach to deliver reliable results that are consistent with traditional methods, providing the mineral classification is well constrained. The produced SEM-AM false color maps are a valuable asset in evaluating the relation between mineral associations, structural features and mineral reactions.

2. When SEM-AM is used to obtain a bulk rock composition, the mineral compositions used to calculate the BRC should be accurately determined (e.g. using EDS or WDS). The difference between SEM-AM derived mineral compositions and quantitatively determined mineral compositions is then a measure of the quality of the SEM-AM classification.

3. In this study new temperature constraints are provided for the Cap de Creus greenschist facies shear zones: depending on pressure ranging 400-430 °C at 2.5 kbar to 410-450 °C at 3.5 kbar. While Ti-in-Quartz data are associated with large uncertainties due to a poorly constrained Ti-activity these results suggest pressure may be as low as 2 kbar, corresponding to temperatures between 390-420 °C.

4. For the reference schist sample obtained in the transition from the sillimanite-muscovite zone to the sillimanite-K-feldspar zone PT conditions are estimated at 650$\pm$30 °C at pressures of >3.9 kbar, in accordance with earlier estimates.

5. Elements transported by Si- and presumably Ca-rich fluids resulted in a $\pm$54% increase in mass of the deformed schists in the greenschist shear zones compared to the undeformed reference sample.

6. The presence of sillimanite and the preservation of different quartz microstructures, both in the sheared pegmatites, is consistent with a primarily Variscan origin of these shear zones that have deformed the host rocks under progressively decreasing metamorphic conditions.

7. Incorporating iron speciation in thermodynamic modeling highlights the effects that partitioning of iron between its 2+ and 3+ oxidation state can have on mineral stabilities.

Bibliography

Ashley, Kyle T and Richard D Law (2015). "Modeling prograde TiO 2 activity and its significance for Ti-in-quartz thermobarometry of pelitic metamorphic rocks". In: *Contributions to Mineralogy and Petrology* 169.2, p. 23.

Ashley, Kyle T et al. (2013). "P-T-D histories from quartz: A case study of the application of the TitaniQ thermobarometer to progressive fabric development in metapelites". In: *Geochemistry, Geophysics, Geosystems* 14.9, pp. 3821–3843.

Ashley, Kyle T et al. (2014). "Ti resetting in quartz during dynamic recrystallization: Mechanisms and significance". In: *American Mineralogist* 99.10, pp. 2025–2030.

B. Eeckhout, van den (1986). *A case study of a mantled gneiss antiform, the Hospitalet massif, Pyrenees (Andorra, France)*. Vol. 45. Utrecht University.

Bachmann, F, Ralf Hielscher, and Helmut Schaeben (2010). "Texture analysis with MTEX–free and open source software toolbox". In: *Solid State Phenomena*. Vol. 160. Trans Tech Publ, pp. 63–68.

Barker, AJ et al. (2000). "Retrogression by deep infiltration of meteoric fluids into thrust zones during late-orogenic rapid unroofing". In: *Journal of Metamorphic Geology* 18.3, pp. 307–318.

Berryman, Eleanor J. et al. (2017). "Tourmaline as a petrogenetic indicator in the Pfitsch Formation, western Tauern window, eastern Alps". In: *Lithos* 284, pp. 138–155.

Bestmann, Michel and Giorgio Pennacchioni (2015). "Ti distribution in quartz across a heterogeneous shear zone within a granodiorite: The effect of deformation mechanism and strain on Ti resetting". In: *Lithos* 227, pp. 37–56.

Boger, SD, RW White, and B Schulte (2012). "The importance of iron speciation (Fe+ 2/Fe+ 3) in determining mineral assemblages: an example from the high-grade aluminous metapelites of southeastern Madagascar". In: *Journal of Metamorphic Geology* 30.9, pp. 997–1018.

Bossiere, G, J Carreras, and E Druguet (1996). "Structural and petrological evolution of the Cala Serena shear zone (Cap de Creus, East Pyrenees)". In: *Università degli Studi di Milano* 107.

Carreras, J. (2001). "Zooming on Northern Cap de Creus shear zones". In: *Journal of Structural Geology* 23.9, pp. 1457–1486.

Cawood, Tarryn Kim and John Paul Platt (2020). "Variations in the PTt of Deformation in a Crustal-Scale Shear Zone in Metagranite". In: *Earth and Space Science Open Archive ESSOAr*.

Clark, C et al. (2006). "Up-temperature flow of surface-derived fluids in the mid-crust: the role of pre-orogenic burial of hydrated fault rocks". In: *Journal of Metamorphic Geology* 24.5, pp. 367–387.

Connolly, JAD (2009). "The geodynamic equation of state: what and how". In: *Geochemistry, Geophysics, Geosystems* 10.10.

Connolly, JAD and K Petrini (2002). "An automated strategy for calculation of phase diagram sections and retrieval of rock properties as a function of physical conditions". In: *Journal of Metamorphic Geology* 20.7, pp. 697–708.

Connolly, James AD (2005). "Computation of phase equilibria by linear programming: a tool for geodynamic modeling and its application to subduction zone decarbonation". In: *Earth and Planetary Science Letters* 236.1-2, pp. 524–541.

Damm, Klaus-Werner et al. (1992). "Stable isotope constraints on the origin of the Cabo de Creus garnet-tourmaline pegmatites, Massif des Alberes, Eastern Pyrenees, Spain". In: *Geological Journal* 27.1, pp. 75–86.

Diener, JFA and R Powell (2010). "Influence of ferric iron on the stability of mineral assemblages". In: *Journal of Metamorphic Geology* 28.6, pp. 599–613.

Druguet, E. (2001). "Development of high thermal gradients by coeval transpression and magmatism during the Variscan orogeny: insights from the Cap de Creus (Eastern Pyrenees)". In: *Tectonophysics* 332.1-2. ID: doc:5fc7fdaee4b04e4b8c3cc73d; M1: Journal Article, pp. 275–293.

Druguet, E and DHW Hutton (1998). "Syntectonic anatexis and magmatism in a mid-crustal transpressional shear zone: an example from the Hercynian rocks of the eastern Pyrenees". In: *Journal of Structural Geology* 20.7, pp. 905–916.

Druguet, E et al. (1997). "Analysis of a complex high-strain zone at Cap de Creus, Spain". In: *Tectonophysics* 280.1-2, pp. 31–45.

Druguet, Elena, Jordi Carreras, and Jochen E Mezger (2018). "Discussion on 'Middle Jurassic shear zones at Cap de Creus (eastern Pyrenees, Spain): a record of pre-drift extension of the Piemonte–Ligurian Ocean?'Journal of the Geological Society, London, 174, 289–300". In: *Journal of the Geological Society* 175.1, pp. 187–188.

Druguet, Elena et al. (2014). "Zircon geochronology of intrusive rocks from Cap de Creus, Eastern Pyrenees". In: *Geological Magazine* 151.6, pp. 1095–1114.

Dunlap, WJ, G Hirth, and Christian Teyssier (1997). "Thermomechanical evolution of a ductile duplex". In: *Tectonics* 16.6, pp. 983–1000.

Dyar, M Darby et al. (2002). "Fe3+ and Fe2+ partitioning among silicates in metapelites: A synchrotron micro-XANES study". In: *American Mineralogist* 87.4, pp. 514–522.

Forshaw, Jacob B and David RM Pattison (2021). "Ferrous/ferric (Fe2+/Fe3+) partitioning among silicates in metapelites". In: *Contributions to Mineralogy and Petrology* 176.9, pp. 1–26.

Fusseis, Florian, MR Handy, and Christoph Schrank (2006). "Networking of shear zones at the brittle-to-viscous transition (Cap de Creus, NE Spain)". In: *Journal of Structural Geology* 28.7, pp. 1228–1243.

Fußeis, Florian Clemens (2007). "Strain localization and shear zone formation at the brittle-viscous transition, Cap de Creus, Spain". PhD thesis.

Ghent, Edward D and Mavis Z Stout (1984). "TiO 2 activity in metamorphosed pelitic and basic rocks: principles and applications to metamorphism in southeastern Canadian Cordillera". In: *Contributions to Mineralogy and Petrology* 86.3, pp. 248–255.

Gleason, Gayle C and Stephanie DeSisto (2008). "A natural example of crystal-plastic deformation enhancing the incorporation of water into quartz". In: *Tectonophysics* 446.1-4, pp. 16–30.

Grujic, Djordje, Michael, and Joseph L. Wooden (2011). "Thermometry of quartz mylonites: Importance of dynamic recrystallization on Ti-in-quartz reequilibration". In: *Geochemistry, Geophysics, Geosystems* 12.6.

Hayden, Leslie A and E Bruce Watson (2007). "Rutile saturation in hydrous siliceous melts and its bearing on Ti-thermometry of quartz and zircon". In: *Earth and Planetary Science Letters* 258.3-4, pp. 561–568.

Hinsberg, Vincent J. van and John C. Schumacher (2007). "Intersector element partitioning in tourmaline: a potentially powerful single crystal thermometer". In: *Contributions to Mineralogy and Petrology* 153.3, pp. 289–301.

Hinsberg, Vincent J. van and John C. Schumacher (2009). "The geothermobarometric potential of tourmaline, based on experimental and natural data". In: *American Mineralogist* 94.5-6, pp. 761–770.

Hinsberg, Vincent J. Van et al. (2006). "Hourglass sector zoning in metamorphic tourmaline and resultant major and trace-element fractionation". In: *American Mineralogist* 91.5-6, pp. 717–728.

Holland, TJB and R Powell (2011). "An improved and extended internally consistent thermodynamic dataset for phases of petrological interest, involving a new equation of state for solids". In: *Journal of metamorphic Geology* 29.3, pp. 333–383.

Holland, TJB and RTJB Powell (1998). "An internally consistent thermodynamic data set for phases of petrological interest". In: *Journal of metamorphic Geology* 16.3, pp. 309–343.

Huang, Ruifang and Andreas Audétat (2012). "The titanium-in-quartz (TitaniQ) thermobarometer: A critical examination and re-calibration". In: *Geochimica et Cosmochimica Acta* 84, pp. 75–89.

Jiang, Shao-Yong et al. (2005). "Mobility of high field strength elements (HFSE) in magmatic-, metamorphic-, and submarine-hydrothermal systems". In: *Physics and Chemistry of the Earth, Parts A/B/C* 30.17-18, pp. 1020–1029.

Kidder, S., J-P Avouac, and Y-C Chan (2013). "Application of titanium-in-quartz thermobarometry to greenschist facies veins and recrystallized quartzites in the Hsüehshan range, Taiwan". In: *Solid Earth* 4.1, pp. 1–21.

Leeman, William P. et al. (2012). "A study of cathodoluminescence and trace element compositional zoning in natural quartz from volcanic rocks: Mapping titanium content in quartz". In: *Microscopy and Microanalysis* 18.6, pp. 1322–1341.

Lexa, O (2011). *PyWerami: Contour/3D Plotting Program for Perple_X WERAMI Data.(Version 2.0. 1)[Software]*.

Mahar, Emma M et al. (1997). "The effect of Mn on mineral stability in metapelites". In: *Journal of Metamorphic Geology* 15.2, pp. 223–238.

Mainprice, David et al. (1986). "Dominant c slip in naturally deformed quartz: Implications for dramatic plastic softening at high temperature". In: *Geology* 14.10, pp. 819–822.

McCaig, Andrew M (1988). "Deep fluid circulation in fault zones". In: *Geology* 16.10, pp. 867–870.

Menegon, Luca et al. (2011). "Dry and strong quartz during deformation of the lower crust in the presence of melt". In: *Journal of Geophysical Research: Solid Earth* 116.B10.

Mezger, Jochen E, Stephan Schnapperelle, and Christopher Rölke (2012). "Evolution of the Central Pyrenean Mérens fault controlled by near collision of two gneiss domes". In: *Hallesches Jahrbuch für Geowissenschaften* 34, pp. 11–30.

Morgan, DJ et al. (2014). "Using titanium-in-quartz geothermometry and geospeedometry to recover temperatures in the aureole of the Ballachulish Igneous Complex, NW Scotland". In: *Geological Society, London, Special Publications* 394.1, pp. 145–165.

Nachlas, WO, JB Thomas, and Greg Hirth (2018). "TitaniQ deformed: Experimental deformation of out-of-equilibrium quartz porphyroclasts". In: *Journal of Structural Geology* 116, pp. 207–222.

Negrini, Marianne et al. (2014). "The effect of deformation on the TitaniQ geothermobarometer: an experimental study". In: *Contributions to mineralogy and petrology* 167.3, p. 982.

Niedermeier, Dominik RD et al. (2009). "The mechanism of cation and oxygen isotope exchange in alkali feldspars under hydrothermal conditions". In: *Contributions to Mineralogy and Petrology* 157.1, pp. 65–76.

Parsons, A. J. et al. (2016). "Thermo-kinematic evolution of the A nnapurna-D haulagiri H imalaya, central N epal: The C omposite O rogenic S ystem". In: *Geochemistry, Geophysics, Geosystems* 17.4, pp. 1511–1539.

Passchier, Cees W and Rudolph AJ Trouw (2005). *Microtectonics*. Springer Science & Business Media.

Pennacchioni, Giorgio et al. (2010). "Development of crystallographic preferred orientation and microstructure during plastic deformation of natural coarse-grained quartz veins". In: *Journal of Geophysical Research: Solid Earth* 115.B12.

Philpotts, Anthony and Jay Ague (2009). *Principles of igneous and metamorphic petrology*. Cambridge University Press.

Piazolo, Sandra (2001). *Shape fabric development during progressive deformation*. Citeseer.

Plümper, Oliver and Andrew Putnis (2009). "The complex hydrothermal history of granitic rocks: multiple feldspar replacement reactions under subsolidus conditions". In: *Journal of Petrology* 50.5, pp. 967–987.

Putnis, Andrew and Christine V Putnis (2007). "The mechanism of reequilibration of solids in the presence of a fluid phase". In: *Journal of Solid State Chemistry* 180.5, pp. 1783–1786.

Reche, J et al. (1996). "Le massif du Cap de Creus". In: *Métamorphisme Hercynien. Synthèse géologique et géophysique des Pyrénées. Edition BRGM–ITGE* 1, pp. 524–531.

Reverdatto, Vladimir V et al. (2019). "Mineral geothermobarometry". In: *The Nature and Models of Metamorphism*. Springer, pp. 55–82.

Rosenberg, Claudio et al. (2020). "On the causes of brittle nucleation of shear zones: the example of Cap de Creus, Eastern Pyrenees (Spain)". In: *EGU General Assembly Conference Abstracts*, p. 19297.

Schmid, SM and M Casey (1986). "Complete fabric analysis of some commonly observed quartz c-axis patterns". In: *Geophysical Monograph* 36.6, pp. 263–286.

Schulz, Bernhard, Dirk Sandmann, and Sabine Gilbricht (2020). "SEM-based automated mineralogy and its application in geo-and material sciences". In: *Minerals* 10.11, p. 1004.

Spear, Frank S et al. (2012). "Ti diffusion in quartz inclusions: implications for metamorphic time scales". In: *Contributions to Mineralogy and Petrology* 164.6, pp. 977–986.

Stenvall, CA et al. (2020). "Sources and Effects of Fluids in Continental Retrograde Shear Zones: Insights from the Kuckaus Mylonite Zone, Namibia". In: *Geofluids* 2020.

Stipp, Michael et al. (2002). "The eastern Tonale fault zone: a 'natural laboratory'for crystal plastic deformation of quartz over a temperature range from 250 to 700 C". In: *Journal of structural geology* 24.12, pp. 1861–1884.

Stipp, Michael et al. (2010). "A new perspective on paleopiezometry: Dynamically recrystallized grain size distributions indicate mechanism changes". In: *Geology* 38.8, pp. 759–762.

Streit, JE and SF Cox (1998). "Fluid infiltration and volume change during mid-crustal mylonitization of Proterozoic granite, King Island, Tasmania". In: *Journal of Metamorphic Geology* 16.2, pp. 197–212.

Tartèse, Romain et al. (2012). "Mylonites of the South Armorican Shear Zone: Insights for crustal-scale fluid flow and water–rock interaction processes". In: *Journal of Geodynamics* 56, pp. 86–107.

Thomas, Jay B. et al. (2010). "TitaniQ under pressure: the effect of pressure and temperature on the solubility of Ti in quartz". In: *Contributions to Mineralogy and Petrology* 160.5, pp. 743–759.

Thomas, Jay B et al. (2015). "TitaniQ recrystallized: experimental confirmation of the original Ti-in-quartz calibrations". In: *Contributions to Mineralogy and Petrology* 169.3, p. 27.

Tikoff, Basil et al. (2019). "Big data in microstructure analysis: Building a universal orientation system for thin sections". In: *Journal of Structural Geology* 125, pp. 226–234.

Tursi, Fabrizio et al. (2018). “Syn-shearing mobility of major elements in ductile shear zones: state of the art for felsic deformed protoliths”. In: *Periodico di Mineralogia* 87.3.

Van Lichtervelde, Marieke et al. (2017). “U-Pb geochronology on zircon and columbite-group minerals of the Cap de Creus pegmatites, NE Spain”. In: *Mineralogy and petrology* 111.1, pp. 1–21.

Vergés, JAUME, MANEL Fernàndez, and ALBERT Martínez (2002). “The Pyrenean orogen: pre-, syn-, and post-collisional evolution”. In: *Journal of the Virtual Explorer* 8, pp. 55–74.

Vissers, Reinoud L. M. et al. (2017). “Middle Jurassic shear zones at Cap de Creus (eastern Pyrenees, Spain): a record of pre-drift extension of the Piemonte–Ligurian Ocean?” In: *Journal of the Geological Society* 174.2. ID: doc:5fc80159e4b0e2531ab9c881; M1: Journal Article, pp. 289–300.

Vissers, Reinoud L. M. et al. (2018). “Reply to discussion on ‘Middle Jurassic shear zones at Cap de Creus (eastern Pyrenees, Spain): a record of pre-drift extension of the Piemonte–Ligurian Ocean?’ Journal of the Geological Society, London, 174, 289–300”. In: *Journal of the Geological Society* 175.1. ID: doc:5fc8017de4b0b3df12d3bad8; M1: Journal Article, pp. 189–191.

Wark, David A and E Bruce Watson (2006). “TitaniQ: a titanium-in-quartz geothermometer”. In: *Contributions to Mineralogy and Petrology* 152.6, pp. 743–754.

White, R. W., R. Powell, and T. E. Johnson (2014a). “The effect of Mn on mineral stability in metapelites revisited: New a–x relations for manganese-bearing minerals”. In: *Journal of Metamorphic Geology* 32.8, pp. 809–828.

White, RW et al. (2000). “The effect of TiO2 and Fe2O3 on metapelitic assemblages at greenschist and amphibolite facies conditions: mineral equilibria calculations in the system K2O-FeO-MgO-Al2O3-SiO2-H2O-TiO2-Fe2O3”. In: *Journal of Metamorphic Geology* 18.5, pp. 497–511.

White, RW et al. (2014b). “New mineral activity–composition relations for thermodynamic calculations in metapelitic systems”. In: *Journal of Metamorphic Geology* 32.3, pp. 261–286.

Zwart, Hendrik Jan and LU De Sitter (1979). “The geology of the Central Pyrenees”. In.

A Python EDS-AM processing script

```
import sys
import os
import pandas as pd
import numpy as np
import xlsxwriter

#manual set path of parent directory containing mineral folders, comment to
    ↪ enable prompting for parent directory
#parent_dir = '/home/centos/projects/python/_eds'

#List of dictionaries to convert element wt% to oxide wt% for oxides in
    ↪ hp62ver thermodynamic database
el_to_ox = [{
    'element' : 'Silicon',
    'abr' : 'Si',
    'oxide' : 'SiO2',
    'at-mass' : 28.09,
    'ox-mass' : 60.08,
    'factor' : 1
    },
    {
    'element' : 'Aluminium',
    'abr' : 'Al',
    'oxide' : 'Al2O3',
    'at-mass' : 26.98,
    'ox-mass' : 101.96,
    'factor' : 2
    },
    {
    'element' : 'Iron',
    'abr' : 'Fe',
    'oxide' : 'Fe2O3',
    'at-mass' : 55.58,
    'ox-mass' : 159.69,
    'factor' : 2
    },
        {
    'element' : 'Magnesium',
    'abr' : 'Mg',
    'oxide' : 'MgO',
    'at-mass' : 24.31,
    'ox-mass' : 40.30,
    'factor' : 1
```

```
    },
    {
    'element' : 'Calcium',
    'abr' : 'Ca',
    'oxide' : 'CaO',
    'at-mass' : 40.08,
    'ox-mass' : 56.03,
    'factor' : 1
    },
    {
    'element' : 'Sodium',
    'abr' : 'Na',
    'oxide' : 'Na2O',
    'at-mass' : 22.99,
    'ox-mass' : 61.98,
    'factor' : 2
    },
    {
    'element' : 'Potassium',
    'abr' : 'K',
    'oxide' : 'K2O',
    'at-mass' : 39.10,
    'ox-mass' : 94.20,
    'factor' : 2
    },
    {
    'element' : 'Titanium',
    'abr' : 'Ti',
    'oxide' : 'TiO2',
    'at-mass' : 47.87,
    'ox-mass' : 79.87,
    'factor' : 1
    },
    {
    'element' : 'Manganese',
    'abr' : 'Mn',
    'oxide' : 'MnO',
    'at-mass' : 54.94,
    'ox-mass' : 70.74,
    'factor' : 1
    },
    {
    'element' : 'Zirconium',
    'abr' : 'Zr',
    'oxide' : 'ZrO2',
    'at-mass' : 91.22,
    'ox-mass' : 123.22,
    'factor' : 1
    },
    {
    'element' : 'Fluorine',
```

```
    'abr' : 'F',
    'oxide' : 'F2',
    'at-mass' : 19.00,
    'ox-mass' : 38.00,
    'factor' : 2
    },
    {
    'element' : 'Copper',
    'abr' : 'Cu',
    'oxide' : 'CuO',
    'at-mass' : 63.55,
    'ox-mass' : 79.55,
    'factor' : 1
    },
    {
    'element' : 'Sulfur',
    'abr' : 'S',
    'oxide' : 'S2',
    'at-mass' : 32.07,
    'ox-mass' : 65.14,
    'factor' : 2
    },
    {
    'element' : 'Clorine',
    'abr' : 'Cl',
    'oxide' : 'Cl2',
    'at-mass' : 35.45,
    'ox-mass' : 56.03,
    'factor' : 2
    }]

#processing function
def process(mineral):

    path = os.path.join(parent_dir,mineral)
    for filename in os.listdir(path):

    #get all elements and append to list
        if filename.endswith('.xlsx'):
            file_loc = os.path.join(path, filename)
            df = pd.read_excel(file_loc, index_col= None, na_values=['NA'],
                ↪ usecols = "A, B")
            df = df[df['Element'].notna()]

            #put in dict
            for key, value in df.set_index('Element').to_dict()['At. No.'].
                ↪ items():
                elements_dict[key] = value
        break

    else:
```

```
        print('Found no .xlsx-files in directory: ' + path)
        print('Skipping ' + mineral)
        minerals.remove(mineral)
        return(1)

    #dataframe for individual mineral

    df2 = pd.DataFrame()
    df2['Element'] = list(dict(sorted(elements_dict.items(), key=lambda item
        ↪ : item[1])).keys())
    df2.set_index('Element')

    last = 1 #keep track of final column index

    #loop through files
    for filename in os.listdir(path):
        if filename.endswith('.xlsx'):
            file_loc = os.path.join(path, filename)

            #temp dataframe, read element and normalized mass
            dftemp = pd.read_excel(file_loc, index_col=None, na_values=['NA'
                ↪ ], usecols = "A, E")
            #assign filename to column
            colname = filename.split('.')
            dftemp = dftemp.rename(columns={dftemp.columns[1]: colname[0]})

            #merge dataframes
            df2 = pd.merge(df2, dftemp, how = 'outer', on = 'Element')
            last += 1


    #drop rows without valid element
    df2 = df2[df2['Element'].notna()]

    #drop rows that are all-zero, all-NaN, or combination
    df2 = df2[~df2.isin([0, np.nan]).iloc[:,1:last].all(axis = 1)]

    #add statistics
    df2.insert(1, 'Min', df2.iloc[:,1:last].min(axis=1))
    df2.insert(2, 'Mean', df2.iloc[:,2:last + 1].mean(axis=1))
    df2.insert(3, 'Max', df2.iloc[:,3:last + 2].max(axis=1))
    df2.insert(4, '%RSD', df2.iloc[:,4:last + 3].std(axis=1) / df2.iloc[:,4:
        ↪ last + 3].mean(axis=1) * 100)
    df2.insert(5, 'Median', df2.iloc[:,5:last + 4].median(axis=1))

    #for each mineral store df2 in dictionary
    df_dict[mineral] = df2

#processing function for AM results
def process_am():
    #read automated mineralogy data into dataframe
```

```
am_df = pd.read_csv(am_file, sep = '\t', error_bad_lines = False,
    ↪ decimal = ',')
new_columns = am_df.columns.values
new_columns[0] = 'Mineral'
am_df.columns = new_columns
am_df = am_df.set_index('Mineral')
am_df['Average␣Composition'] = am_df['Average␣Composition'].str.replace(
    ↪ ',', '.')
am_df = am_df.drop(['Not␣Analysed'])

#Dataframe to store processed data
headers = ['mineral','wt%','O','Si','Al','Fe','K','Mg','F','Ba','Na','Ca
    ↪ ','Cl','Gd','Mn','W','P','Hf','Dy','Ta','Sm','I','Yb','Sb','Co','
    ↪ Cs','Re','Te','Cu','Ni','Nd','Ce','Sc','Pd','Sn','Cd','Zn','In','
    ↪ Cr','Ga','Pr','U','Ti','N','Nb','Zr','S','La','V','Tl','Pb','Ru','
    ↪ Th','Rb','Ag','Y','Rh','Sr','Bi','Mo','As','Os','Hg','Pt']
am_df2 = pd.DataFrame()
for item in headers:
    am_df2[item] = 0

am_df2['mineral'] = am_df.index
am_df2 = am_df2.set_index('mineral')

#Split csv from cells in df
for mineral in am_df2.index.tolist():
    am_df2.at[mineral, 'wt%'] = am_df.loc[mineral, 'Weight␣%']
    templist = am_df.loc[mineral, 'Average␣Composition'].split(';␣')
    for item in templist:
        if item != '':
            am_df2.at[mineral, item.split('␣')[0]] = item.split('␣')[1]

#Assume average density for unclassified and correct other weight
    ↪ percentages for unclassified
am_df2['wt%'] = am_df2['wt%'] * (1 - am_df.loc['Unclassified', 'Area␣%']
    ↪  / 100)
am_df2.at['Unclassified', 'wt%'] = am_df.loc['Unclassified', 'Area␣%']


#dataframe for brc
brc_df = pd.DataFrame()
brc_df['Mineral'] = am_df2.index
brc_df = brc_df.set_index('Mineral')
brc_df = brc_df.T

#temp dataframe to calc BRC
df_temp = pd.DataFrame()
df_temp['Oxide'] = brc_df.index

#calculate oxide wt% for elements for which conversion is available and
    ↪ store in brc_df
for mineral in am_df2.index:
```

```
    for element in df4.index:
        brc_df.at[df4.loc[element, 'oxide'], mineral] = am_df2.loc[
            ↪ mineral, df4.loc[element, 'abr']] / df4.loc[element, '
            ↪ factor'] / df4.loc[element, 'at-mass'] * df4.loc[element,
            ↪ 'ox-mass']
    total = brc_df[mineral].sum()
    brc_df[mineral] = brc_df[mineral] / total * 100
    #calculate contribution to BRC
    df_temp[mineral] = brc_df[mineral] * am_df2.loc[mineral, 'wt%'] / 100
#add column with BRC
df_temp['BRC␣(AM)'] = df_temp.sum(axis = 1)
brc_df['BRC␣(AM)'] = df_temp['BRC␣(AM)']
df_temp = brc_df

#append row with wt%
brc_df = pd.DataFrame()
brc_df['wt%'] = am_df2['wt%']
brc_df = brc_df.T
brc_df = brc_df.append(df_temp)

#calculate BRC based on EDS composition + AM wt%, when no EDS
    ↪ composition is available for a mineral use AM composition
if eds_results == True:
    combi_brc = pd.DataFrame(df5)
    combi_brc.loc['wt%'] = 0
    for mineral in am_df2.index:
        if mineral in eds_minerals:
            combi_brc[mineral] = df5[mineral]
            combi_brc.at['wt%', mineral] = brc_df.loc['wt%', mineral]
        else:
            combi_brc[mineral] = brc_df[mineral]

    wt_row = combi_brc.loc['wt%']
    combi_brc.drop(['wt%'] , inplace = True)
    combi_brc = combi_brc.multiply(np.array(wt_row) / 100, axis = 1)
    combi_brc['BRC␣(EDS+AM)'] = combi_brc.sum(axis = 1)
    combi_brc_col = combi_brc.pop('BRC␣(EDS+AM)')

    brc_df = pd.concat([brc_df, combi_brc_col], axis=1, join="outer",
        ↪ ignore_index = False)

brc_df = brc_df.reset_index(level=None, drop=False, inplace=False,
    ↪ col_level=0, col_fill='')
brc_df = brc_df.rename(columns={'index': ''})

brc_col = brc_df.pop('BRC␣(AM)')
brc_df.insert(1, 'BRC␣(AM)', brc_col)

if eds_results == True:
    brc_combi_col = brc_df.pop('BRC␣(EDS+AM)')
    brc_df.insert(2, 'BRC␣(EDS␣+␣AM)', brc_combi_col)
```

```
        #Indicate minerals for which EDS compositions are used in EDS + AM
            ↪ brc calculation
        for mineral in eds_minerals:
            brc_df.rename(columns = {mineral: mineral + ' (X)'} , inplace =
                ↪ True)

    return(brc_df)

#prompt for sample name
sample = input('Sample name: ')

am_results = False
eds_results = False

print('1 - Process only EDS-measurements. \n2 - Process only AM results. \n3
    ↪  - Do both.')
while True:
    inp = input('Option: ')
    if inp in ('1', '2', '3'):
        break
    print('Invalid input.')

if inp == '1':
    eds_results = True
elif inp == '2':
    am_results = True
else:
    eds_results = True
    am_results = True

if am_results == True:
    while True:
        am_file = input('AM results filename or path to file: ')
        if os.path.isfile(am_file):
            break
        else:
            print ("File does not exist. ")

#prompt for parent dir, not executed if parent dir above is set
if 'parent_dir' not in locals() and eds_results == True:
    parent_dir = ''
    inp = input('Current directory (' + os.getcwd() + ') contains EDS data
        ↪ folders? [Y/N]\n')
    if inp.lower() in ('yes', 'y'):
        parent_dir = os.getcwd()
    elif inp.lower() in ('no', 'n'):
        while os.path.exists(parent_dir) is False:
            parent_dir = input('Path of directory containing data: ')
            if os.path.exists(parent_dir) is False:
                print('Invalid path.')
```

```
    else:
        print('Invalid input.')
        quit()


#empty dict for elements
elements_dict = {}

#empty list for minerals
eds_minerals = []

#empty dictionary for storing mineral dataframes
df_dict = {}

#empty datafram for overview
df3 = pd.DataFrame()

#dataframe for converting to oxides
df4 = pd.DataFrame(el_to_ox)
df4 = df4.set_index('element')


#loop through directories and process content
if eds_results == True:
    dir_bool = False
    for subdir, dirs, files in os.walk(parent_dir):
        if dirs:
            dir_bool = True
        if not dir_bool:
            print('No directories found. Aborting.')
            quit()
        else:
            for dir in dirs:
                fullpath = os.path.join(parent_dir, dir)
                eds_minerals.append(dir)
                process(dir)


    #add elements to overview DF
    df3['Element'] = list(dict(sorted(elements_dict.items(), key=lambda item
        ↪ : item[1])).keys())

    #df containing oxides overview
    df5 = pd.DataFrame(df4['oxide'])
    df5 = df5.set_index('oxide')

    #aggregate minerals in overview and oxide wt%
    for mineral, df in df_dict.items():
        #overview
        dftemp = pd.DataFrame()
        dftemp['Element'] = df['Element']
```

```
        dftemp[mineral] = df['Mean']
        df3 = pd.merge(df3, dftemp, how = 'outer', on = 'Element')

        #Oxides
        #New column for each mineral
        df5[mineral] = ''
        df = df.set_index('Element')
        for element in df.index:
            #Only process elements for which oxide conversion is available
            if element in df4.index.tolist():
                df5.at[df4.loc[element, 'oxide'], mineral] = df4.loc[element,'
                    ↪ ox-mass'] / df4.loc[element,'factor'] * df.loc[element,
                    ↪ 'Mean'] / df4.loc[element,'at-mass']
        df5 = df5.replace(r'^\s*$', np.nan, regex=True)
        #sum total weight
        total = df5[mineral].sum()
        #Convert to wt%
        df5[mineral] = df5[mineral] / total * 100


    #drop all-NaN rows in overview
    df3 = df3[~df3.drop('Element', axis = 1).isna().all(1) & df3['Element'].
        ↪ notna()]

if am_results == True:
    brc_df = process_am()

if eds_results == True:
    #Reset index df5, drop all-NaN rows, change column header from oxide to
        ↪ Oxide
    df5 = df5.reset_index(level=None, drop=False, inplace=False, col_level
        ↪ =0, col_fill='')
    df5 = df5[~df5.drop('oxide', axis = 1).isna().all(1) & df5['oxide'].
        ↪ notna()]
    df5 = df5.rename(columns={'oxide': 'Oxide'})

    #final dictionary with overviews as first items followed by minerals
    fin_dict = {'EDS␣Overview␣(atomic␣wt%)' : df3, 'EDS␣Overview␣(oxide␣wt%)
        ↪ ' : df5}
    if am_results == True:
        fin_dict['AM-results␣(oxide␣wt%)'] = brc_df
    fin_dict.update(df_dict)
else:
    fin_dict = {'AM-results␣(oxide␣wt%)' : brc_df}



#write data to xlsx-file
pd.io.formats.excel.ExcelFormatter.header_style = None
writer = pd.ExcelWriter(sample + '.xlsx', engine='xlsxwriter')
workbook = writer.book
```

```
#set formats
default = workbook.add_format({'bold': True, 'font_color': 'black'})
integer = workbook.add_format({'num_format': '0.00', 'align': 'center'})
text = workbook.add_format({'bold': True})
mean = workbook.add_format({'bold': True, 'font_color': 'red', 'align': '
    ↪ center'})
statheader = workbook.add_format({'bold': True, 'font_color': 'black', '
    ↪ align': 'center'})
measurement_head = workbook.add_format({'font_color': '#9C0006', 'align': '
    ↪ center'})


highlight = workbook.add_format({'bold': True, 'font_color': '#9C0006'})

for sheetname, df in fin_dict.items(): # loop through dict with dataframes
    df.to_excel(writer, sheet_name = sheetname, index = False) # send df to
        ↪ writer
    worksheet = writer.sheets[sheetname] # pull worksheet object
    for idx, col in enumerate(df): # loop through columns
        series = df[col]
        max_len = max((
            series.astype(str).map(len).max(), # len of largest item
            len(str(series.name)) # len of column header
            )) + 1 # adding a little extra space
    worksheet.set_column('B:ZZ', max_len, integer)
    worksheet.set_column('A:A', max_len, text)
    worksheet.set_row(0, None, measurement_head)
    worksheet.conditional_format('A1:F1', {'type': 'cell', 'criteria': '=',
        ↪ 'value': '"Element"', 'format': statheader})
    worksheet.conditional_format('A1:F1', {'type': 'cell', 'criteria': '=',
        ↪ 'value': '"Min"', 'format': statheader})
    worksheet.conditional_format('A1:F1', {'type': 'cell', 'criteria': '=',
        ↪ 'value': '"Mean"', 'format': mean})
    worksheet.conditional_format('A1:F1', {'type': 'cell', 'criteria': '=',
        ↪ 'value': '"Max"', 'format': statheader})
    worksheet.conditional_format('A1:F1', {'type': 'cell', 'criteria': '=',
        ↪ 'value': '"%RSD"', 'format': statheader})
    worksheet.conditional_format('A1:F1', {'type': 'cell', 'criteria': '=',
        ↪ 'value': '"Median"', 'format': statheader})
    worksheet.conditional_format('A1:F1', {'type': 'cell', 'criteria': '=',
        ↪ 'value': '"Oxide"', 'format': statheader})

if eds_results == True:
    for mineral in eds_minerals:
        worksheet = workbook.get_worksheet_by_name(mineral)
        #highlight measurements off by more than two SD
        worksheet.conditional_format('G2:ZZ99', {'type': 'cell', 'criteria':
            ↪ '>', 'value': '$C2␣+␣($C2␣*␣$E2␣*␣0.01␣*␣2)', 'format':
            ↪ highlight})
```

```
        worksheet.conditional_format('G2:ZZ99', {'type': 'cell', 'criteria':
            ↪ '<', 'value': '$C2␣-␣($C2␣*␣$E2␣*␣0.01␣*␣2)', 'format':
            ↪ highlight})

writer.save()
```

B AFM Diagrams

AFM diagrams projected from muscovite. White, gray and black fields consist of respectively three, two and one phase(s) plus quartz, muscovite and H_2O.

First page: AFM diagrams for 400-550 °C at 25 °C intervals at 2 kbar with BRC for MD95CC.1 based on AM and AM + EDS. Shown for reference in the first diagram are: Cap de Creus schist composition from literature (Druguet et al., 1997) an CC97-9.

Second page: AFM diagrams from 450-625 °C at 25 °C intervals at 4 kbar with the BRC of sample CC97-9 based on AM + EDS.

Mineral abbreviations: And = andalusite, Bt = biotite, Chl = chlorite, Crd = Cordierite, Ctd = Chloritoid, Ky = kyanite, Sill = sillimanite, St = staurolite.

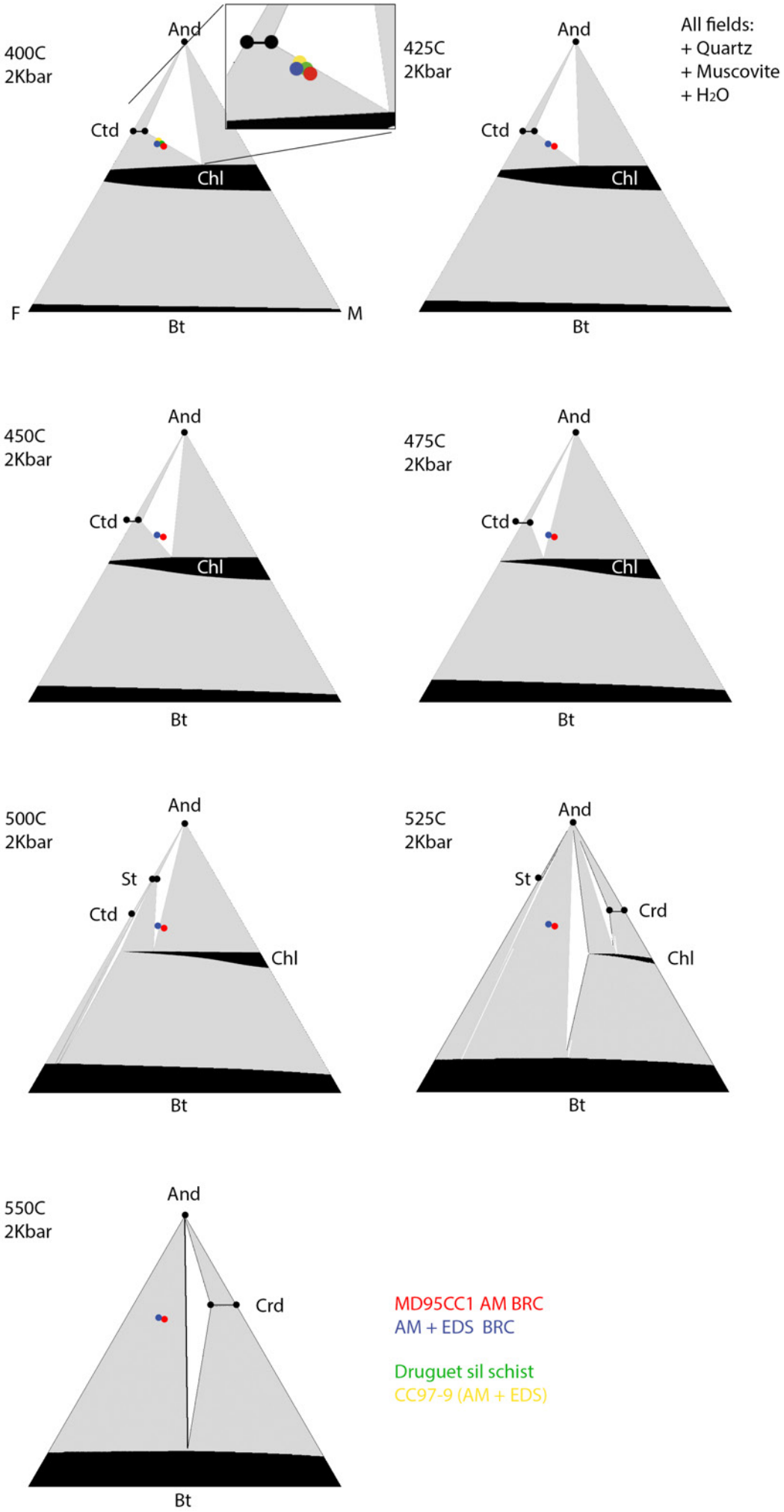
400C
2Kbar
And
Ctd
Chl
F
M
Bt
425C
2Kbar
And
Ctd
Chl
Bt
All fields:
+ Quartz
+ Muscovite
+ H2O
450C
2Kbar
And
Ctd
Chl
Bt
475C
2Kbar
And
Ctd
Chl
Bt
500C
2Kbar
And
St
Ctd
Chl
Bt
525C
2Kbar
And
St
Crd
Chl
Bt
550C
2Kbar
And
Crd
Bt
MD95CC1 AM BRC
AM + EDS BRC
Druguet sil schist
CC97-9 (AM + EDS)

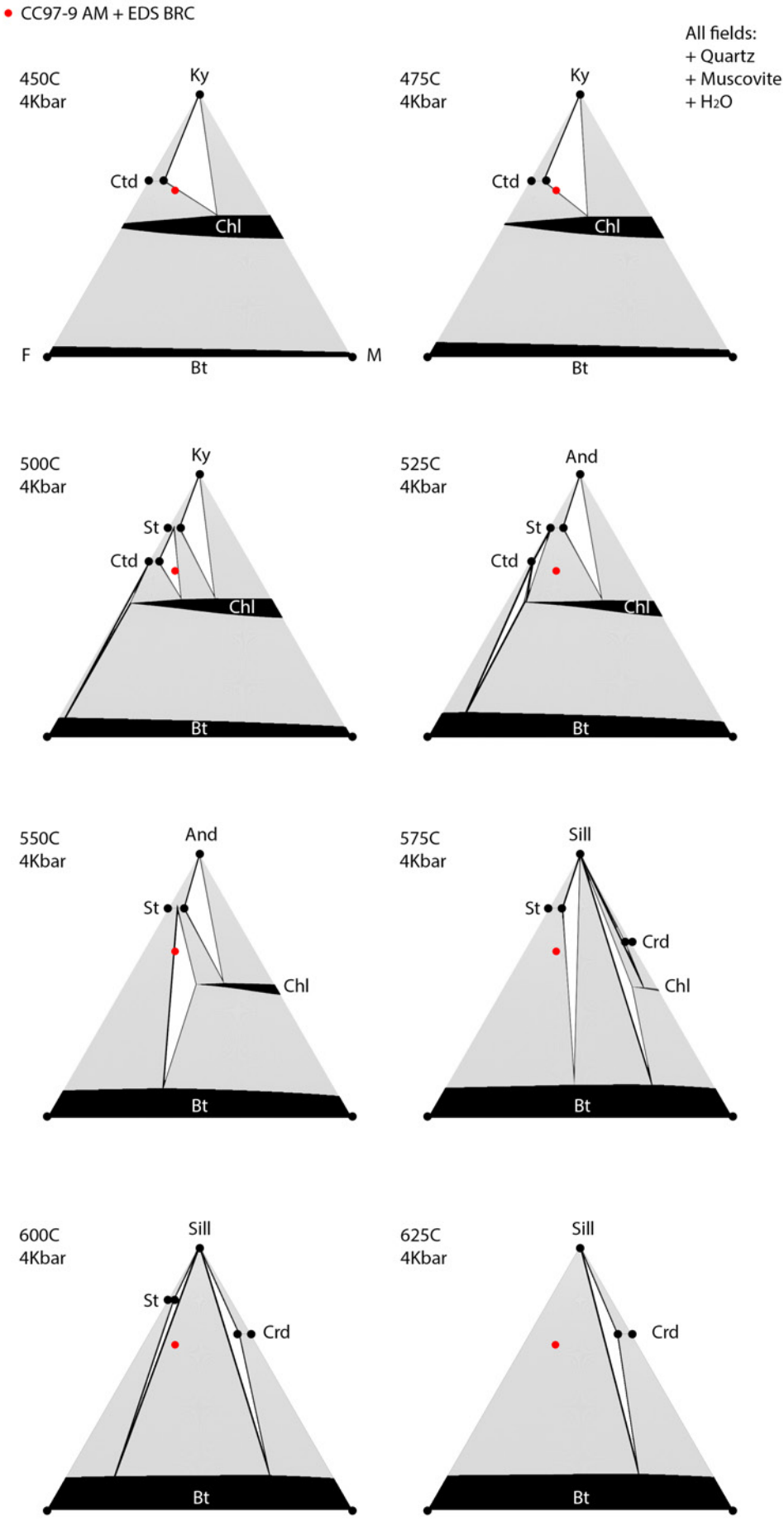
CC97-9 AM + EDS BRC
All fields:
+ Quartz
+ Muscovite
+ H2O
450C
4Kbar
Ky
Ctd
Chl
F
M
Bt
475C
4Kbar
Ky
Ctd
Chl
Bt
500C
4Kbar
Ky
St
Ctd
Chl
Bt
525C
4Kbar
And
St
Ctd
Chl
Bt
550C
4Kbar
And
St
Chl
Bt
575C
4Kbar
Sill
St
Crd
Chl
Bt
600C
4Kbar
Sill
St
Crd
Bt
625C
4Kbar
Sill
Crd
Bt

C Grain size distribution MD95CC.3

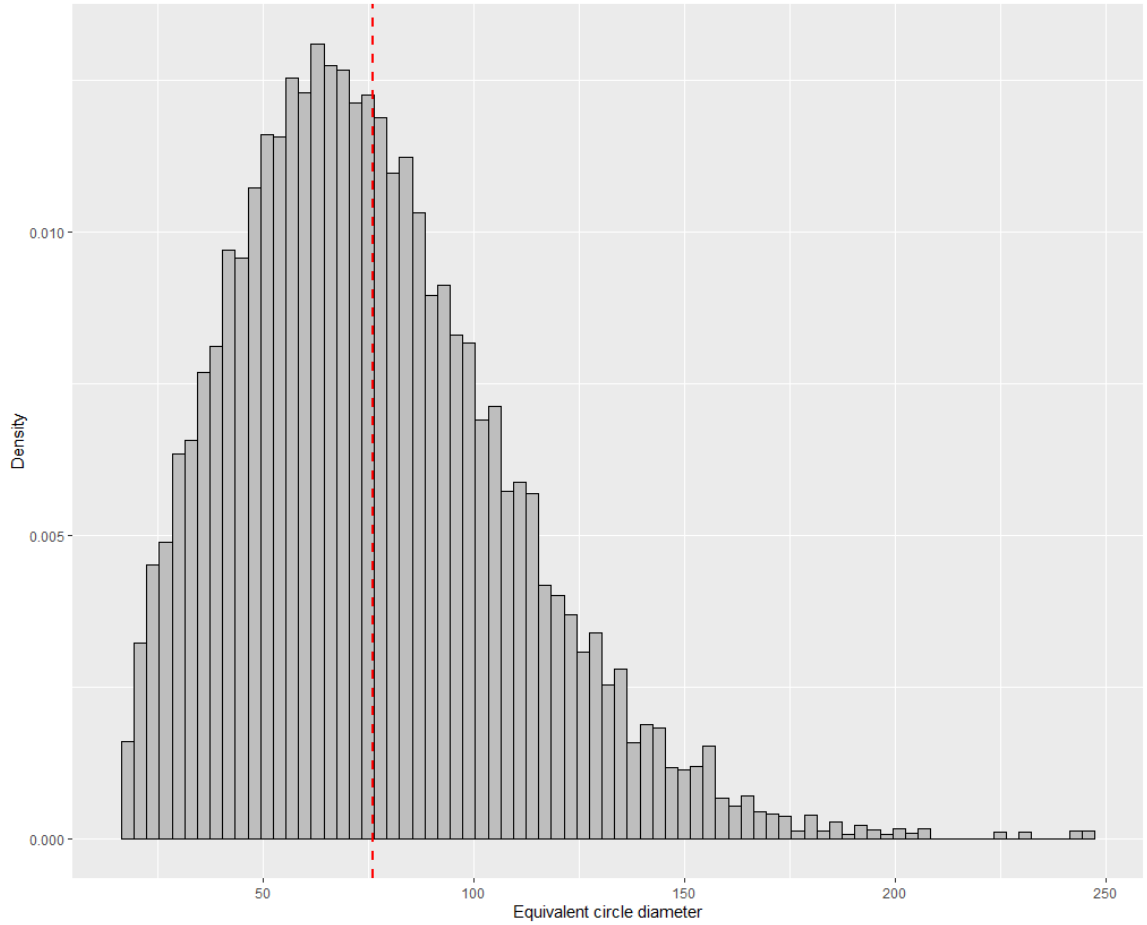

FIGURE C.1: Area weighted quartz grain size distribution for thin section MD95CC.3 based on EBSD data. Vertical line is the mean at 76 µm.

D Oxides normalized against SiO_2

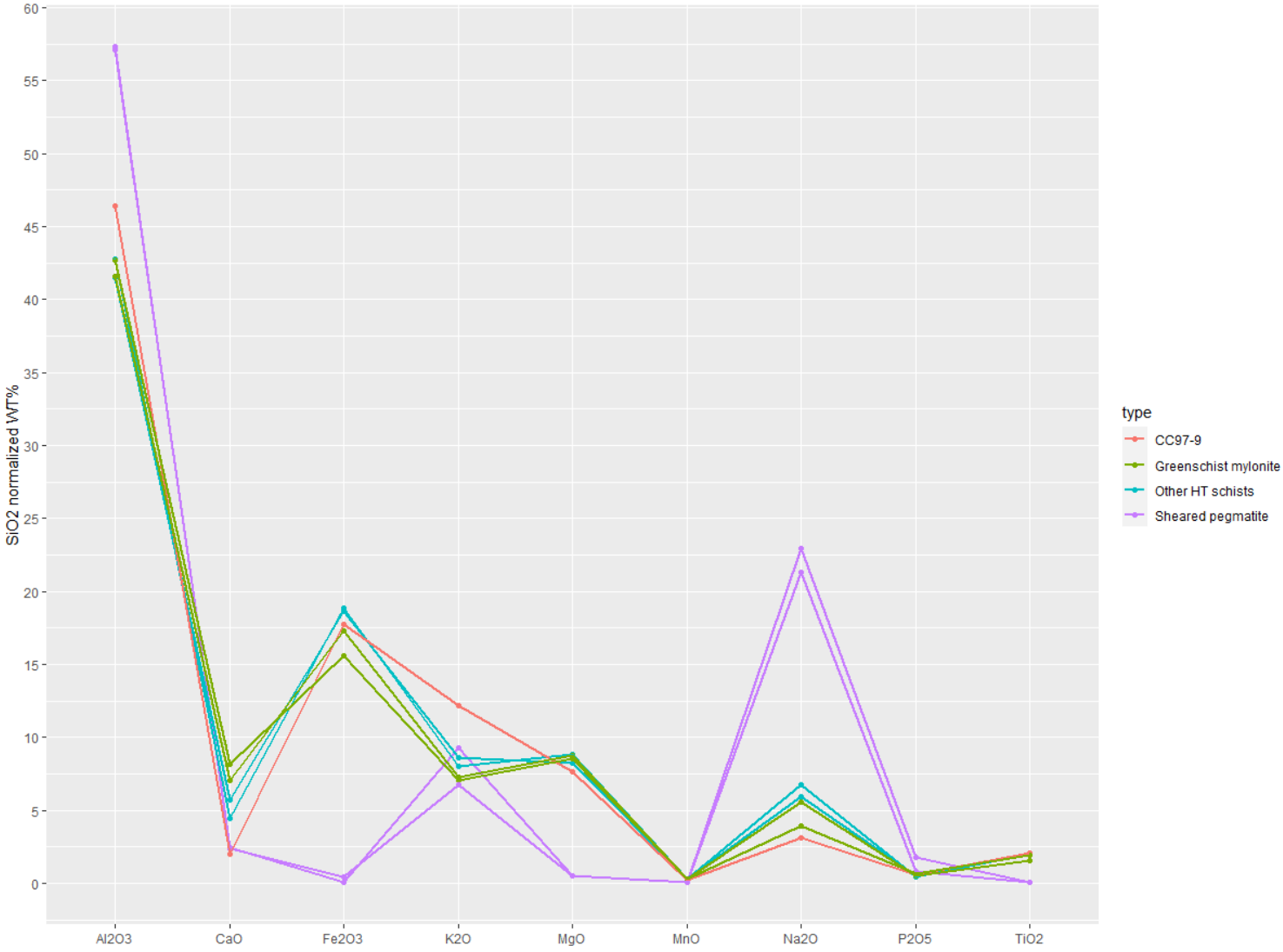

FIGURE D.1: XRF data normalized against SiO_2. HT schists: contain the not discussed samples CC95X-1 & CC95-12 besides CC97-9. Greenschist mylonite: MD95CC.1 & MD95CC.4. Sheared pegmatite: BB1B & BB2B.

E CL maps & SIMS transects

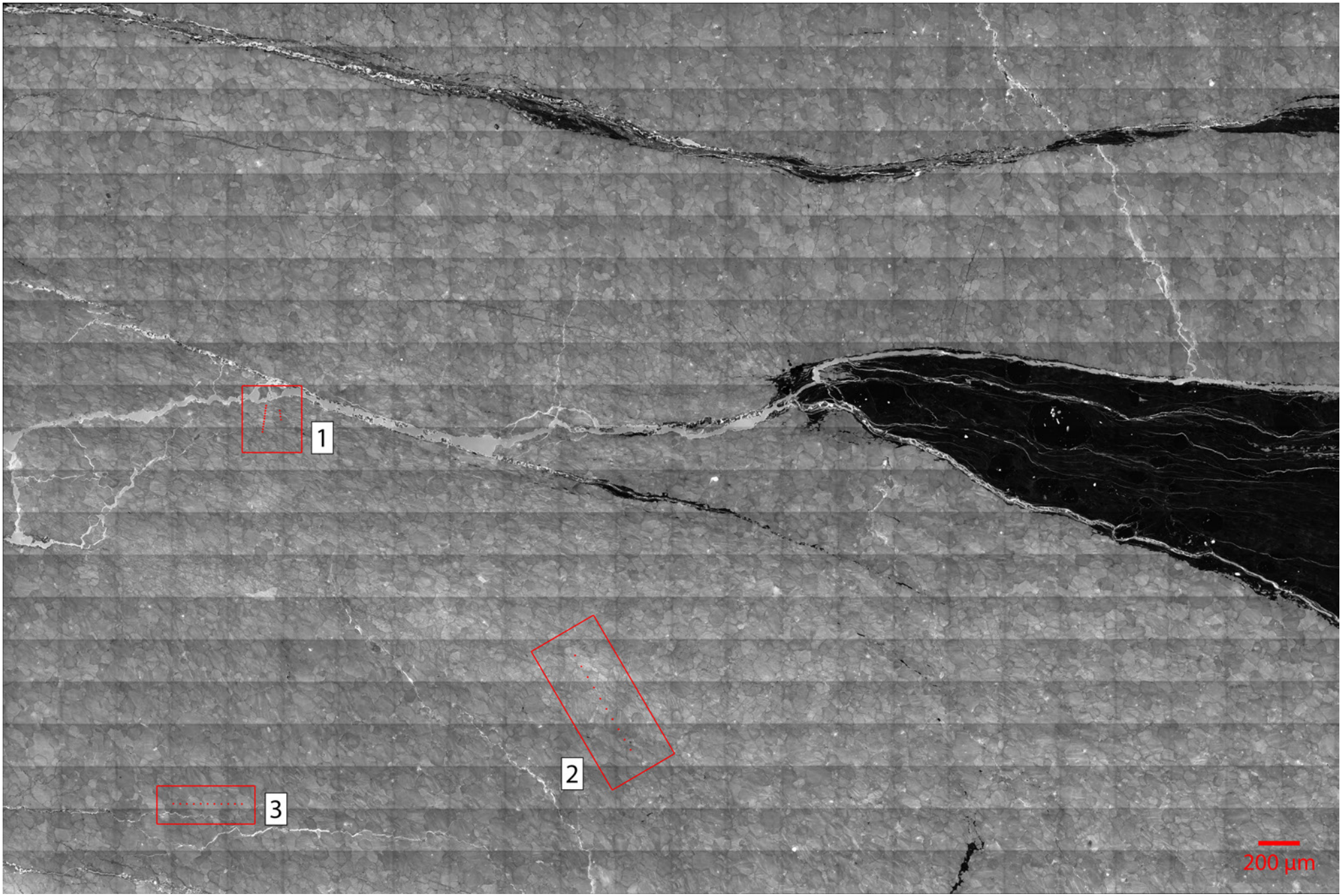

FIGURE E.1: CL map of a region in thin section MD95CC.1 with measurement locations. Numbers correspond to the transects in the figures that follow below.

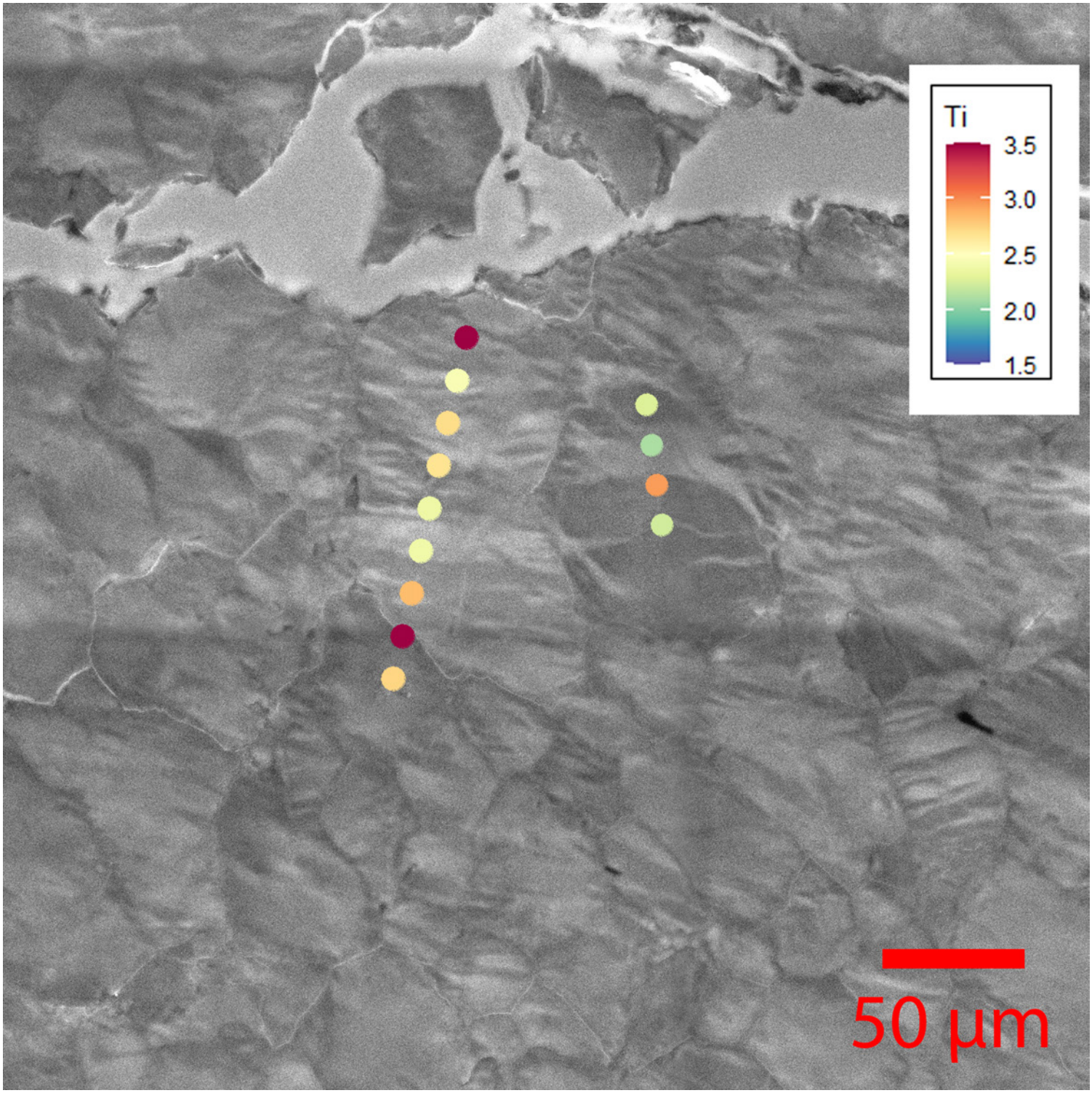

FIGURE E.2: Transect 1 in thin section MD95CC.1 with the exact measurement spots.

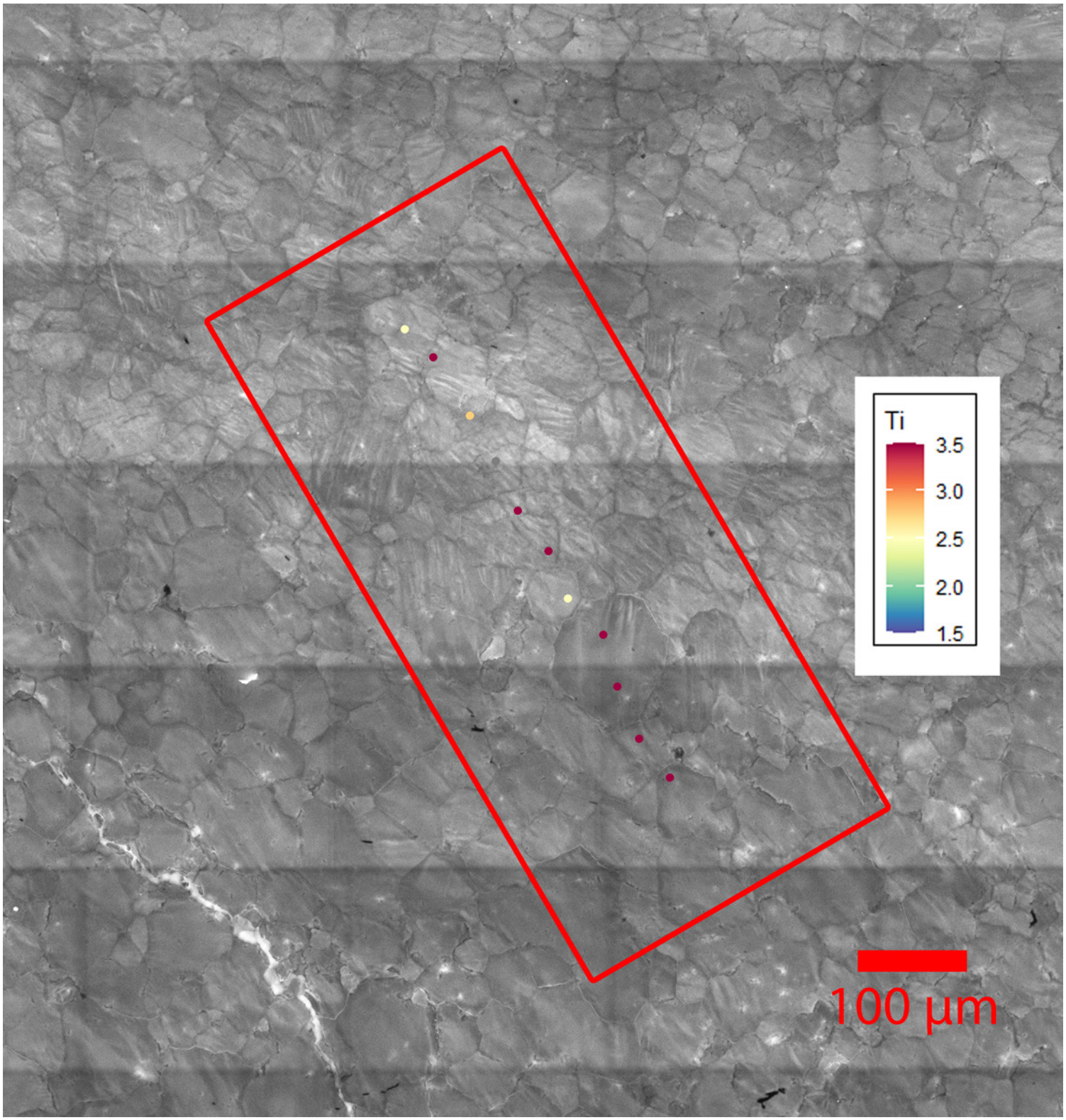

FIGURE E.3: Transect 2 in thin section MD95CC.1 with the exact measurement spots. The 10 µm spot size resulted in most measurements [Ti] > 10 ppm.

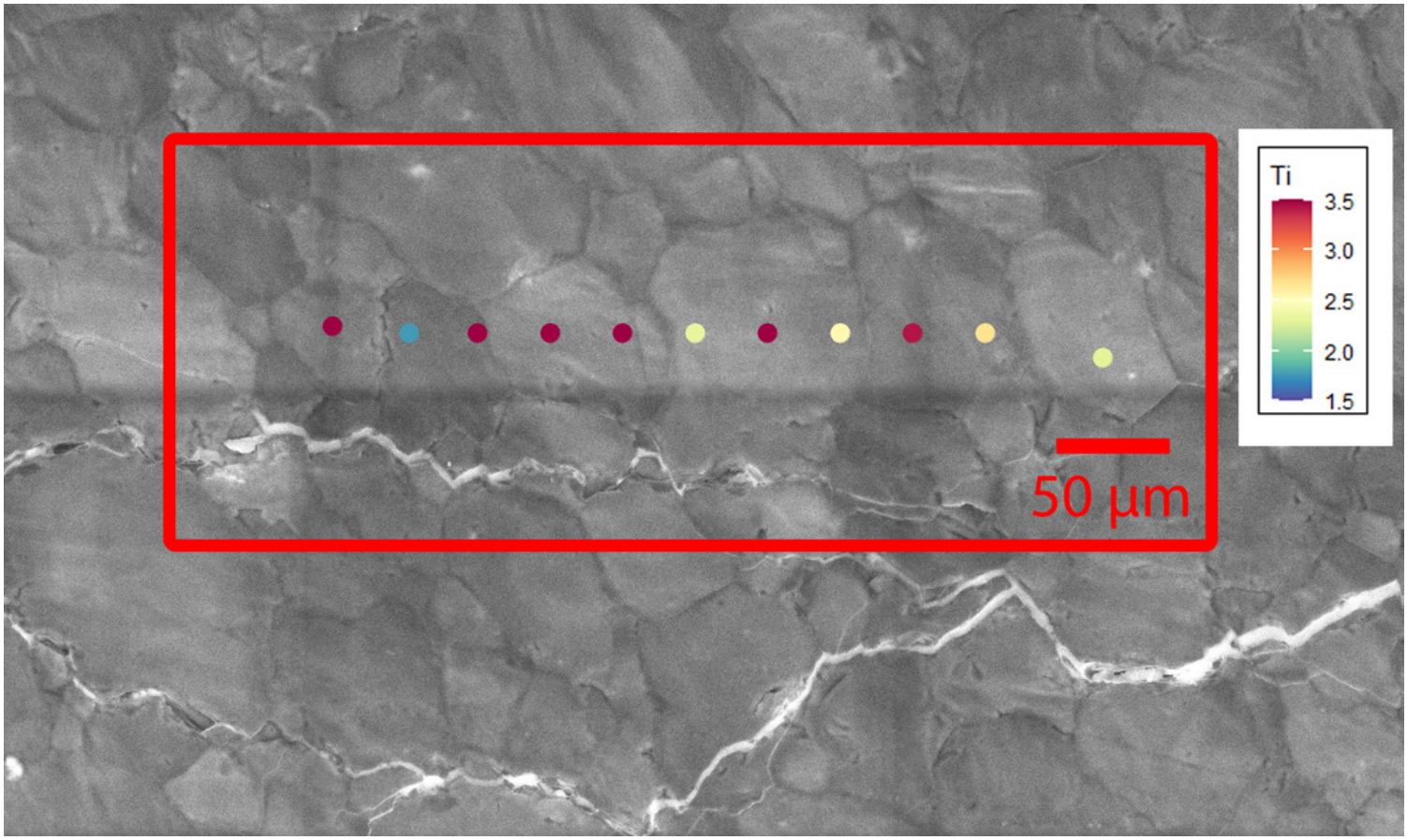

FIGURE E.4: Transect 3 in thin section MD95CC.1 with the exact measurement spots.

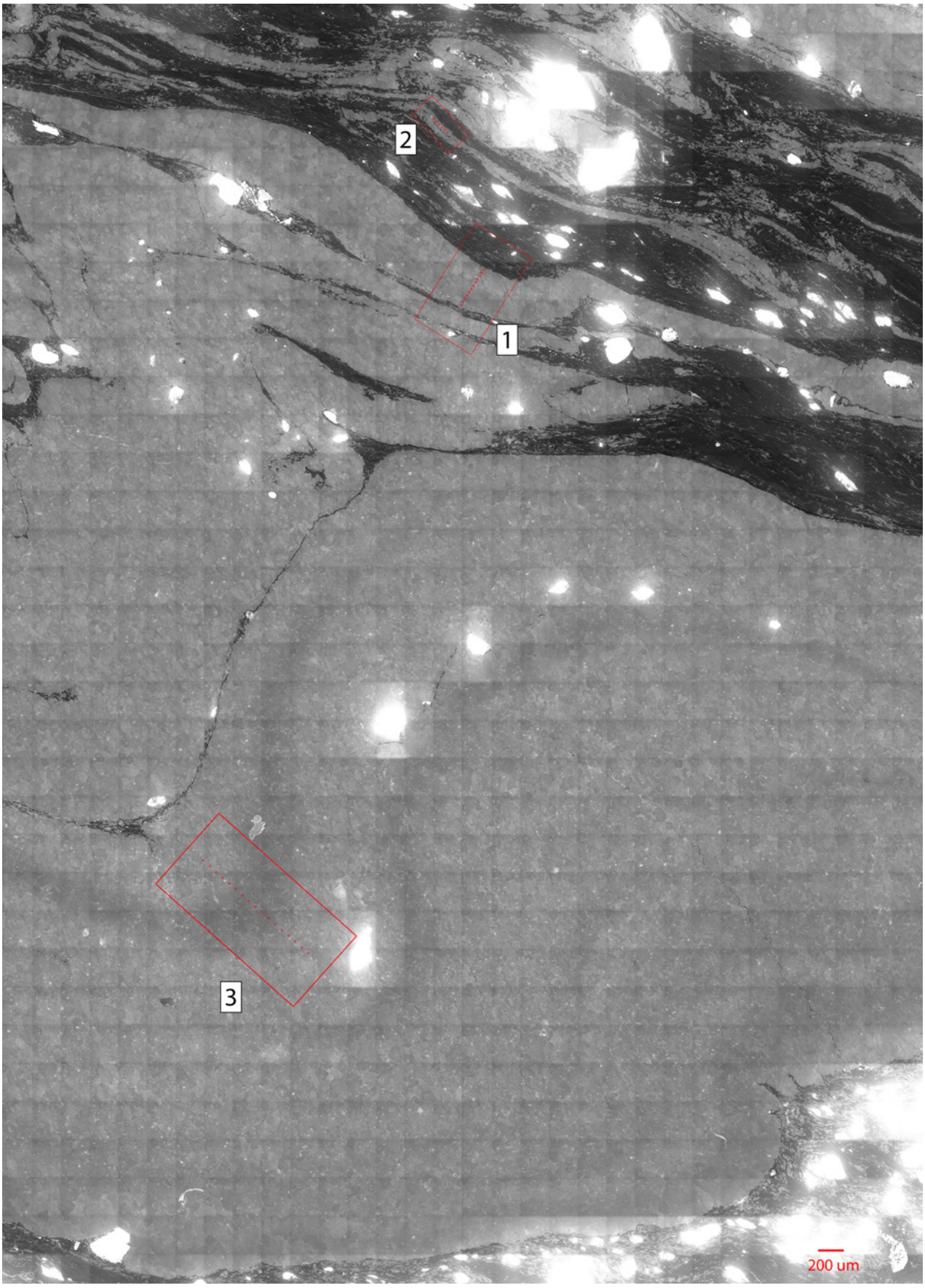

FIGURE E.5: CL map of a region in thin section MD95CC.3 with measurement locations. Note how bands of low CL intensity follow the fold geometry. Numbers correspond to the transects in the figures that follow below.

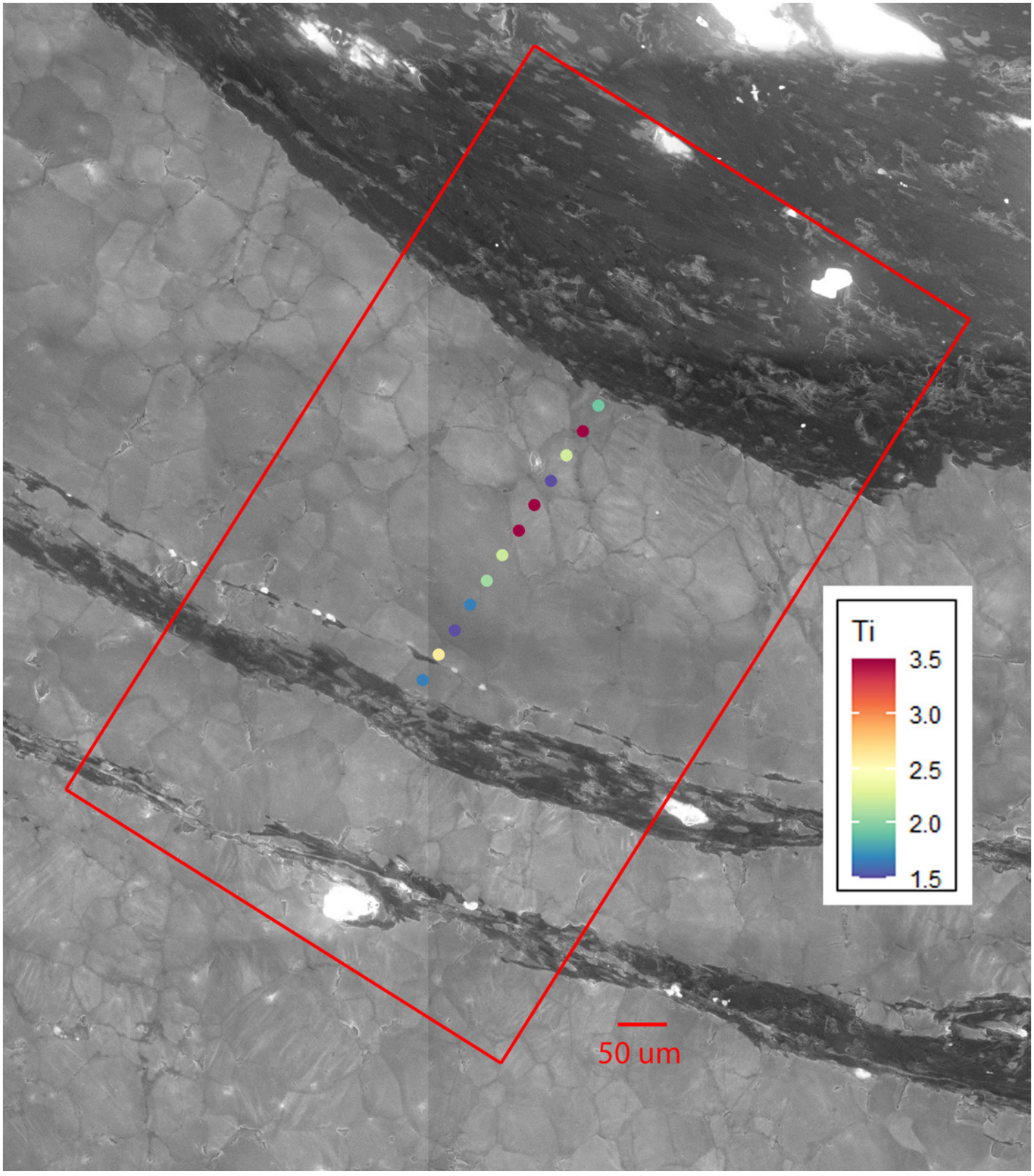

FIGURE E.6: Transect 1 in thin section MD95CC.3 with the exact measurement spots.

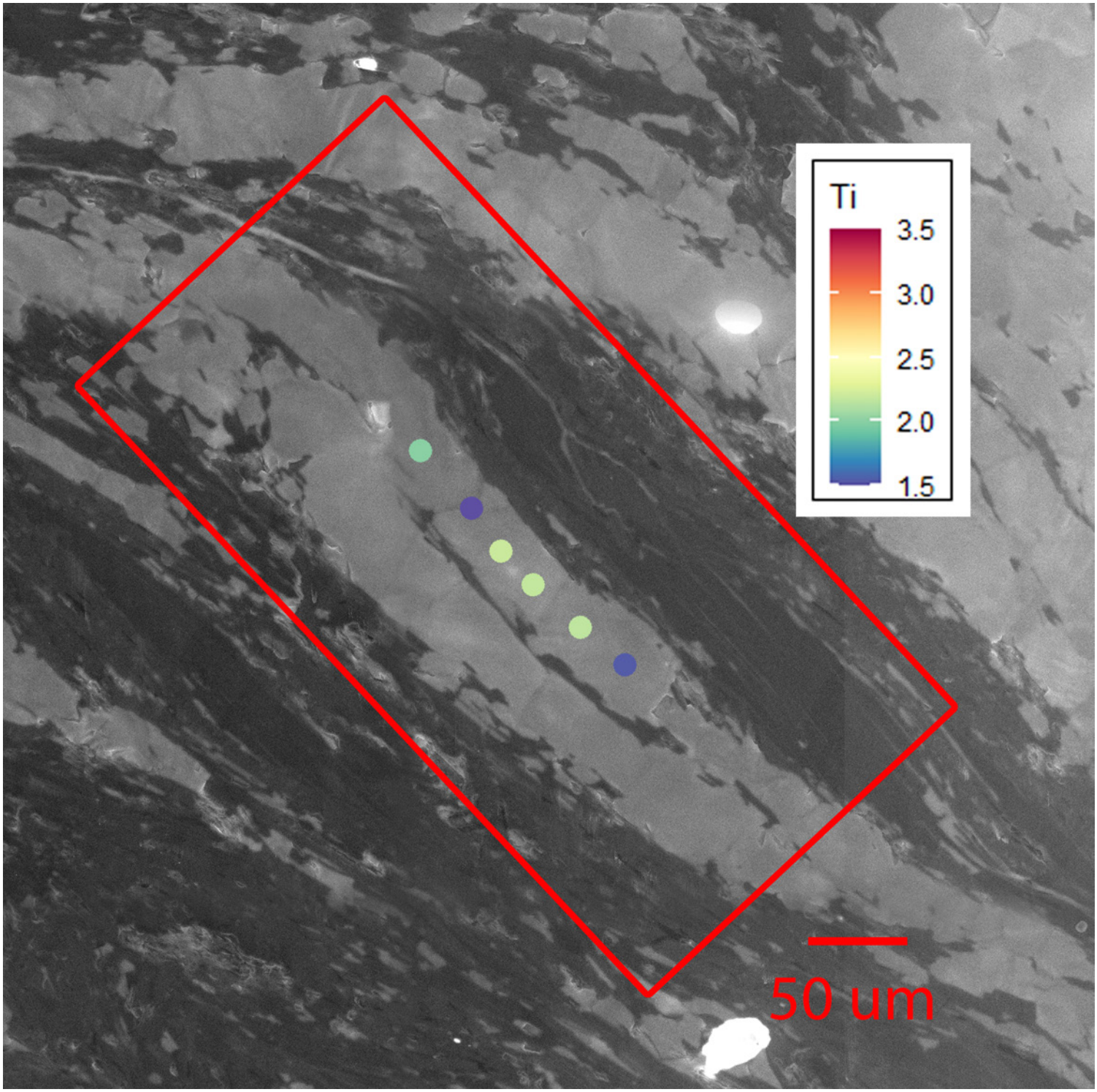

FIGURE E.7: Transect 2 in thin section MD95CC.3 with the exact measurement spots.

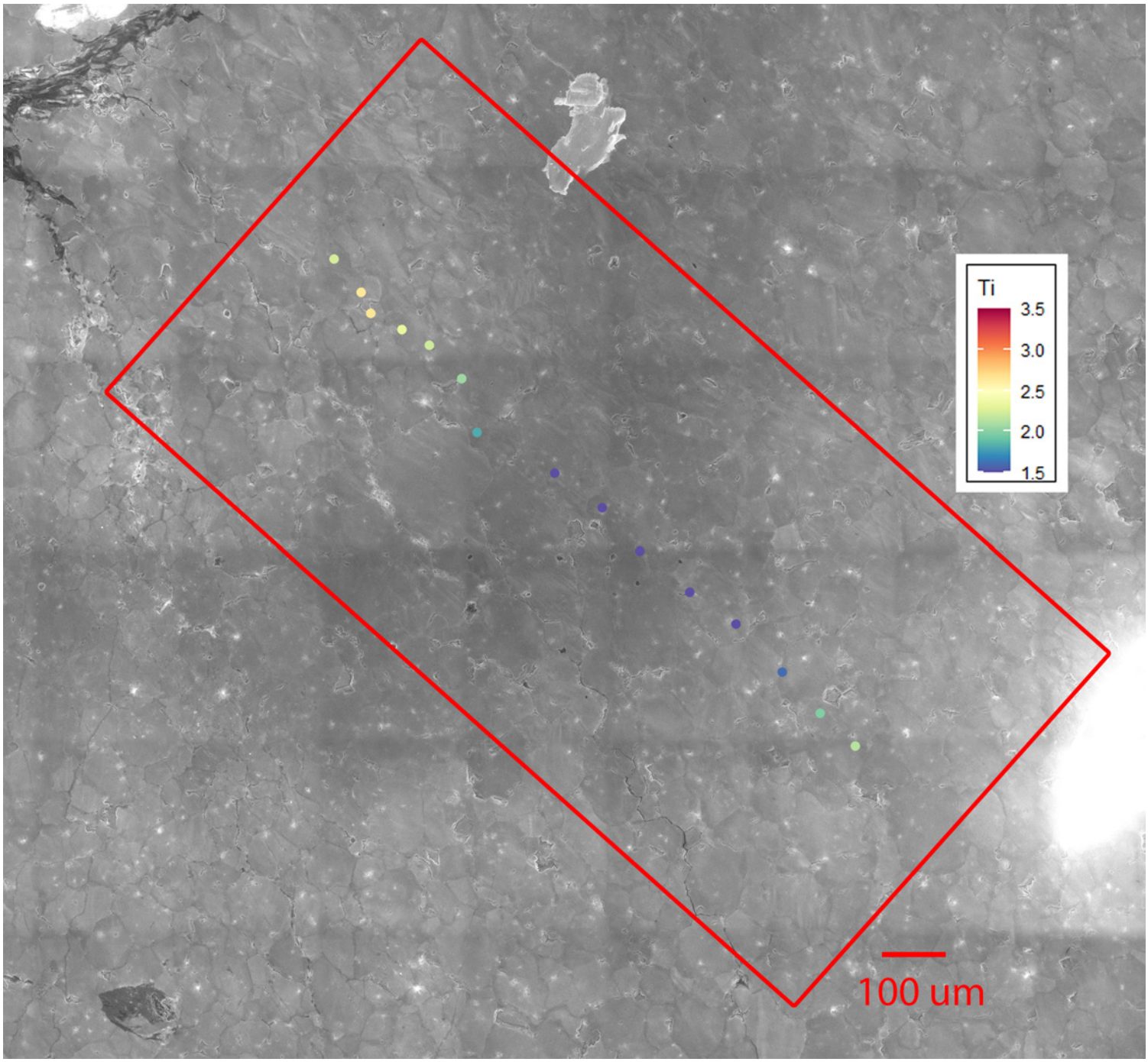

FIGURE E.8: Transect 3 in thin section MD95CC.3 with the exact measurement spots. Note the correlation between CL intensity and measured Ti concentrations.

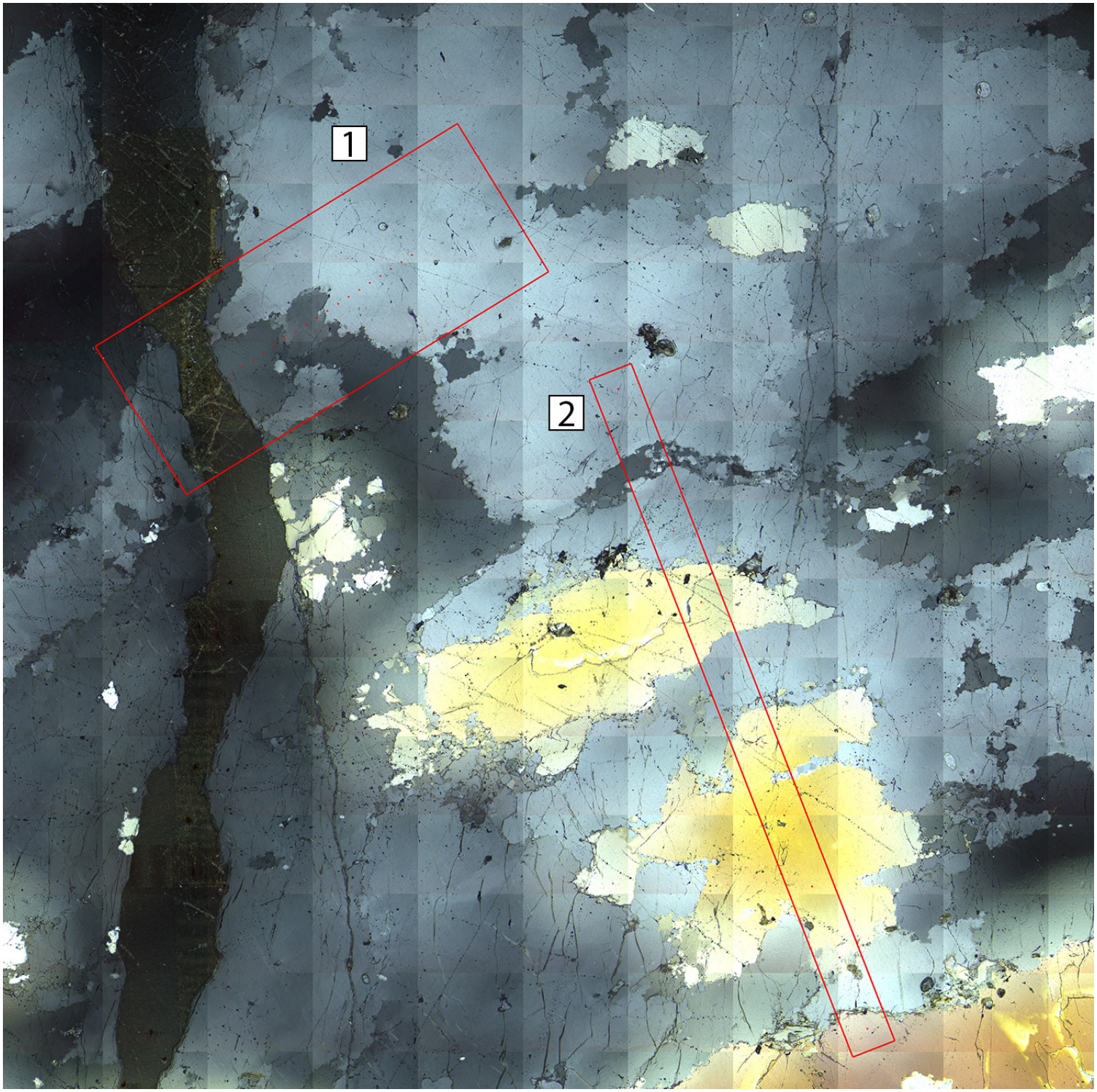

FIGURE E.9: Transects in thin section FR3 with the approximate measurement spots plotted in reflected light view. Mean Ti concentrations of 2.82±0.68 ppm and 7.22±1.06 ppm for transect 1 and 2, respectively.